Intermediate Coulomb Excitation of ^{77,79}Zn

Shailendra Bhandari

Thesis submitted for the degree of
Master in Nuclear and Energy Physics
60 credits

Department of Physics
The Faculty of Mathematics and Natural Science

UNIVERSITY OF OSLO

Spring 2021

Intermediate Coulomb Excitation of ^{77,79}Zn

Shailendra Bhandari

Intermediate Coulomb Excitation of ^{77,79}Zn

http://www.duo.uio.no/

Printed: Reprosentralen, University of Oslo

Contents

List of Figures

List of Tables

Abstract

This thesis work is focused to study the collectivity of the odd-even ^{77,79}Zn nuclei via intermediate-energy Coulomb excitation. ^{77,79}Zn, having 30 protons and 47 and 49 neutrons, will help understand both shell evolution and collective properties near ^{78}Ni. The experiment subject to the thesis was conducted in April 2015 at the Radioactive Ion Beam Factory (RIBF), RIKEN Nishina Center, Japan. The beams of radioactive nuclei near ^{78}Ni, including the ^{77,79}Zn isotopes were produced by the in-flight fission of a primary beam of ^{238}U at 345 MeV/u bombarding a 3 mm thick ^{9}Be target. These exotic Zn isotopes to be investigated were separated, selected, and identified using the BigRIPS in-flight fragment separator. The identified particles were further transported to the focal point, F8, where they impinged on a reaction target of ^{197}Au at 948 mg/cm^2 thickness. The DALI2 γ-ray spectrometer, which is an array formed by 186 NaI(Tl) detector, surrounding the reaction target, was used to detect the γ-rays emitted by the decay of the excited states of ^{77,79}Zn. Finally, the reaction products exited the target and were identified by the ZeroDegree spectrometer. In order to deduce the contribution from the nuclear interaction on the γ-ray yield observed for ^{77,79}Zn, another set of data was taken using the reaction target of ^{12}C (903 mg/cm^2 thick) during the experiment.

Using the Doppler-corrected γ-ray spectra for ^{79}Zn, a new transition at 1260 keV has been observed in the present experiment. The tentative spin assignment and origin of this newly identified collective state will be discussed in this thesis. The γ-ray spectrum obtained for ^{77}Zn shows rather scattered structure with several transitions. This can be related to a different excitation mechanism which will be further discussed in the present thesis.

Acknowledgement

First and foremost, I would like to express my gratitude to my supervisors Professor Andreas Görgen and Dr. Eda Sahin for their constant support and advice throughout this project. A special thanks to Andreas for being available every week with enlightening suggestions and encouragements. I consider myself very fortunate for being able to work with a very considerate and encouraging professor like him. Eda has always been positive and encouraging and it is difficult to overrate her efforts that make this work thrive. I really appreciate her guidance, and for giving me a unique opportunity to work on the experimental data from RIKEN Radioactive Ion Beam Factory. I appreciate the time I spent with everybody that I met during this period since they all contributed in different ways to enrich my experiences in studies and in life. Thanks for the good advice, help, and enriching ideas you provided.

I am grateful to the Nuclear Physics Group for giving me a great working environment, gathering students and highly devoted professors and employees together at meetings and conferences. Thank you for letting me go to the summer school in South Africa and letting me participate in different conferences. Thanks to this, I have many adventures to look back on.

I would like to thank Julian, Tellef and Fardous on both personal and academic accounts. They patiently helped me to distill our problems and made an enjoyable studying environment. Thanks to everyone at the fourth-floor office, it was a pleasure to get to know and work together with all other members of the nuclear physics group at UiO.

These acknowledgments would not be complete without thanking my family for their support throughout this period. I could not stand here without my brothers, Dr. Janarjan Bhandari, Rameshwor Bhandari and Saroj Bhandari. They always loved me and supported my every choice. My father nourished my curiosity and allowed me to explore the world. My mother, for the constant love and who always believes in me. Their everlasting encouragement, love, and unconditional support helped me to see it calmly through to the end.

Last but not the least, I would like to thanks the University of Oslo and the state of Norway for providing free and quality education. I (being an international student) could not have written this thesis without this excellent opportunity.

Chapter 1

Introduction

If you've never done anything wrong it's probably because you have never tried anything new.

ALBERT EINSTEIN, RELATIVITY: THE SPECIAL AND THE GENERAL THEORY

The advent of Radioactive Ion Beam (RIB) facilities has given a boost on nuclear structure studies, over a wide area of the chart of nuclides. The RIBs permit to study and investigate entirely new nuclear topics as, for example, the dynamics of exotic nuclei[1], the limits of nuclear existence and the modification of the shell structure, and the magic numbers far from stability with extreme neutron-to-proton ratios. One of the main discoveries made when studying exotic nuclei was that the magic numbers observed near the valley of stability change dramatically for extreme neutron-to-proton ratios. This phenomenon of the shell evolution as a function of proton and neutron has been widely studied recently both theoretically and experimentally [1]. In recent years, experiments with RIBs have shown that in some neutron-rich nuclei well-established shell closures vanish, and the new magic numbers appears. Some examples of this effect are presented in section 2.2, "the evolution of the shell structure in exotic nuclei".

This thesis focuses on the study of very neutron-rich nuclei around ^{78}Ni mainly ^{77,79}Zn via intermediate-energy Coulomb excitation. ^{77,79}Zn nuclei having 30 protons and 47 and 49 neutrons, will help understand both shell evolution and collective properties in the ^{78}Ni mass region. This is particularly important since the experimental input is missing for the odd-even neutron-rich Zn isotopes and the ^{79}Zn is the most exotic Zn isotope where the collective properties can be explored via Coulomb excitation. A Coulomb excitation experiment at intermediate energies was conducted in 2015 at the Radioactive Ion Beam Factory (RIBF), RIKEN, Japan and the Zn isotopes were populated via in-flight fission of ^{238}U primary beam on a thick ^{9}Be target. Coulomb excitation will selectively populate the states due to collective excitations which is the primary scope of the present work. The goal of this thesis is therefore, to determine the gamma ray intensity of the major obtained peaks of ^{77,79}Zn isotopes through the reaction. The validity of the method for the calculation of gamma ray intensity was tested by fitting the well known peak of ^{78}Zn at 730 keV transition. In order to determine the collectivity,

[1] The nuclei which are located far away from the valley of stability are known as "exotic nuclei".

the reduced transition probabilities, B(E2) values, have to be determined. The calculated gamma ray intensity can be used to achieve the cross-section and finally to calculate the B(E2) values. To overcome the possible interference of the nuclear and the electromagnetic excitation at intermediate energies, the contribution from nuclear inelastic scattering was studied in the same experimental condition using a light C target as a secondary target instead of a heavy-Z Au target in order to increase the probability of the nuclear interaction. These conditions are explained in section 2.5.2.

The thesis in overall is organized as follows. Chapter 2 gives an overview of the theoretical and experimental considerations. Chapter 3 presents the experimental set up for the production, separation and identification of isotopes of interest. In chapter 4, the data analysis procedure is explained. Chapter 5 shows the obtained experimental results and discussion, and provides the conclusions and outlook of the thesis work.

Chapter 2

Nuclear Structure

Science is beautiful when it makes simple explanations of phenomena or connections between different observations. Examples include the double helix in biology and the fundamental equations of physics.

STEPHEN HAWKING

Quantum mechanics, a mathematical tool for predicting the behavior of microscopic particles, a realm of physics since Newton formulated the foundations of classical mechanics and the Schrödinger equation, formulated by Erwin Schrödinger in 1926 [2], is the quantum analog of Newton's second law. The equation elaborates two key concepts of quantum mechanics: the wave function (ψ) and operators which operate on a wave function to extract information. It has two forms, the time-dependent Schrödinger equation to explicitly define how the wave function of a particle will evolve in time and the time-independent Schrödinger equation in which time dependence has been removed and describe, among other things, what the allowed energy is of the particles.

$$i\hbar\frac{\partial}{\partial t}\psi = H\psi \tag{2.1}$$

$$-\frac{\hbar^2}{2m}\nabla^2\psi + V(x)\psi = E\psi \tag{2.2}$$

They are also a postulate of quantum mechanics, a theory that is one of the pillars of modern electronic technology.

Atoms are the foundation of nature and nature is a composition of different chemical compounds of the organic and inorganic world. The electronic configuration, i.e. electrons surrounding the atom, is a crucial finding in the history of chemistry. In a similar manner, the stability of the nucleus is very decisive for the existence of the atom. The problem of which atoms may exist is therefore reduced to the problem of what nuclei may exist. A nucleus is composed of protons and neutrons and the stability of the nuclei is closely related to the forces holding them together. It is nuclear structure physics that studies the effective forces between the nucleons.

There are four fundamental interactions, also known as the fundamental forces in Physics- Gravitational, Electromagnetic, Strong and Weak forces, which govern the particle (object) interaction or particle decay process. These forces are characterized on the basis of the types of the particles that experience the force, the relative strength of force, the range over which the force is effective and the nature of the particles that mediate the force. The gravitational force is the force of attraction between two objects that have mass and energy. It is probably the most intuitive and familiar of the fundamental forces that hold the planets, the stars, the solar system and even the galaxies together. This force, however, turns out to be the weakest of the fundamental forces, at the atomic or molecular scale. The electromagnetic and the strong nuclear interaction play a significant role in nuclear stability. As the name suggests the electromagnetic force (sum of electric and the magnetic force) acts between the charged particles like positively charged protons and negatively charged electrons, forming the atoms. In the case of nuclei, it acts as a repulsive force between the protons due to the positive charge of the protons and tries to disintegrate the nucleus. The weak force is also important for nuclear stability, as it governs beta decay. The attractive gravitational force, being orders of magnitude weaker, can by no means compensate for this repulsive Coulomb force. Therefore, the short-range strong nuclear interaction is responsible for holding the nuclei together.

2.1 Nuclear Models

The existence of nuclei in each atom was discovered by Rutherford in 1911 [3], after the so-called Rutherford experiment. Rutherford and his team bombarded α-particles into a thin gold (metal) foil, and observed the scattering of the particles. They expected the α-particles to pass straight through the foil, with little deflection. However, the result was astonishing that the α-particles were observed to have a large spread in scattering angles. These astonishing results explain the existence of a positively charged nucleus at the center of the atom. In 1913, Niels Bohr [4] proposed his famous model of the atom on the basis of atomic theory. The atomic theory consists of negatively charged electrons in orbits around a positively charged nucleus at the center. The atomic shell model can explain complicated details of the atomic structure and chemistry. At the time when Bohr developed the shell model of the atom, the second constituent of the nucleus, the neutron, was unknown. In 1932, 46 years after the discovery of the proton, the neutron was identified by James Chadwick. In nuclear physics, an analogous model to the atomic shell model can be used to explain the nuclear structure.

2.1.1 The Liquid Drop Model

The semi-empirical mass formula and the binding energy of the nucleus using liquid drop model is defined as

$$m(N,Z) = \frac{1}{c^2}E(N,Z) = NM_n + ZM_H - \frac{1}{c^2}B(N,Z) \tag{2.3}$$

$$B(N,Z) = a_V A - a_S A^{2/3} - a_C \frac{z^2}{A^{1/3}} - a_I \frac{(N-Z)^2}{A} \pm \delta \tag{2.4}$$

where m(N,Z) is the atomic mass corresponding to the neutron number N and the proton number Z, and M_n and M_H the free neutron and the hydrogen atom masses. Similarly, B(N,Z) is the binding energy and the leading terms in Equation [2.4] are described as follows:

- Volume term (a_V): The volume term assumes the constant nucleon density. It reflects the nearly linear A-dependence of the nuclear volume or the A-independence of the nuclear density i.e. $E \propto R^3 \propto A$. Most authors give $a_V \cong 16$ MeV.
- Surface term (a_S): The surface energy is proportional to the nuclear surface area and represents the loss of the binding energy suffered by the particles in the surface layer due to lower density(fewer surface) there i.e. $E \propto R^2 \propto A^{2/3}$.
- Coulomb term (a_C): It is also called the electric repulsion term, corresponds to the electrostatic energy of a homogeneously charged sphere of radius R_C i.e. $E = \frac{3}{5}\frac{q^2}{R_c}$.
- Isospin (also called asymmetry) term (a_I): This term reflects the fact that nuclear force favors either an equal number of neutrons or protons(N=Z) or to have more N than Z, however, the limitations brought about by the Pauli principle have to be considered at the same time.
- Pairing term δ: For even-even nuclei it is $+\delta$, for odd-even nuclei $\delta = 0$ and for odd-odd nuclei it is $-\delta$.

This simple model explains a lot of important features like the binding energy per nucleon of large numbers of nuclei and illustrates which nuclei undergo fusion and fission processes, the effect of the isospin, and the pairing terms for the binding energy, and the energies of radioactive decay. Even though this model describes the general features very well, it is unable to describe the shell effects, and reproduce the "magic numbers" seen from the experiments. This is because this model is purely phenomenological where we fit five parameters, and the model uses some assumptions about the nuclear force. It has short range, which explains the overall features of the volume and surface terms; the model also considers pairing as part of the nuclear force.

2.1.2 The Shell Model

In the atomic shell model, each shell is filled by the atomic electrons in the order of increasing energies such that each sub-shell with orbital angular momentum l can take up to 2(2l+1) electrons. The atomic properties are then determined by the electrons in a non-completely filled shell which leads to a periodicity of atomic properties such as the atomic radius and the ionization energy. The same model cannot be adapted to the nuclear shell model because the potential is not external to the particles but created by themselves and the nucleons are much larger than the electrons. Nevertheless, the shell orbitals are filled with two types of particles, protons and neutrons with a complicated system but the atomic shells are filled with one type of particle (electron) obeying Pauli's principle. The high ionization potential for noble gases like ${}_2He$, ${}_{10}Ne$, ${}_{18}Ar$, ${}_{36}Kr$, ${}_{54}Xe$, ${}_{86}Rn$ with atomic numbers 2, 10, 28, 36, 54, 86 respectively is the single-electron energy of the valance electron that is removed when the atom becomes singly ionized. The corresponding quantity in the nuclear shell model is the large neutron

or proton separation energies for the nuclei at proton and the neutron numbers 2, 8, 20, 28, 50, 82, 126. These numbers are magic numbers with enhanced stability demonstrating the evidence of the shell structure. The nuclear shell structure is described by the shell model where the protons and neutrons separately fill quantized energy levels. The description of such a quantized energy level is given by the Schrödinger equation for single-particle states [5]:

$$H\psi_i(r) = \epsilon_i\psi_i(r) \tag{2.5}$$

$$\left(\frac{-\hbar^2}{2m}\nabla^2 + V(r)\right)\psi_i(r) = \epsilon_i\psi_i(r) \tag{2.6}$$

where H is the Hamiltonian and the first part of the Hamiltonian represents the kinetic energy whereas the second one is the effective potential. The potential used for the shell model are for example the Harmonic Oscillator (HO) potential, square well potential and the Wood-Saxon potential [6]. The Woods-Saxon potential has the form

$$V(r) = \frac{V_0}{1 + exp[\frac{(r-R)}{a}]} \tag{2.7}$$

The Woods-Saxon potential falls somewhere between the two such potentials, namely the harmonic oscillator potential

$$V(r) = \frac{1}{2}m\omega^2 r^2 \tag{2.8}$$

and the square well potential

$$V(r) = \begin{cases} -V_0 & \text{if } r \leq R_0 \\ +\infty & \text{if } r > R_0. \end{cases} \tag{2.9}$$

The spherical harmonic oscillator is not very realistic but can be solved analytically. A more realistic choice would be the Woods-Saxon potential. Even with the more realistic potential we still cannot explain all the experimental magic numbers. In order to accurately describe the magic numbers above N, Z = 20, the idea was to incorporate a strong spin-orbit term in the Hamiltonian, developed by Maria Goeppert Mayer [7] and O.Haxel, Hans Jensen and Hans Suess [8], for which Goeppert-Mayer and Jensen were awarded the Nobel Prize in 1963. The associated potential can be written as

$$V(r) = \frac{1}{\hbar^2}V_{so}(r)\vec{l}\cdot\vec{s} \tag{2.10}$$

where $\vec{l}$ and $\vec{s}$ are angular momentum and the spin operators respectively for a single nucleon. Since

$$\left\langle \vec{l}\cdot\vec{s} \right\rangle = \begin{cases} l\frac{\hbar^2}{2} & \text{for } j = l + 1/2 \\ -(l+1)\frac{\hbar^2}{2} & \text{for } j = l - 1/2, \end{cases} \tag{2.11}$$

the total potential is

$$V_{nuc}(r) = \begin{cases} V_0 + V_{so}\frac{l}{2} & \text{for } j = l + 1/2 \\ V_0 - V_{so}\frac{l+1}{2} & \text{for } j = l - 1/2. \end{cases} \tag{2.12}$$

This term splits the degeneracy of the levels depending on $j = l + \frac{1}{2}$ or $j = l - \frac{1}{2}$. Also, the spin-orbit splitting is directly proportional to the angular momentum l (larger for higher l). Figure [2.1] shows the resulting energy levels splitting as a result of different potentials and the interaction that is considered.

A more sophisticated treatment of the shell model requires a many-body approach. The nucleus is described by $(H_0 + V)\psi = E\psi$ where V is the nucleon-nucleon interaction. We can expand the wave function as

$$|\psi\rangle = \sum_{i=1}^{\infty} a_i \left| \psi_i^{(0)} \right\rangle, \qquad \left\langle \psi_i^{(0)} \middle| \psi_j^{(0)} \right\rangle = \delta_{ij} \ ; \tag{2.13}$$

where the unperturbed wave function is defined by $H_0 \left| \psi_i^{(0)} \right\rangle = E_i^{(0)} \left| \psi_i^{(0)} \right\rangle$. Since every nucleon interact with everyone else, it become practically impossible to solve directly for the nuclei with approximately $A \geq 12$. Therefore we simplify with the shell model approach, where only the valence nucleons (separate for π and ν) describe the nucleus (inspired by how elements are described by the valence electrons).

More specifically, only the particles outside a core made up of filled shells (valence particles) are considered to be active in this truncated Hilbert space, the so-called model space. If you have a full Hilbert space with a realistic potential V and a true wave function ψ, the shell model is basically a reduction of this into reduced model space, with an effective interaction V_{eff} and a model wave function ψ'. This gives

$$\langle \psi' | H_{eff} | \psi' \rangle = E, \qquad H_{eff} = H_0 + V_{eff}. \tag{2.14}$$

This means that for each model space we have to find a suitable effective interaction V_{eff}. If one more orbital is included in model space, we have to find a new V_{eff}. Although, the model wave function ψ' is used instead of true wave function ψ as shown in Equation [2.14], the main goal is to find the correct energies. This can be accomplished either by using a realistic effective nucleon-nucleon interaction from perturbation theory or by finding an effective interaction from fitting experimental data. This seems to work for simple systems with a few nucleons outside a doubly magic core. But if we have many valence nucleons, open-shell nuclei become collective and deformed. Thus, the next step is to include deformation of nuclei, considering both macroscopic and microscopic effects together.

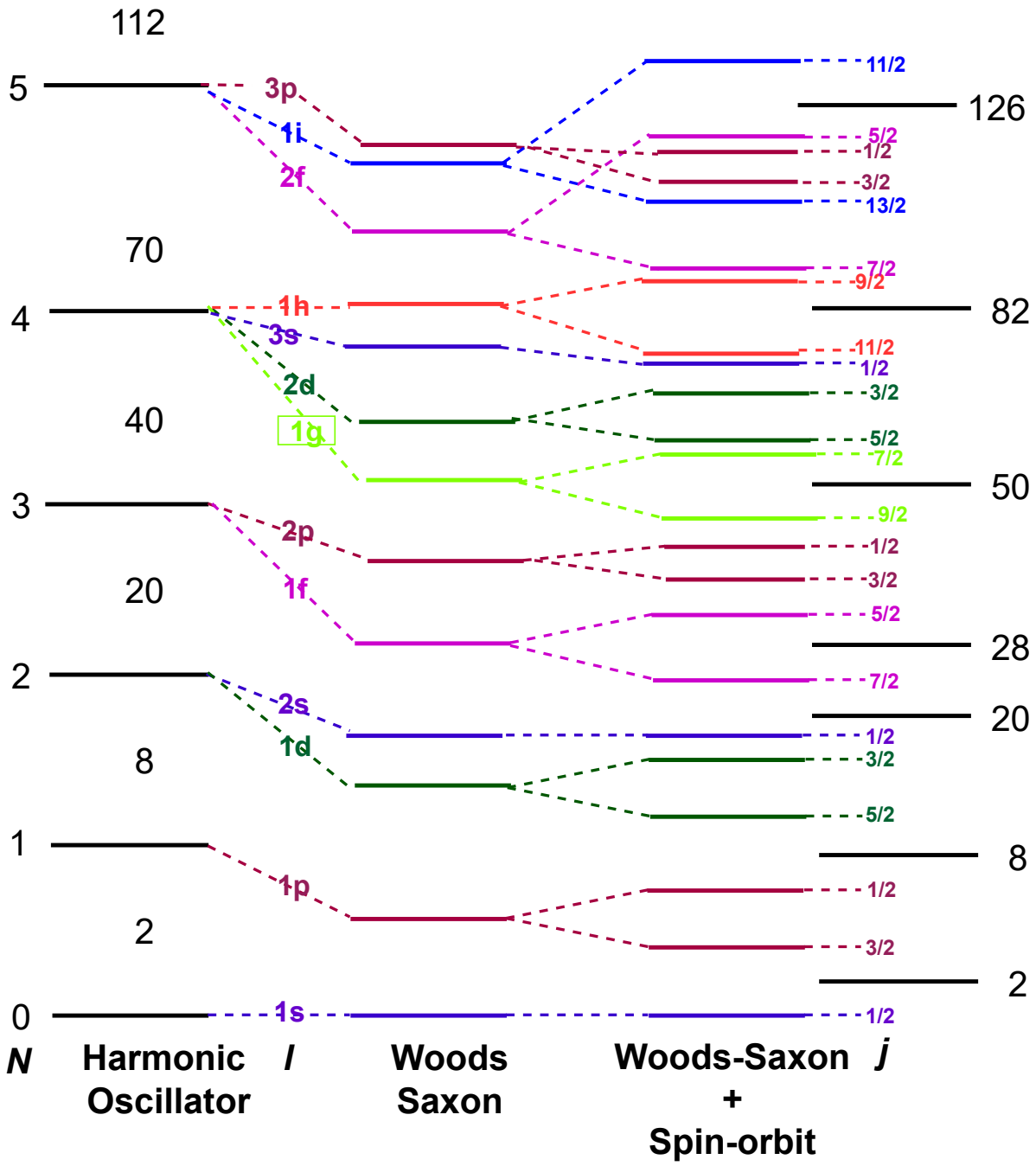

Figure 2.1. The Shell Model prediction of the magic numbers. Level splittings are due to harmonic oscillator(on the left), Woods-Saxon potential(on the center), and a strong spin-orbit interaction to the Woods-Saxon potential(on the right). l is the orbital quantum number, N is the principal quantum number and j is the total angular momentum. The details of the variation of the levels can be found in Ref [[9] Fig: 5.6]. Here only the shiftings leading to new shell groupings are shown.

2.2 The Evolution of the Shell Structure in Exotic Nuclei

The nucleon magic numbers (2, 8, 28, 50 and 82, as well as 126 for neutrons) are the most fundamental quantities reflecting the shell structure in atomic nuclei and were considered to be valid all over the nuclear chart within the nuclear shell model since 1949 [10]. In recent years, investigations at radioactive ion beam facilities have revealed that major shell closures and magic numbers may change in nuclei far from stability due to large neutron-to-proton asymmetry [11]. The evolution of the magic number when moving away from stability is a

more recent question. The so-called shell evolution has been already verified in light mass regions, for example, the disappearance of the neutron N=20 shell gap in ^{31}Na and ^{32}Mg [12, 13] and the appearance of the new shell gaps N=32, 34 in the neutron-rich ^{52,54} Ca isotopes [14, 15]. These results provided clear evidence that magic numbers are not universal, and may differ from those traditional ones when moving far away from stability.

The evolution of the major shells is strongly related to certain properties of the (residual) interactions between nucleons. Among them, the monopole part of the nucleon-nucleon interaction, in particular, its tensor component was found to be responsible for the changes in the location of the single-particle orbitals [16]. Figure [2.2(a)] shows the attractive and repulsive effect of the tensor interaction on given orbitals. It is strongly attractive between two orbits with spins $j_< = l - 1/2$ and $j'_> = l' + 1/2$ and repulsive between two with spins $j_> = l + 1/2$ and $j'_> = l' + 1/2$ where l and l' denote orbital angular momenta for protons and neutrons, respectively. Figure [2.2(b)] shows the effect of this attractive and repulsive tensor interaction in the proton single-particle orbitals in the ^{78}Ni region. The $g_{9/2}$, $f_{7/2}$ and $p_{3/2}$ corresponds to the $j_>$ coupling, while $g_{9/2}$ $f_{5/2}$ corresponds to $j_<$. The interaction between $g_{9/2}$ and $f_{5/2}$ is attractive because of which $f_{5/2}$ is lowered as more neutrons are added to $g_{9/2}$. In contrast, the interaction between $g_{9/2}$ neutrons and both $f_{7/2}$ and $p_{3/2}$ protons is repulsive which causes the energy of the $f_{7/2}$ and $p_{3/2}$ orbitals increases as neutrons are added to $g_{9/2}$. As a consequence, the Z = 28 shell gap gets smaller and the $f_{7/2}$ and $p_{3/2}$ orbitals eventually cross.

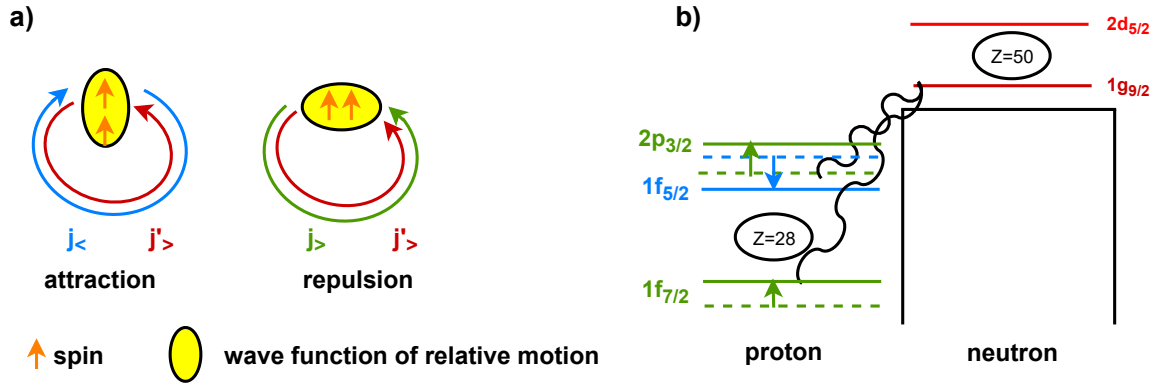

Figure 2.2. (a): Schematic illustration of the attractive and repulsive tensor force acting two nucleons on respective orbits. (b): Schematic illustration of shell evolution because of monopole interaction produced by the tensor force between a proton in $1f_{7/2}, 1f_{5/2}, 2p_{3/2}$... and a neutron in $1g_{9/2}$.. Figure adapted from Ref: [16].

The proton single-particle energies as a function of neutrons in the $1g_{9/2}$ orbit can be determined via single-proton excitations to the shell orbits under study. Figures [2.3] show the proton effective single-particle energy (ESPE) as function of neutron number for Ni isotope chain from two different publications and both are based on shell model calculations. For the later one [17], the effective interaction was refined using experimental data for ^{77}Cu. Figure [2.3 (a)], as reported in 2005 in the work of T. Otsuka [16], the inversion of the $\pi 2p_{3/2}$ and $\pi 1f_{5/2}$ orbits occurs around the mid of the shell at N=45. The experimental results on the low-lying single-particle states on ^{77}Cu show (E. Sahin et al., (2017)) [17] the occurrence of inversion of the $\pi 2p_{3/2}$ and $\pi 1f_{5/2}$ orbits at N=48. To determine the shell gap and how much the level cross when moving away from stability as well as to improve the theory, experimental results on the neutron-rich nuclei near ^{78}Ni are paramount important. In this context, the study of neutron-rich ^{77,79}Zn isotopes, having two more protons than ^{78}Ni, will contribute towards the understanding of the shell evolution and magicity of ^{78}Ni and of the structure of nuclei in the region.

The study of the even-mass Zn isotopes [18, 19] has shown how collectivity and deformation evolves as N=50 is approached. In the odd-mass Zn nuclei, one can potentially study three different types of states: neutron single-particle (or rather hole) excitations, neutron excitations across the N=50 gap, and states based on the coupling of the neutron holes to excitations of the even-even core. Similar to the present thesis work here, an intermediate-energy Coulomb excitation experiment on the $^{73-75}$Ni nuclei was performed at RIKEN [20]. The observed large B(E2) values in ^{73,75}Ni could be related to the proton excitations across the Z=28 gap starting from the mid-shell or could be due to increased number of neutron excitations across the N=50 shell gap. The Coulomb excitation of ^{77}Cu from the same experiment subject to this thesis work instead, indicated a particle-core coupled character of the observed state at 946 keV. This was already predicted from the shell model calculations in Ref.[17, 18]. Finally, the study of collective properties in odd-mass nuclei in the ^{78}Ni region is very important for identifying the nature of the observed states via different excitation mechanisms.

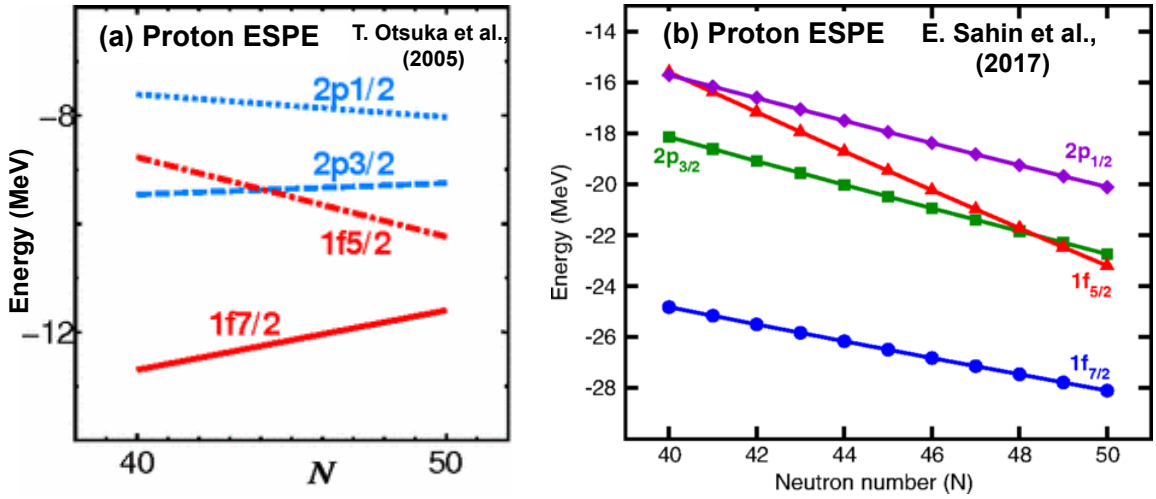

Figure 2.3. Calculated effective single particle energies for the Ni isotope chain. Figures taken from references [16, 17] respectively.

2.3 Nuclear Shapes and Deformation

Different shapes have been observed in the atomic nuclei depending upon the neutron-to-proton ratio and on the conditions of the excitation energy or the spin of the nuclei. The developments of γ-ray detector arrays have become a crucial innovation to the study of nuclear shapes, in particular to high angular momenta. Contrary to nuclei near closed shells,, the collective motion of many nucleons is the origin of deformation and has to be included to explain the nuclear properties of nuclei far from closed shells.

With the expansion of the spherical harmonics, the radius R as a function of θ and ϕ of a deformed nucleus can be expressed as:

$$R(t) = R_0\left[1 + \sum_{\lambda}\sum_{\mu=-\lambda}^{+\lambda} a_{\lambda\mu}(t)Y_{\lambda\mu}(\theta,\phi)\right] \tag{2.15}$$

where R_0 is the radius of the sphere with the same volume and the constant a_{00} describes changes of the nuclear volume. For $\lambda = 1$ dipole vibration we have the translation of the whole system which does not contribute to the vibration of the nuclear surface, i.e. R(t). For $\lambda = 2, 3, 4$

however, we get the quadrupole, octupole and hexadecapole deformed shapes, respectively. If we look for the quadrupole shape ($\lambda = 2$), we have five parameters $a_{2\mu}$, only two of them describe the shape of the nuclei and the remaining three describe the orientation in space (the three Euler angles). The two independent parameters that describe the nuclear shapes are a_{20} and a_{22}:

$$a_{20} = \beta cos\theta \qquad a_{22} = \frac{1}{\sqrt{2}}\beta sin\gamma \tag{2.16}$$

where β describes the axial deformation and γ describes the triaxial deformation. Figure [2.4] shows the nuclear shapes described by a_{20} and a_{22}. Three axially symmetrical shapes, the spherical, prolate, and the oblate and a non-symmetrical triaxial shape is shown respectively in figure.

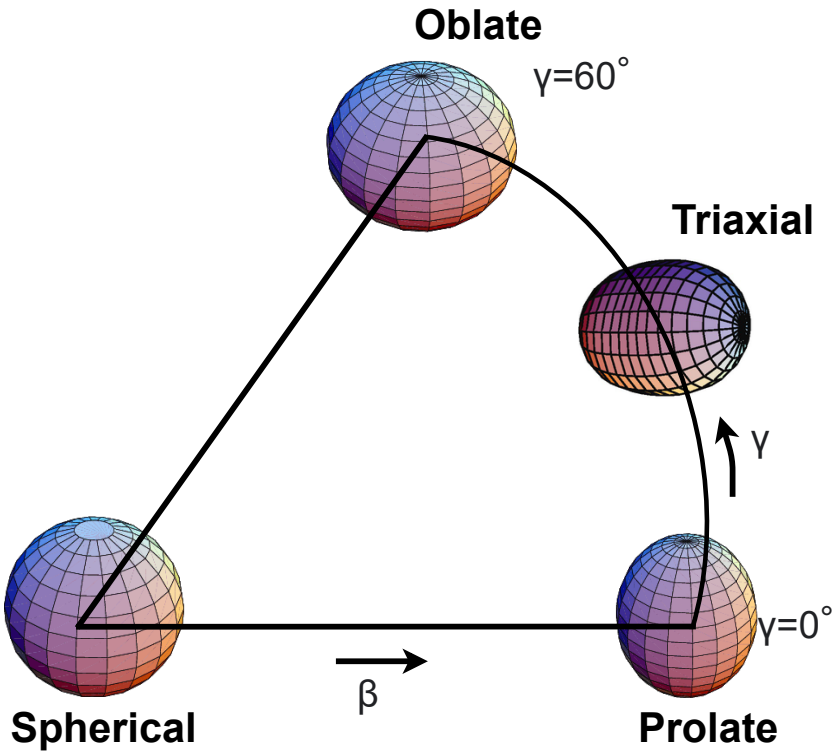

Figure 2.4. The β and γ parameters in deformation.

Deformation can be dynamic and studied in different ways. One way to study the deformed shapes is using the collective models where the nuclei either rotate or vibrate. The differential equation for the harmonic oscillator for quadrupole vibrations

$$\frac{dH}{dt} = B\frac{d^2a_{2\mu}(t)}{dt^2} + Ca_{2\mu(t)} = 0 \tag{2.17}$$

where B is the inertia parameter and C the restoring force of vibration. Each $a_{2\mu}(t)$ is oscillating with the frequency $\omega = \sqrt{\frac{C}{B}}$. Using creation and annihilation operators we get different phonon

states

$$|\psi(n_{2\mu}=1)\rangle = b^{\dagger}_{2\mu}|0\rangle, one-phonon\ \ state$$
$$|\psi(n_{2\mu}=2)\rangle = \frac{1}{\sqrt{2}}b^{\dagger}_{2\mu}b^{\dagger}_{2\mu}|0\rangle, two-phonon\ \ state$$
$$|\psi(n_{2\mu}=N)\rangle = \frac{1}{\sqrt{N}}(b^{\dagger}_{2\mu})^{N}|0\rangle, N-phonon\ \ state$$

This gives Hamiltonian as

$$H = \hbar\omega \sum_{\mu=-2}^{2}\left(b^{\dagger}_{2\mu}b_{2\mu} + \frac{1}{2}\right), \tag{2.18}$$

with energies of an N-phonon state as

$$E_N = \hbar\omega\left(N + \frac{5}{2}\right), \tag{2.19}$$

getting evenly distanced levels with $\hbar\omega$ energy difference between each level. For each multipolarity, λ you get $2\lambda+1$ parameters $a_{\lambda\mu}$, where $2\lambda-2$ are the intrinsic vibrational modes, and the remaining 3 degrees of freedom are rotational modes about the three axes. A quadrupole phonon carries $I^{\pi}=2^{+}$ angular momentum and parity, and an octupole phonon would carry $I^{\pi}=3^{-}$. Two phonons of multipolarity λ can couple to states of different angular momentum. The coupling of two quadrupole phonons produces states with I^{π} = $4^{+}, 2^{+}, 0^{+}$. Three quadrupole phonons can couple to $6^{+}, 4^{+}, 3^{+}2^{+}, 0^{+}$. We can look for candidates for vibrational nuclei near (but not at) shell closures. This would be nuclei that are not very deformed, but are a bit "soft" and vibrate around a ground state spherical shape. There we look for nuclei with $\frac{E(4^{+})}{E2^{+}}$ = 2 and $\frac{B(E2;4^{+}\rightarrow 2^{+})}{B(E2;2^{+}\rightarrow 0^{+})}$ = 2. Also, we would expect a ratio between 4^{+} and 2^{+} energies of rotational bands to be $\frac{E(4^{+})}{E2^{+}}$ = 3.33.

We can couple vibration and rotation, and the results are an expression for the kinetic energy as

$$T = \frac{1}{2}B(\dot{\beta}^2 + \beta^2\dot{\gamma}^2) + \frac{1}{2}\sum_{k=1}^{3}\mathcal{J}_{\kappa}\omega_{\kappa}^2 \tag{2.20}$$

where $\mathcal{J}$, is the moment of inertia. The first term describes the vibrational energy, whereas the second term describes the rotational energy. ω_{κ} is the angular velocity of the body-fixed axes with respect to the space-fixed axes of the laboratory. The moment of inertia is expressed as

$$\mathcal{J}_{\kappa} = 4B\beta^2\sin^2\left(\gamma - \frac{\kappa 2\pi}{3}\right) \tag{2.21}$$

which shows that for β = 0 we have no rotations, and similarly for some γ values. This shows the nucleus cannot rotate about a symmetry axis.

2.4 Electromagnetic Transitions

2.4.1 Gamma Decay

The excited nucleus may lower its energy by γ-ray emission, β decay, conversion electron emission, or fission. Gamma decay is a radioactive decay process where an excited nucleus emits electromagnetic radiation in the form of energetic gamma photons instead of particles such as neutrons or protons. Gamma-decay can be categorized as electric or magnetic multipolarity depending on the spins and the parities, π, of the connected states. Considering the γ transition from an initial excited state of angular momentum I_i and parity π_i to the final state I_f and the parity π_f, the excitation is defined by certain selection rules on angular momentum and parity. The allowed multipolarities are restricted by:

$$|J_f^\pi - J_i^\pi| \leq \lambda \leq |J_f^\pi + J_i^\pi| \tag{2.22}$$

where λ is the multipole order of the emitted radiation. Based on the parities of the initial and the final states, π_i and π_f, the transition is further classified as electric or magnetic:

$$\pi_i\pi_f = \begin{cases} (-1)^\lambda & for \quad E\lambda \rightarrow \quad electric \;\; decay \\ (-1)^{\lambda+1} & for \quad M\lambda \rightarrow \quad magnetic \;\; decay. \end{cases} \tag{2.23}$$

where $\lambda \neq 0$, which means that $0^+ \rightarrow 0^+$ is forbidden via single γ-ray decay since the photons are bosons with spin = 1 and they must carry at least one unit of angular momentum. There are a few examples of even-even nuclei that have first excited and ground states that are both 0^+. Once populated, these states decay by the internal conversion processes, via atomic electrons with significant penetration into the nucleus, and are directly emitted from the atom. Transition with the lowest possible multipolarity is always preferred and for the same multipolarity, $E\lambda$ will always be preferred over $M\lambda$. In intermediate-energy Coulomb excitation experiments, for a given even-even nucleus, the first excited 2^+ state is expected to be populated while multiple excitations, i.e. excitations within a $2^+ \rightarrow 4^+ \rightarrow 6^+$... cascade are highly suppressed due to the large incoming beam energy ($\approx$ 200 MeV/u). In the current analysis both ^{77}Zn and ^{79}Zn nuclei are odd-even nuclei and rather exotic. Thus, it is highly possible that the spin-parity of the first excited state is unknown. Furthermore, the states do not carry E2 multipolarity, but the transitions that connect the excited states with the ground state. In such cases, gamma-ray angular distributions, where possible, could give necessary information about the spin of the observed states. For exotic nuclei, where the collected data are not sufficient for such analysis, shell model calculations provide a good basis for the spin assignment of the observed states. Gamma-decay selection rules are considered and the selection rules are presented in Table [2.1].

TABLE 2.1. The γ-decay selection rules.

$\|\Delta J\|$	0	1	2	3	4
$\Delta\pi$ = yes	E1 (M2)	E1 (M2)	M2 E3	E3 (M4)	M4 E5
$\Delta\pi$ = no	M1 E2	M1 E2	E2 (M3)	M3 E4	E4 (M5)

2.4.2 Electrostatic Multipoles

In classical field theory, electromagnetic multipoles appear as a result of the multipole expansion of the fields created by a finite system of charges and currents. For the system with point-like classical particles with electric charge e_i located at the points r_i, the Coulomb potential is written as [21]

$$V(r) = \sum_i \frac{e_i}{|r - r_i|} \tag{2.24}$$

Expanding this function with Legendre polynomials with multipole expansion, a general form of the multipole moment can be obtained as:

$$V(r) = \sum_{LM} \frac{4\pi}{2L+1} \frac{1}{r^L + 1} Y^*_{LM}(n) \mathcal{M}(EL, M) \tag{2.25}$$

Here the electric multipole moments of rank L, is defined for a system of point-like charges i = 1,2,3... A as a set of (2L+1) quantities

$$\mathcal{M}(EL, M) = \sum_i e_i r_i^L Y_{LM}(n_i), \tag{2.26}$$

By introducing the charge density operator

$$\rho(r) = \sum_i e_i \delta(r - r_i), \tag{2.27}$$

a more general form of the multipole moments can be obtained as,

$$\mathcal{M}(EL, M) = \int d^3 r \rho(r) r^L Y_{LM}(n) \tag{2.28}$$

In a similar way, the magnetic multipoles $\mathcal{M}(ML, M)$ related to the distribution of the current can be defined as:

$$\mathcal{M}(ML, M) = \sum_i \left(g_i^s s_i + \frac{2}{L+1} g_i^L l_i \right) . \nabla \left(r_i^L Y_{lM}(n_i) \right). \tag{2.29}$$

where s_i and l_i are spin and orbital angular momentum, g_i^s and g_i^L are the gyromagnetic factors of the spin and orbital angular momentum, respectively, of a particle i.

The probability for the radioactive decay between initial transition i and the final transition f is given by:

$$\omega_{fi} = \frac{8\pi(L+1)}{L[(2L+1)!!]^2 \hbar} \kappa^{2L+1} \times \sum_{LM} \left\{ \left| \left(\mathcal{M}(EL, M) \right)_{fi} \right|^2 + \left| \left(\mathcal{M}(ML, M) \right)_{fi} \right|^2 \right\} \tag{2.30}$$

with $\kappa = \omega/c$, and $\omega = (E_f - E_i)/\hbar$. The reduced transition probability can be defined as

$$B(EL; i \to f) = \sum_{MM_f} \left| \left(\mathcal{M}(EL, M) \right)_{fi} \right|^2 \tag{2.31}$$

By using the Wigner-Eckart theorem, the reduced transition probability is then related to the reduced matrix element of the multipole operator,

$$B(EL; i \to f) = \frac{1}{2J_i + 1} \left| \langle f || \Big(\mathcal{M}(EL) \Big)_{fi} || i \rangle \right|^2 \tag{2.32}$$

For inverse transition induced by the same operator, it is calculated as:

$$B(EL; f \to i) = \frac{2J_i + 1}{2J_f + 1} B(EL; i \to f) \tag{2.33}$$

The reduced transition probability can be used to calculate the partial life time of a given initial state with respect to specific radiative decay,

$$\frac{1}{\tau_{i \to f}} = \sum_{M_f} \omega_{fi} = \frac{8\pi}{\hbar} \frac{L+1}{L[(2L+1)!!]^2} \kappa^{2L+1} B(EL; i \to f) \tag{2.34}$$

With the substitution of $EL \to ML$ the same expression [2.34] is valid for magnetic multipoles. Depending on the energy regimes of the ion-ion collision, the probability that the Coulomb excitation process occurs has to be analyzed separately for three different cases: the low energy collisions (5-10MeV), relativistic collision (>500MeV) and the intermediate-energy collision (20-300MeV). At low energies, one uses Rutherford trajectories [22] while at relativistic energies one uses straight lines for relative motion [23, 24]. In this thesis work, I will briefly mention the intermediate-energy collision.

2.5 Experimental Technique

The main aim of the present experiment is to determine the B(E2) value of excited states. For even-even nuclei, it is only possible to reach the first excited 2^+ state, but in odd-even nuclei it is possible to excite several states at intermediate beam energies. However, the study of the exotic nuclei close to the neutron drip-line in the laboratory is challenging. In such a case, the use of large beam velocity enables us to use thick secondary targets which in turn, will increase the number of secondary reaction products in in-beam γ-ray experiments. Furthermore, it is important to choose an appropriate reaction that results in sufficiently a large cross-section, thus the large number of γ rays to make experimental measurement feasible. The relationship between the number of reactions taking place ($N_{reaction}$) and the number of γ-rays detected (N_γ) is given by [25]:

$$N_{reaction} = \frac{N_\gamma}{\epsilon} = \sigma \times N_{target} \times N_{beam} \tag{2.35}$$

where N_{beam} is the number of beam particles impinging onto the target, ϵ is the γ-ray detection efficiency, and σ is the cross-section to be determined. The use of the thicker targets translates directly into an increase in the number of reactions $N_{reactions}$ and the number of detected γ-rays. For exotic nuclei, where beam intensities are low, it can be an advantage to perform measurements at higher energies where one can use thicker targets. The Coulomb excitation of radioactive ion beams at intermediate energies on high-Z, thick targets allow us to measure transition matrix elements with beam rates as low as a few particles/s. The major task of this experiment is to determine the cross-section σ in [2.35] under well-controlled conditions, accurately, and with documented precision.

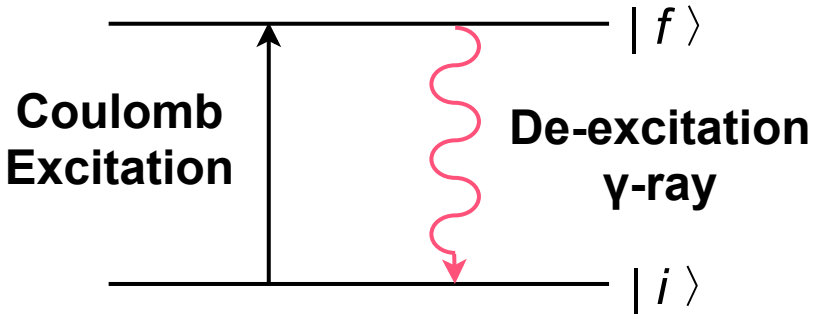

Figure 2.5. Schematic illustration of first-order Coulomb excitation followed by de-excitation γ-rays from the bound excited state. The nucleus in its ground state $|i\rangle$ is Coulomb excited into final state $|f\rangle$, which then γ-decays back to the ground state $|i\rangle$.

Since the Coulomb excitation cross-section $\sigma_{i\to f}$ from an initial state $|i\rangle$ to final state $|f\rangle$ in equation [2.35] can be determined by measuring the γ-ray yield $I_{f\to i}$ for the de-excitation $|f\rangle \to |i\rangle$, it is important to assess contributions to this yield which are not proportional to the excitation cross section. The decay of the state is electromagnetic. If the excitation of the state is purely electromagnetic, the extraction of the cross section is straightforward. If the excitation has contributions from both electromagnetic and nuclear excitation, it is more complicated. Either we have to exclude any nuclear contribution, or we have to determine how strong this contribution is. By choosing a heavy target and small scattering angles, we can ensure that electromagnetic excitation is dominating. We then use a light target (carbon, for which electromagnetic excitation is weak) to determine the strength of the nuclear contribution. The schematics of the excitation and de-excitation process are illustrated in Figure [2.5]. For the measurement of emitted γ-rays from the projectile and the target, a suitable detector array is needed. Because of the Doppler effect, it is complicated to observe the γ-ray without doing proper Doppler correction. Also, the γ-ray spectrum is contaminated by atomic and Compton background. Considering all these conditions, the most convenient process to excite nuclei of such a beam is through scattering on a heavy target via the electromagnetic interaction. This process is called the Coulomb excitation process and is explained in next section.

2.5.1 Coulomb Excitation

Intermediate-energy Coulomb excitation has become one of the advanced modern techniques for measuring specific observables that can be compared with theoretical calculations. With the advancement in the exotic beam intensities, the modern development of the experimental technique and the corresponding detectors and with the development of theories and respective computational tools, the understanding of the evolvement of the nuclear shell structure

towards the nuclear drip-line has significantly improved. The Coulomb excitation technique is very useful since the interaction mechanism between the projectile and the target is well-known. Since the strength of the Coulomb interaction is proportional to the charges of the nuclei involved in the process, and because large secondary-beam energies allow the use of very heavy targets (usually gold or lead) to increase the Coulomb strength. This technique was used extensively to study the electromagnetic transition strength using low-energy (5-10 MeV/u) stable and radioactive ion beams since 1950s [26]. Also low-energy Coulomb excitation is used with RIB today. (30-300 MeV/u) is in use at different radioactive ion beam facilities instead of stable beams and targets.

2.5.2 Coulomb Excitation Process

Coulomb excitation is a process of inelastic scattering in which a charged particle transmits energy to the nucleus through an electromagnetic field. This technique provides an electromagnetic probe that is sensitive to the internal structure of the nuclei involved. The scattered projectiles are detected at small scattering angles in coincidence with γ-rays emitted from the target nucleus (which is at rest or slowly recoiling in the laboratory) and the projectile which is moving with close to beam velocity slowed down only by energy loss in the target [25]. Detection of the scattered projectile at a small scattering angle is true for intermediate-energy Coulomb excitation, where one tries to exclude nuclear excitation by limiting the scattering angle and hence the distance of the closest approach. For low-energy Coulomb excitation, one tries to measure for large scattering angles, where there is a higher probability for multi-step excitation. The scattering process is schematically illustrated in Figure [2.6]. The beam particle gets excited by the electromagnetic interaction with the target particle. It is at the same time also possible that the target nucleus gets excited. The excited energy state is unstable and it will rapidly de-excite with the emission of the γ-ray. The scattering angle and impact parameter are defined as shown in the figure. The projectile is scattered with scattering angle θ as shown in the figure. A small scattering angle θ means forward scattering of the beam, a larger distance between the beam particle and the target particle, a weaker electromagnetic field and a decreased excitation probability. A large scattering angle θ means the backward scattering of the beam, a closer distance between the beam particle and the target particle, a stronger electromagnetic field and a higher excitation probability. It is assumed that the nuclei follow classical Rutherford trajectories in the determination of the Coulomb excitation probability. The Coulomb excitation cross-section is given by:

$$\left(\frac{d\sigma}{d\Omega}\right)_{Ruth} = \left(\frac{a_0}{2}\right)^2 \sin^{-4}\left(\frac{\theta}{2}\right) \tag{2.36}$$

where a_0 is the classical distance of closest approach and is given by

$$a_0 = \frac{Z_1 Z_2 e^2}{4E} \tag{2.37}$$

E is the kinetic energy and is assumed to be large enough so that we can neglect the feedback from the intrinsic excitations to relative motion. θ is the scattering angle, $Z_1 e$ and $Z_2 e$ are the charge of the projectile and target respectively. a_0 is larger than $R_1 + R_2$ at relative energy lower than the Coulomb barrier

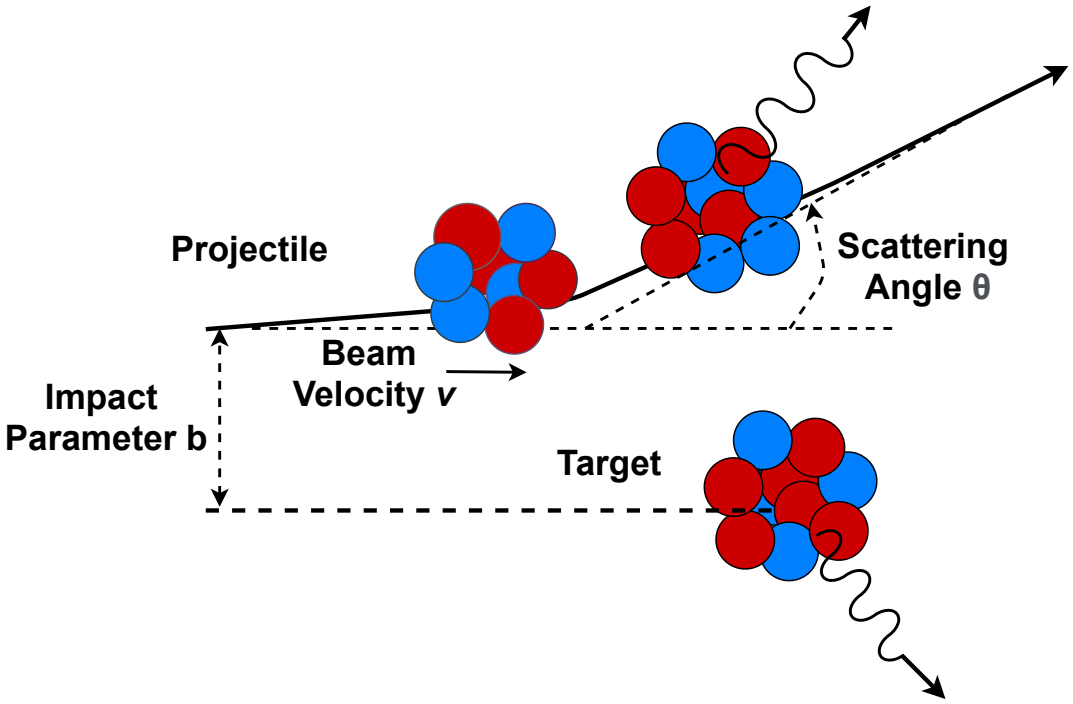

Figure 2.6. Schematic illustration of the intermediate-energy Coulomb excitation process. The projectile is scattered by an angle θ impinges on heavy target at an impact parameter b with velocity v. Figure adapted from [25].

$$E_B = \frac{Z_1 Z_2 e_2}{R_1 + R_2} \tag{2.38}$$

The probability of intrinsic excitation for the Coulomb excitation of a nuclear state $|f>$ from an initial state $|i>$ is determined by the presence in this field of Fourier harmonics with the excitation frequencies

$$\omega = \frac{E_f - E_i}{\hbar} \tag{2.39}$$

If the motion is too slow, the field acts adiabatically, the intrinsic wave function is changing reversibly and the probability of excitation is low. The corresponding adiabaticity parameter is the ratio ξ of the time scales for the Coulomb collision, $\approx \frac{a_o}{v}$, and for the nuclear excitation, $\approx \frac{1}{\omega}$ [21]:

$$\xi = \frac{\omega a_o}{v} \tag{2.40}$$

When ξ>1, the situation is adiabatic and the transition probabilities are small.

This treatment is valid in almost all situations studied in Coulomb excitation at low energies [22]. For high energy collisions, because the nuclear interaction distorts the scattering waves appreciably, a quantum treatment is essential for some observable, e.g. angular distributions.

2.5.3 Intermediate-energy Collision

In the semiclassical theory of Coulomb excitation at low energy collision, the Rutherford bending is accounted, however, relativistic retardation effects are still neglected. Therefore, in intermediate energy collision, one wants to account for the recoil and retardation simultaneously to solve the general classical problem of the motion of two relativistic charged particles. This has been studied in detail in Reference [27, 28]. Considering the importance of relativistic effects at intermediate energies, one has to consider two relativistic charged particles moving with respect to each other. However, at the same time, the straight-line trajectories can no longer be considered. This is schematically illustrated in Figure [2.6] where the target nucleus does not recoil. The impact parameter b was rescaled to account for the recoil of the target as the first-ordered deviation from straight-line trajectories and is given by [29]:

$$b \rightarrow b + \frac{\pi a}{2\gamma}, \tag{2.41}$$

where γ is the relativistic Lorentz factor $\gamma = 1/\sqrt{1-\beta^2}$ and a is a half distance of closest approach in a non-relativistic head-on collision. It is expressed as

$$a = \frac{Z_{projectile} Z_{target} e^2}{m_0 \beta^2 c^2} \tag{2.42}$$

where, $Z_{projectile}$ and Z_{target} are the charges of projectile and target respectively. β is the beam velocity relative to the speed of light and m_0 is the reduced mass of the projectile-target system. The Coulomb excitation cross section as a sum of the allowed multipole matrix elements of the electromagnetic decay of the nuclear state $|f>$ to $|i>$ is [26]

$$\sigma_{i\rightarrow f} = \sum_{\pi\lambda} \sigma_{\pi\lambda}. \tag{2.43}$$

The Coulomb excitation cross-section for an electromagnetic excitation of a state including the relation to the reduced transition probabilities, including multipolarity λ and the parity π for a single line trajectories with impact parameter greater than b_{min} as [25]:

$$\sigma_{\pi\lambda} \approx \left(\frac{Z_p e^2}{\hbar c}\right)^2 \frac{\pi}{e^2 b_{min}^{2\lambda-2}} B(\pi\lambda, 0 \rightarrow \lambda) \begin{cases} (\lambda-1)^{-1} & :for \quad \lambda \geq 2 \\ 2ln\left(\frac{b_a}{b_{min}}\right) & : \quad for\lambda = 1. \end{cases} \tag{2.44}$$

where b_a is the impact parameter where the adiabatic cutoff of the Coulomb excitation process sets in. The cutoff of the Coulomb excitation is possible when the nucleus $\hbar/E_\gamma$ equals the collision time $b_a/(\gamma c\beta)$. Here E_γ is the energy of the excited state $|f>$ relative to the initial state $|i>$. Also,

$$b_a = \frac{\gamma \hbar c \beta}{E_\gamma}. \tag{2.45}$$

The maximum energy of the final states that can be excited in the collisions with impact parameter b is

$$E_{\gamma}^{max} \approx \frac{\gamma \hbar c \beta}{b}. \tag{2.46}$$

Equation [2.44] shows the linear relation between the Coulomb excitation cross-section and the reduced transition probability matrix element. Because of the proportionality relationship between the cross-section (σ) and B(E2), the reduced transition probabilities can be obtained from measurements of Coulomb excitation cross-sections via the calculation of the cross-section yields.

Chapter 3

Experimental Setup

If your result needs a statistician then you should design a better experiment.

ERNEST RUTHERFORD

The experiment reported in this thesis was conducted at the Radioactive Ion Beam Factory (RIBF), RIKEN, Japan. It took place in April, 2015 and lasted for four days. The main purpose of the experiment was to study the collective properties of the neutron-rich ^{77}Cu nucleus via Coulomb excitation. However, in addition to ^{77}Cu, ^{77,79}Zn isotopes were produced simultaneously and also present in the cocktail beam. The experimental setup consists of the BigRIPS and the ZeroDegree fragment separators for particle identification and the DALI2 gamma array for the detection of gamma rays emitted from the reaction products. Details of the experimental setup will be discussed in this chapter.

3.1 Radioactive Ion Beams

To facilitate the study of the isotopes that have a neutron-to-proton ratio very different from the stable isotopes, the production and study of the radioactive ion beams (RIBs) have resulted as an advanced technology over the last decades. Being far away from the valley of beta stability, these so-called exotic neutron-rich nuclei are difficult to study experimentally because of small cross-sections, short half-lives, simultaneous production of less exotic nuclides at the same time in the same nuclear reaction. There are two techniques: (i) Isotope separation on-line (ISOL) with the thick target, ionization and extraction of the wanted species (chemistry dependent and relatively slow), and post-acceleration; (ii) in-flight method, with thin target and subsequent electromagnetic separation (independent of chemistry and fast). ISOL usually produces higher-quality beams. Beams produced by the in-flight method often have a wider energy spread, but because the method is faster, more exotic species can be produced.

The in-Flight technique is characterized by the kinematics focusing conservation of linear

momentum at small angles around the primary beam direction of the reaction product and allow for fast separation of the exotic species. A stable projectile is accelerated to several hundreds of MeV/u and collides with a stable primary target. Radioactive beams of a wide variety of neutron-rich elements are produced by this method. This technique is independent of the chemical properties of the produced isotopes, and the selection of radioactive beam of interest can be performed through the deflection of ions in the magnetic and electric fields. A detailed description of the in-flight technique can be found in the review article [30]. Recently, there are several facilities worldwide which employed in-flight techniques for particle identification and separation with projectile fragmentation and fission methods. These are mainly GSI Germany [31], GANIL in France [32], NSCL-MSU in USA [33], RIKEN Nishana center in Japan [34]. This project work relies on the experimental data analysis of the data from Radioactive Ion Beam Factory (RIBF), RIKEN Nishana Center. Currently, the RIBF provides primary beams of very high intensity, which allows producing very exotic secondary beams even when their production cross-section is low. The RIBF, RIKEN Nishina Center is used for achieving excellent resolving power in in-flight particle identification of the radioactive isotopes beams at the BigRIPS and ZeroDegree fragment separator [35].

3.2 Production of Primary Radioactive Ion Beam at RIKEN Nishina Center

The RIBF, RIKEN became operational from March 2007 with all the experimental setup for the study of the so-called exotic nuclei, far from the valley of stability. The production of the RI beam is based on the in-flight technique with superconducting recoil separator BigRIPS [34, 36, 37] to separate the ions of interest. Usually, a ^{238}U produces fission fragments for lighter neutron-rich nuclei they start with the most neutron-rich stable isotope, e.g. ^{48}Ca or ^{70}Zn and separate out those fragments where mostly protons were removed. For neutron-deficient nuclei, start with the most neutron-deficient isotope of a given element, and collect fragments where mostly neutrons were removed. In addition, ^{124}Xe beam is most suited for generating proton-rich nuclei in the proximity to the doubly magic nucleus of ^{100}Sn region.

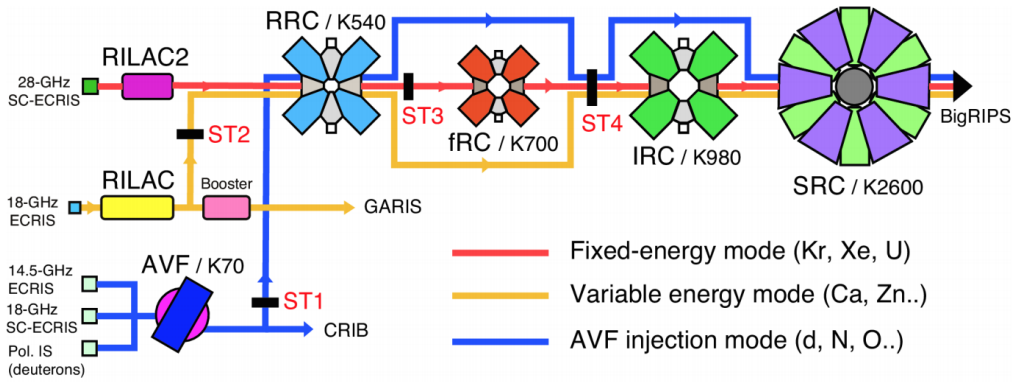

Figure 3.1. RIBF accelerator system for the production of Primary beam at RIKEN. Three different injectors (AVF,RILAC, and RILAC2) followed by four booster cyclotron (RRC, fRC, IRC and SRC) is schematically shown in figure. Figure taken from Ref. [38]. See text for full description.

In this experimental setup, a fixed-energy mode ^{238}U beam was used as a primary beam source with a beam energy 345 MeV/nucleon. This ion beam is generated from a superconducting electron cyclotron resonance (SCECR) ion source and accelerated up to 6 MeV/u using the RIKEN Heavy-ion Linac (RILAC) [39, 40]. The beam is then injected into RIKEN Ring Cyclotron (RRC), the fixed-frequency Ring Cyclotron (fRC) and the Intermediate

Stage Ring Cyclotron (IRC) and finally the Superconducting Ring Cyclotron (SRC). The different modes for the production of the primary beams as shown in Figure [3.1] are [40]:

- Mode 1: AVF + RRC + SRC is used for polarized deuteron beam generation at 880MeV (shown in blue line),
- Mode 2: RILAC + RRC + IRC + SRC is used for variable energy mode (shown in yellow line), and
- Mode 3: RILAC + RRC + fRC + IRC+ SRC is used for fixed-energy mode(shown in red line).

Mode 3 was employed as a necessary condition in our experiment. ^{238}U beam is first of all injected into RILAC. The output of the RILAC is then injected into RRC of an approximate energy 670 keV/u. The output of RRC has an energy approximately 11 MeV/u. After this, the output beam is again injected into IRC, where it can reach a maximum energy of 127 MeV/u. Finally, at SRC the ions are accelerated up to 345 MeV/u. The details of this procedure can be found in reference [40, 41]. Thus generated primary beam from the SRC, is then guided to the BigRIPS and ZeroDegree separator.

3.3 Separation and Identification of the Secondary Radioactive Ion Beams

The experimental condition for this thesis work is that a ^{238}U primary beam of beam energy 345 MeV/u was accelerated to 3 *mm* thick ^{9}Be target in order to produce ^{77}Cu. As mentioned above, ^{77,79}Zn isotopes beam cocktails were also produced at the same time along with ^{77}Cu. In this thesis work, identification of ^{77,79}Zn isotopes in BigRIPS and ZeroDegree will only be briefly explained as the particle identification had already been done prior to this work. In-beam γ-ray spectroscopy of ^{77,79}Zn isotopes via DALI2 array is the major aim of this thesis work. The detailed data analysis process is discussed in Chapter 4, Data Analysis.

3.3.1 BigRIPS Spectrometer

The Big RIKEN projectile-fragment separator (BigRIPS) was build and adopted with the aim of achieving high-intensity RIBs of greater capability, especially those of nuclei far from stability. The major characteristic features of the BigRIPS spectrometer are large acceptances in its ion optics and accounting for the use of in-flight fission. Furthermore, a well-adopted two-stage fragment separator scheme, which when RI-beam purity is poor, eases to tag RI-beam species in event-by-event mode [36, 37]. The schematic of the BigRIPS is shown in Figure [3.2]. It is composed of a two-stage structure namely the first and second stages. The first stage extends from production target (^{9}Be) to F2 focal point and consists of four superconducting quadrupole triplets and two room-temperature dipoles (D1 and D2) with a bending angle of 30°. An achromatic wedge-shaped energy degrader is placed at the F1 focus at an intermediate point to make isotopic separation based on a technique called momentum achromat. The second stage starts from the F3 focal plane till F7 with 8 superconducting quadrupole triplets and 4 room-temperature dipoles (D3-D6). The intermediate focal points F4, F5 and F6 of the second stage are momentum-dispersive, while F7 is fully achromatic. The distance of the first stage is 31.6 m, while that of the second stage is 46.6 m with the total beam line of BigRIPS 78.2 m.

The first stage of BigRIPS is characterized to separate and select the RIB. The beam cocktails of many different isotopes are formed by the fragmentation and fission of the ^{238}U primary beam. Isotopes with different masses and proton-to-neutron ratios are produced during the process and we need to select and identify the nuclei of our interest. Nuclei are selected by a slit at the exit of the dipole magnet. First, the magnetic rigidity ($B\rho \propto A/Q$) of the objective nuclide is selected by the combination of the first dipole magnet and the slit. However, the nuclide which has a similar $B\rho$ with that of objective nuclide cannot be stopped by the slit. Then, the beam passes through the wedge degrader (8 mm) at F1 and loses the beam energy in the degrader depending on the atomic number. After passing the second dipole magnet D2, the slit placed at its exit selects the ion with a certain $B\rho$. The objective nuclide (A, Z) is selected by the combination of the second dipole magnet and the slit. The selected isotopes are transported to the achromatic focal plane F3.

The second stage (F3-F7) is mainly dedicated to the further separation and particle identification of the different isotopes by measuring A/Q and Z by using the momentum-loss-achromatic method ($B\rho - \Delta E - TOF$ separation). A 10mm thick aluminum is placed at F5 focal point for further purification of the beam by removing fragmentation products closer to stability. The 46.6 m long beam line of the second stage is fitted with beam line detectors for measuring the particle trajectory, Energy loss (ΔE), and the Time of Flight (TOF). The plastic scintillation detectors placed at F3 and F7 focus are used to measure the TOF, while the energy loss is measured by using a Multi Sampling Ionization Chamber (MUSIC detector) placed at F7. The Parallel Plate Avalanche Counters (PPACs) placed at F3, F5 and F7 are used to deduce $B\rho$ position measurements. Each of these detectors is clearly shown in Figure [3.2] with their appropriate focal points. Following this two-stage particle identification method, we can deduce the mass-to-charge ratio (A/Q) and the atomic number (Z) of the fragments. After the identification of the particles, thus formed secondary beam was transported to the reaction target and the ZeroDegree Spectrometer.

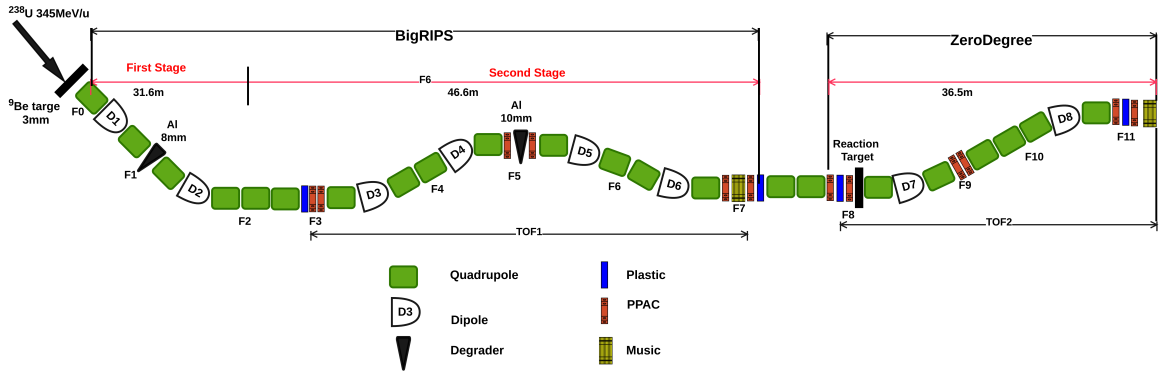

Figure 3.2. Schematic diagram of the BigRIPS and ZeroDegree spectrometers. The two stage structure of the BigRIPS is indicated by the red line. The series of quadrupoles, dipoles and different detectors used in the experiment are also labelled in the diagram. Figure adapted from Ref. [42].

3.3.2 ZeroDegree Spectrometer

The schematic of the ZeroDegree spectrometer is shown on the right side of Figure [3.2]. The main purpose of the ZeroDegree spectrometer is to perform particle identification of the reaction products after the ions pass through the reaction target placed at the F8 focus. It extends from F8 focus (achromatic) to F11 (doubly achromatic) and consists of 6 quadrupoles and 2 diploes (D7 and D8) bending at the angle of 30°. The total length of the beam line of ZeroDegree is 36.5 m long. The reaction target at F8 focus consist of ^{197}Au target of thickness

948 mg/cm^2 and ^{12}C of thickness 903 mg/cm^2. The gold target is employed here mainly to induce the Coulomb excitation of the projectile since the atomic number (Z) of the gold is very high (Z=79). Particle identification in ZeroDegree follows $B\rho - \Delta E - TOF$ method as in BigRIPS. The plastic scintillator detectors placed at F8 and F11 focal planes measure the TOF, the $B\rho$ values are determined from the positions measured at F8, F9 and F11 focal planes and the ΔE is measured with the MUSIC detector placed at F11 focal plane. At F8 focal plane, three PPACs were installed. The two PPACs placed at the F8 focal plane, in front of the target, are used to track the beam and one PPAC that is placed behind the target is used to determine the scattering angle of the ejectiles.

3.4 Beam Line Detectors

The primary beam when passing through the ^{9}Be target follows a path (beam-line direction) with a set of detectors, dipoles, and quadrupoles magnets and the degraders. This section is dedicated to describe the different sets of detectors used along the beam line direction. As mentioned earlier, PPAC, MUSIC and Plastic scintillator detectors were used in the experiments. The position of these detectors in different focal planes and their numbers are shown in Table [3.1] below.

TABLE 3.1. Positions of the detectors used for the particle identification along beam-line direction of BigRIPS and ZeroDegree

Detectors	Focal Planes
MUSIC detector	F7 and F11
Plastic Scintillator	F3, F7, F8 and F11
PPAC(*2)	F3, F5, F7,F9and F11
PPAC(*3)	F8

3.4.1 Multi-Sampling Ionization Chamber (MUSIC)

Two different MUSIC detectors were used, one at the F7 focal plane of BigRIPS spectrometer and the other at the F11 focal plane of the ZeroDegree spectrometer, in this experimental setup. The major task of the MUSIC detector is to measure the energy loss (ΔE) of the incident beam. The energy loss measurement of the beam using the ΔE detector and the velocity measurement (by measuring the time-of-flight) using the PPAC detector are employed for particle identification. The ΔE detectors require an excellent energy resolution, high counting rate capacity, and robustness against beam bombardment. The schematic diagram of the MUSIC detector used in RIBF RIKEN is shown in the Figure [3.3]. It consists of thirteen cathode and twelve anode planes placed alternatively within 2 cm steps. A total of 24 parallel plate ionization chambers are stacked together back to back resulting in a 48 cm thick chamber. The mixture of $Ar(90\%) - CF_4(10\%)$ was mainly used as a counter gas in the chamber. The incident particles pass through each of the conducting anode and cathode which are made of 4 μm thick aluminized mylar foil. Each of the anodes and the cathodes is tilted in 30° angle so that the liberated electrons and the positive ions drift away from the original particle trajectories in the opposite direction of each other. Then, they have little chance to collide with each other and recombine. Both the anode and the cathode foils are glued on aluminum rings. These glued foils are stretched tightly by applying the appropriate tension to avoid distortion due to the electrostatic force when high voltage is applied to the anodes. The signal of the detector from

the grounded anodes and the cathodes was measured using six peaks sensitive ADC. More detailed information of the above-mentioned MUSIC detector, including its working principle, can be found in reference [43].

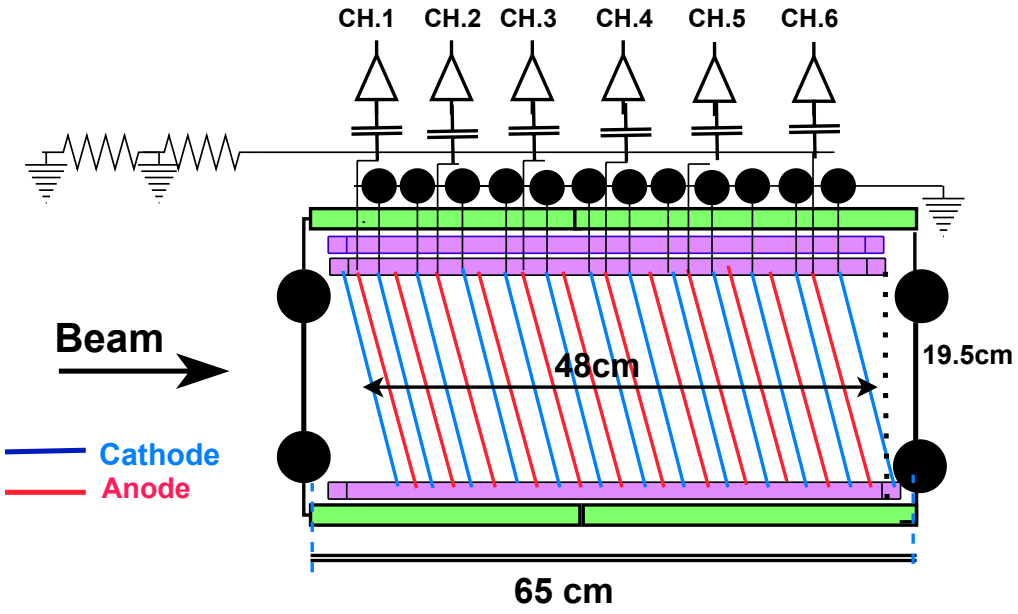

Figure 3.3. Schematic diagram of the MUSIC detector used at RIBF RIKEN for the measurement of the energy loss (ΔE). This figure is adapted from Ref. [43].

The principle of the ionization chamber is based on a collected charge which is proportional to the amount of energy loss at each strip. The incoming heavy ion beam penetrates the detector chamber and interacts with the electrons of the medium (foils, gas), and loses energy. In this process the gas gets ionized, electrons are removed from the foils, so the free electrons are generated, which are collected and induce a signal. Since the number of the created electrons is proportional to this energy loss, these electrons can be collected by using an electric field and used to determine the energy loss. The mechanism of energy loss of the ions per unit distance depends on the atomic number of particles and their velocity. The energy loss measures in the MUSIC detector at high velocities for the fragments with the atomic number Z can be associated with the Bethe-Bloch formula for the stopping power of the particles [9].

$$\left\langle \frac{-dE}{dX} \right\rangle = \frac{4\pi}{m_e c^2} \frac{nz^2}{\beta^2} \left(\frac{e^2}{4\pi\epsilon_0} \right)^2 \left[\ln \frac{2m_e c^2 \beta^2}{I(1-\beta^2)} - \beta^2 \right] \tag{3.1}$$

where, the $\beta = v/c$ for a particle with speed v, c is the speed of light and ϵ_0 the vacuum dielectric constant, energy E, traveling distance x, electron number density n and the mean excitation potential I, e and m_e the electron charge and the rest mass, respectively.

3.4.2 Plastic Scintillation Detectors

Two thin Plastic Scintillation Detectors were used in both BigRIPS and ZeroDegree spectrometer for the determination of Time of Flight (TOF). As mentioned earlier, plastic scintillation detectors are placed at F3 and F7 in BigRIPS while at F8 and F11 in the case of ZeroDegree

spectrometer. The thickness of each plastic was 0.2mm. The scintillators are build from a BC-420 scintillation material coupled to HAMAMATSU H1949 Photo Multipliers (PMTs) at both sides. When the ions traverse the plastic scintillator, the signal is produced and thus produced signal is collected by two photo-multipliers on each side of the detector. Each PMT gives one signal that is split into two analog signals to record the energy loss and the timing information of each hit. The charge-integrated signals from the PMT contain the position information of an incident particle [35]. It is expressed as follows:

$$q_1 = q_0\, exp\Big(-\frac{L+x}{\lambda}\Big) \text{ and } q_2 = q_0\, exp\left(-\frac{L-x}{\lambda}\right) \tag{3.2}$$

from this we can find:

$$x = -\frac{\lambda}{2}\ln\left(\frac{q_1}{q_2}\right). \tag{3.3}$$

where, q_0 is the signal value of the original scintillation. q_1 and q_2 are the signal values from the left and right of the PMTs and λ, the attenuation length of the light in the scintillation counter respectively. L and x are the length of the scintillator counter and horizontal position of an incident particle respectively. Also, the relationship between the timing signals from the PMTs and the position information of the incident particle is given by the relation:

$$x = -\frac{V}{2}\Big(t_2 - t_1\Big). \tag{3.4}$$

Here, V is the propagation of speed of light in the scintillation counter and t_1 and t_2, represent the timing information from left and right PMTs respectively. From equation (3.3) and (3.4) we get

$$-\frac{\lambda}{2}\ln\left(\frac{q_1}{q_2}\right) = -\frac{V}{2}\Big(t_2 - t_1\Big). \tag{3.5}$$

which allow us to remove inconsistent events. Similarly the time signal in each of the focal planes are given by:

$$T_{focalplane} = \frac{t_R + t_L}{2} \tag{3.6}$$

where t_L and t_R are the timing signals from the left and right PMTs, respectively. Summing the left and right times, the position dependence of the ion hit is estimated. The TOFs in BigRIPS and ZeroDegree are given by:

$$TOF_{BigRIPS} = T_{F7} - T_{F3} + offset_{37} \qquad TOF_{ZeroDegree} = T_{F11} - T_{F8} + offset_{811} \tag{3.7}$$

where the offset parameters are experimentally determined.

3.4.3 Parallel Plate Avalanche Counter (PPAC)

The position of the Parallel Plate Avalanche Counter (PPAC) in this experimental setup is shown in Table [3.1]. The PPAC detectors are used for tracking the trajectory of each ion and to define the beam profile. The beam passing the beamline is formed by high-energy projectile

fragmentation followed by an in-flight separation process. For precise measurement of position and angles of the particles along the beam line, a PPAC detector was used. Particle trajectory reconstruction at F3-F5 and F5-F7 was done for the measurement of the $B\rho$ value. For trajectory reconstruction, the positions and angles of fragments were measured at F3, F5, and F7 foci by a couple of PPAC detectors, installed at respective foci of the BigRIPS spectrometer. A similar process was followed in one stage at F8, F9 and F11 foci in the ZeroDegree spectrometer.

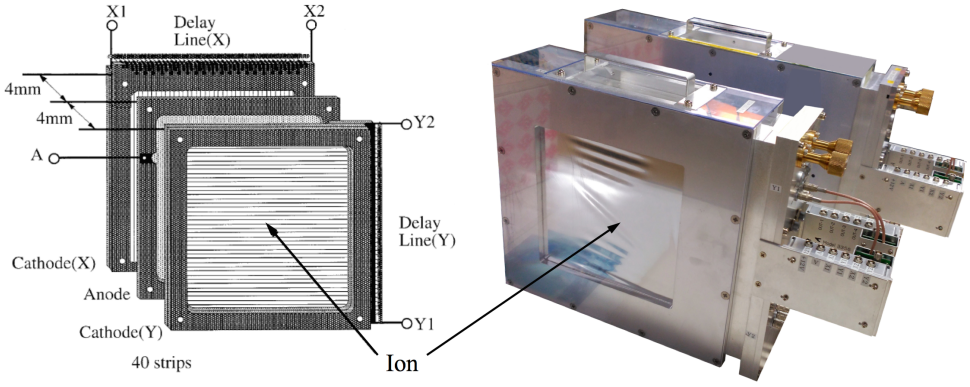

Figure 3.4. Image on the left shows the schematic view of PPAC whereas the image on the right is the photograph of two sets of double PPACs used in the experiment. Figures taken from Ref. [42, 44] respectively.

The two-fold $B\rho$ measurement at BigRIPS is essential to deduce the A/Q value in combination with the TOF measurement. The detail of the trajectory reconstruction is described in reference [35]. Figure [3.4] illustrates the schematic view of a delay-line PPAC. An anode plate is located in between two cathodes at a distance of 4 mm. Both the anode and the cathode are encapsulated in a chamber filled with a perfluoropropane C_3F_8 gas. The advantages of using this gas are a large energy deposition of the ion when passing through it, a fast rise time of the signal and it is not flammable. When an ion traverses the gas, it ionizes the gas molecules which induces an electron avalanche. Usage of double PPAC enables the measurement of the angle of the trajectory. Five signals, one from the anode and two from each side of the cathode planes are obtained from each PPAC, and thus obtained signals are used for the time and the charge information. The cathode signals are separated into up and down (and right and left) direction shown as Y1 and Y2 (and X1 and X2) in Figure [3.4] and the delay time is calculated with a time-to-digital converter (TDC). Numerically, position P_X and P_Y in the PPAC are given by the equation [44]:

$$P_X = K_x \frac{T_{x1} - T_{x2}}{2} + X_{off} \qquad P_Y = K_y \frac{T_{y1} - T_{y2}}{2} + Y_{off} \tag{3.8}$$

where K_x and K_y are the slope factors for the P_X and P_Y delay lines, T_{x1} and T_{x2} (T_{y1} T_{y2}) are the delay-times between the two signals in the X (Y) direction, and X_{off} and Y_{off} are the geometrical offsets. The sum of the delay times, $T_{sum\,x} = T_{x1} + T_{x2}$ and $T_{sum\,y} = T_{y1} + T_{y2}$, is a constant value and can be used to remove inconsistent events detected in the PPACs.

3.5 Detector for in-beam Gamma-ray Spectroscopy

In this experiment, the DALI2 γ-ray spectrometer is installed at the F8 focal point and surrounding the secondary target to detect γ-rays emitted from the decay of excited states in reaction products.

3.5.1 DALI2 Gamma Detector Array

A 186 NaI(Tl) detector array called DALI2 (Detection Array for Low Intensity radiation 2) has been constructed and implemented in RIKEN Nishana center for in-beam γ-ray spectroscopy experiments with fast RI beams [45]. Because of the special features like a good compromise between the intrinsic energy resolution, detection efficiency, and the cost, NaI(Tl) has been employed as the detector crystal. DALI2 is a 4π γ-ray detector array for the detection of the γ-rays emitted with the velocities around the range $\beta = 0.3 - 0.6$. DALI2 is composed of three types of detector crystals of different dimensions. The details of the manufacturer, numbers and the dimensions of the DALI2 crystals are shown in Table [3.2].

TABLE 3.2. The DALI2 scintillation crystals and their types used to build the array.

Manufacturer	Numbers of crystals	Dimentions(mm)	PMT Diameter(Φ)
Saint-Gobain	88	$45 \times 80 \times 160$	38
Scionix	66	$40 \times 80 \times 160$	38
Bicron	32	$60 \times 60 \times 120$	50

Each of these DALI2 crystals are encapsulated in a 1-mm thick aluminium housing coupled with the PMTs. The first two crystals in the table are coupled with 38 mmϕ HAMASTU R580 PMTs, whereas the last type use 50mm ϕ HAMASTU R1306 PMTs.

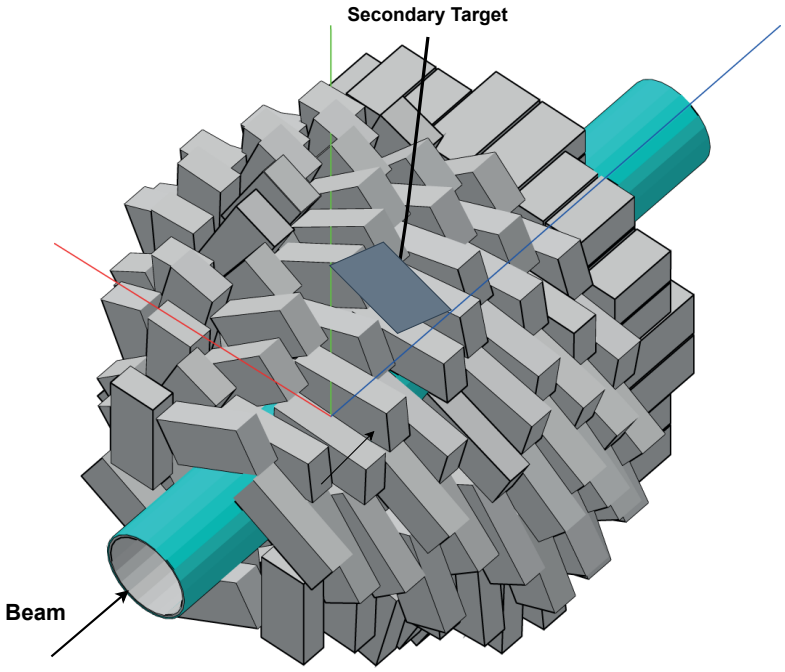

Figure 3.5. Schematic diagram of the DALI2 array configuration with a beam pipe and the crystals [46].

Figure [3.5] displays a schematic DALI2 view surrounding the beam pipe in the DALI2 crystal configuration. The entire setup of DALI2 crystals covers a polar angles in the laboratory frame between 20° and 150°. All 186 detectors are arranged in 12 layers, perpendicularly to the beam axis and the detector matrix covers the forward angles. Each of these crystals are supported in a fixed frame on a 5 mm thick aluminium plate and there are 6-14 detectors crystals on each layer. The first 11 layers consists of 122 detectors arranged in circles in the plane perpendicular to the beam axis. Because of this arrangement each of the detectors shortest edge will be parallel to the beam axis which minimize the opening angle. As shown in figure,

the detectors circles' radii increase with decreasing polar angle. Doppler broadening is worse near 90°, therefore you want small opening angles there. At forward and backward angles the Doppler shift is larger, but Doppler broadening is less, therefore you can have larger opening angles. At forward angles the gamma rays are boosted to higher energies, therefore is is better to have the wall configuration with the full length of the detectors to stop the gammas. Thereby, the opening angle Doppler broadening is approximately balanced for all γ-ray angles. The combination of 64 detectors in the twelfth layer forms a wall like configuration, where the crystals long edges are placed parallel to the beam axis. This configuration helps to achieve high addback efficiency for γ-ray scattering events across several crystals. The secondary target is fixed in the plane of the sixth layer of the detector. The layer downstream to the target are in backward angles ($\theta = 90^\circ - 150^\circ$) and layers upstream to the target are forward angles ($\theta = 20^\circ - 90^\circ$).

In addition to the intrinsic resolution of the detector, the resolution of the γ-transition energy is affected by the Doppler effect. Therefore, the high granularity of DALI2 is required to perform accurate Doppler correction. The details about Doppler shift correction is mentioned in Section 4.2.4. Furthermore, in case of in-beam spectroscopy, the relativistic velocity of the particles results a Lorentz boost towards forward angles and the coverage of the forward angles becomes important. At relativistic energies, the Lorentz boost plays a major role in increasing the detection efficiency and the energy resolution at forward angles. Moving the target position in one direction will improve the resolution of the detectors in the opposite direction and worsen the ones in the direction of move. The experimental conditions like beam velocities, target thickness, beam line directions also affect the energy resolution. The intrinsic energy resolution and the photopeak efficiency for the γ-ray emission were obtained for three standard sources, ^{60}Co, ^{88}Y and ^{137}Cs. At first, the expected efficiencies of the array were estimated using GEANT4 simulations and then the experimental condition was applied to calculate efficiency of experimental sources. γ-ray detected from more than one crystal can be regarded as scattering events from the same initial γ-ray for all nearby crystals. Therefore, the addback effect has to be considered. The calculated GEANT4 simulated efficiency shows that by using addback, the full energy peak efficiency value increases. The calculated experimental and simulated efficiency values (with and without addback) are shown in Table 4.5, Chapter 4.

3.6 Data Acquisition (DAQ) and Trigger Configuration

Data acquisition system at RIBF, so-called RIBF DAQ is used for the experiments involving BigRIPS and ZerooDegree spectrometers [47]. RIBF DAQ is designed to acquire events corresponding to a large number of RIBs produced by the fragmentation and fission reaction at the production target position at F0 focus. This system has functions of network-distributed data processing, hierarchical event building and parallel readout which are achieved with newly developed software and commodity hardware. All these functions are performed with commercial computers, network equipment standard VME and CAMAC modules. For all CAMAC and VME modules, a common trigger is required. In response to a common trigger, a front-end computer (FEC) reads data from the CAMAC and VME modules on an event-by-event basis. The logical OR of busy signals from each FEC with general logic modules allow sharing the system dead time to all FECs. This is necessary because, to produce a common trigger, the system dead time has to be shared by all the FECs, i.e. common dead time is required. The dead time of the system is determined by the slowest FEC. In our experiment, the slowest FEC corresponded to a beam-line detector.

The trigger condition for the Data Acquisition System is explained in this section. Applying

the trigger condition has several purposes, however in our experimental case, the trigger condition was used to a) achieve good events, b) reduce the large number of unwanted events hence dead time c) easily reduce the recorded data and handle the data storage and d) estimate number of beam particles hitting the Au target to create the reaction (Coulomb excitation). With the aim of selecting the events of interest, the trigger condition used during the experiment to initialize the data acquisition is explained below.

- **F7(DS) trigger**: As the main trigger, the F7 plastic signal was chosen. It is generated when the ion produces a signal in the F7 plastic detector. The signal was then split and passed through the rate divider to downscale (DS) which create a F7(DS) trigger condition. Thus created F7(DS) events were assigned as a projectile events and used to identify the number of particles arriving to the secondary target. The downscale factor is necessary to improve the data collection by reducing the dead time of the DAQ. The downscale factor used in the experiment was 20.
- **F7(DS)×F11 trigger**: In addition to the F7 plastic detector the ion also produce signal in the F11 plastic detector. The F7(DS) trigger was put in coincidence with F11 trigger to generate F7DS×F11 trigger which symbolize the ions reached at the end of ZeroDegree spectrometer.
- **F7× F11×DALI2 trigger**: Together with F7 and F11 signal, at least one γ-ray signal is detected from the DALI2. The trigger events from the DALI2 corresponded to at least one NaI crystal hit and the PPACs were not part of any triggers. The signals generated from the DALI2 were recorded for each event. The F7×F11 signal was put in coincidence with the γ trigger from the DALI2 which creates F7× F11×DALI2 γ trigger. This trigger is needed to select the Coulomb excitation events.
- **F7(DS)× F11×DALI2 trigger**: This trigger is same as before but with F7 plastic signal down scaled. This trigger is just a subset of trigger 6 as shown in Figure [3.7].

The above mentioned trigger configuration is systematically shown in Figure [3.6]. The scaling factor of 20 was applied by the rate divider module in the experiment. Also, Figure [3.7] displays the total number of events at different trigger conditions in the experiment.

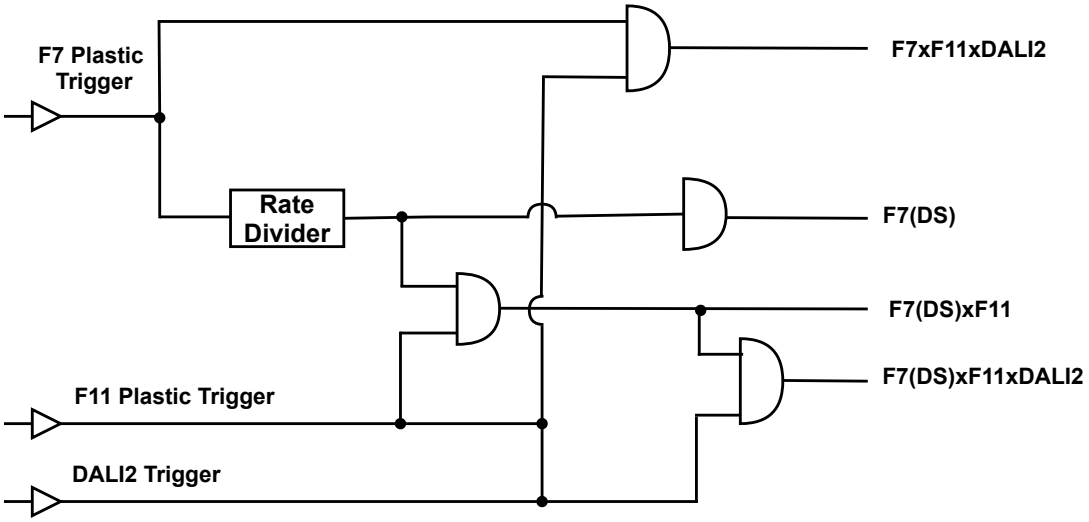

Figure 3.6. The schematics of the trigger configuration used during the experiment. During the experiment, the scaling factor of 20 was employed by the rate divider module. Figure adapted from Ref. [42].

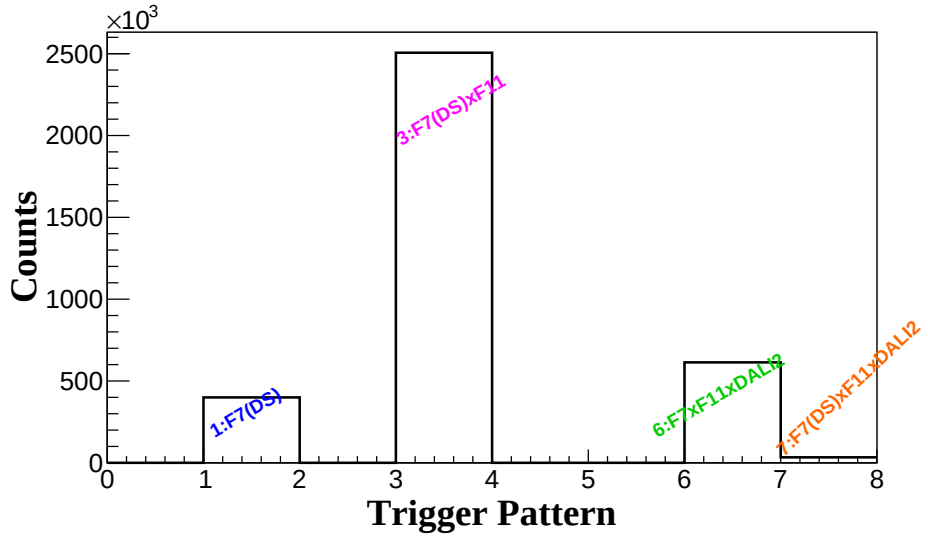

Figure 3.7. The DAQ was triggered when one of four conditions was met, labeled trigger 1, 3, 6, and 7, and that the figure shows the number of events that met the different trigger conditions.

3.7 GEANT4 Simulations

The GEANT4 simulation package for the DALI2 detector was developed by Pieter Doornenbal and the main aim of the simulation code is to produce well-grounded values for the $\gamma - ray$ energy resolution and the detection efficiency under realistic experimental conditions for secondary beams. The GEANT4 simulation code for γ-ray detectors used in the RIKEN-RIBF Facility includes the geometry of the DALI2 crystals, the beam pipe, absorbers, and the target holder. The beam profile was modeled in a way that produces the experimental energy and the angular emittance. The simulated data can be analyzed the same way as the in-beam data, as Doppler correction is performed in the simulation as well. The response function of the DALI2 obtained with the GEANT4 is used to fit the Doppler-corrected γ-ray spectra of ^{77,79}Zn isotopes and to extract the gamma intensity of each transition. Therefore, it is very crucial to verify that the simulated results should be in very good agreement with the experimental measurement. The comparison between the experimental and the simulated spectra for different sources is presented in chapter 4, "Data Analysis" and a good agreement between the experimental and simulated spectra is observed. The details of the performed simulations can be found in the Simulation manual [48]. The simulation package is divided into three steps: the EventGenerator, the EventBuilder, and the Reconstructor.

EventGenerator

The EventGenerator is the first step of simulation where the heavy ion beam strikes on a target and emits γ rays. The incoming and outgoing beams may be different, i.e. knock-out reactions are covered in the simulation. The input of the EventGenerator like the type of the projectile P with mass A_p, the element number Z_p and the charge state Q_p of the isotope are defined. The beam energy before striking the target E_p, the position of the projectile before impinging the target, beam angle (θ_p), the types of target, for example, Au, Be, C, Fe etc, and the Borrel (the velocity shift for the fragmentation process) are also defined properly in this step.

EventBuilder

The EventBuilder simulates the γ-ray detection responses and uses the EventGenerator as input values. In addition to the input values from the EventGenerator, EventBuilder defines the specific inputs like DALI2INCLUDE in which the detector array determines the position and rotation relative to the target, ZPOSSHIFT f which specifies how many cm the detectors are shifted relative to the target. In addition, the geometry of the DALI2 as a plain text file, the resolution of each individual detectors, thresholds, and absorbing materials such as housing, shielding and beam pipe are defined in this step of simulation. The energy resolution of the detectors is the experimentally measured intrinsic resolution of each crystal. Including all the information from the EventGenerator, the detection of the emitted γ-rays is simulated.

Reconstructor

The Reconstructor is the final step of the simulation which performs the Doppler correction of the simulated γ-rays including addback procedures. It follows the same procedure as for the experimental data. The addback distance of 15 cm is applied in between any two detectors for addback reconstruction. Similarly, the TRIGGER condition and the FIFIND are also defined which gives the trigger probability as a function of γ-ray energy, and the average first interaction point of a full energy peak γ-ray respectively.

Note: All the parameters of the EventGenerator, EventBuilder and the Reconstructor are explained in detail in Appendix B.

3.8 Performed Experiments and the Run Conditions

The experiment took place in April 2015 and lasted for four days employing different BigRIPS and ZeroDegree settings. The main aim of the experiment was Coulomb excitation of ^{77}Cu. The separation and identification of particles were performed at BigRIPS then thus identified particles were delivered in-flight at relativistic energies and bombarded onto the secondary target. Two different reaction targets were used in order to scatter these isotopes. The primary target was Be to produce in-flight fission of ^{238}U. For the secondary target, two different materials were used: ^{197}Au and ^{12}C. The Au induces mostly electromagnetic excitation, but also a little bit of nuclear excitation. To estimate the amount of nuclear excitation, we use the data on C, where Coulomb excitation is negligible. The details of the experimental run and conditions are shown in Table [3.3].

TABLE 3.3. The summary of the experimental setup with ^{197}Au ($948 mg/cm^2$)) and ^{12}C ($903 mg/cm^2$) target settings.

Primary Beam	^{238}U	^{238}U
Primary Intensity (pnA)	15	15
Beam Energy (MeV/u)	345	345
Production Target and its Thickness	^{9}Be 3mm	^{9}Be 3mm
Bρ_{01} (T.m)	7.700000	7.700000
Degrader at F1 and its Thickness	Al 8mm	Al 8mm
F1 slits (left/right mm)	5/80	5/80
B$\rho_{12,23}$ (T.m)	6.832500	6.832500
F2 slits (left/right mm)	7/7	7/7
B$\rho_{34,45}$ (T.m)	6.817000	6.817000
B$\rho_{56,67}$ (T.m)	5.347900	6.817000
Degrader at F5 and its Thickness	Al 10mm	Al 10mm
F5 slits (left/right mm)	120/120	120/120
Bρ_{78} (T.m)	5.151100	5.347900
F7 slits (left/right mm)	7/7	7/7
Reaction Target	^{197}Au ($948\ mg/cm^2$)	^{12}C ($903\ mg/cm^2$)
F7DS factor	1/20	1/20
Bρ_{89} (T.m)	4.7911	5.347900
Bρ_{910} (T.m)	4.788500	4.447500
F9 slits (left/right in mm)	120/120	120/120
Bρ_{1011} (T.m)	4.788500	4.443000
F10 slits (left/right in mm)	120/120	120/120

Chapter 4

Data Analysis

"The whole of science is nothing more than a refinement of everyday thinking."

-ALBERT EINSTEIN

This chapter intends to analyze the experimentally obtained data to get the experimental quantities of interest. The experiments performed at RIKEN consisted of BigRIPS reaction target surrounded by DALI2 and ZeroDegree spectrometer, the data analysis is therefore divided into two parts:

Part I: Particle Identification in BigRIPS and ZeroDegree

Part II: The DALI2 γ-ray spectrometer

However, the first part related to the particle identification of the reaction fragments through the BigRIPS and ZeroDegree spectrometers has been done prior to the present thesis work. The data was already pre-sorted into root files, and the extracted information on Z and A/Q is being used for further analysis. Therefore, the Data analysis section here will cover the analysis of the second part, related to the DALI2 γ-ray spectrometer. Before going to the steps of the data analysis of DALI2, particle identification in BigRIPS and ZeroDegree will be briefly explained below.

4.1 Particle Identification

The particle identification for both the BigRIPS and the ZeroDegree was performed with the moment loss achromat method ($TOF - B\rho - \Delta E$). In $TOF - B\rho - \Delta E$ method, we deduce the Z and $\frac{A}{Q}$ values from the measured TOF, Bρ, and ΔE using equations as follows:

$$TOF = \frac{L}{\beta c} \tag{4.1}$$

$$\frac{A}{Q} = \frac{B\rho}{\beta\gamma}\frac{c}{m_u} \tag{4.2}$$

$$\frac{dE}{dX} = \frac{4\pi e^4 Z^2}{m_e v^2} Nz[\ln \frac{2m_e v^2}{I} - \ln(1-\beta^2) - \beta^2] \tag{4.3}$$

Here L is the flight path length, v is the velocity of particle, defined as $\beta = \frac{V}{C}$, $\gamma = \frac{1}{\sqrt{1-\beta^2}}$: c is the velocity of light , m_u= 931.494 MeV is the atomic mass unit, m_e is the electron mass, and e is the elementary charge. z, N and I represent the atomic number, atomic density and mean excitation potential of the material, respectively. Z, A and Q represent the atomic number, mass and charge respectively. The dE/dX formula in equation [4.3] describe the energy loss ΔE. The details of the above-described particle identification method can be found in Ref. [35].

4.1.1 Particle identification in BigRIPS

The particle identification in BigRIPS spectrometer starts at the F3 focal plane and ends at the F7 focal plane. Fig. [3.2] shows the schematic diagram of the BigRIPS with the setup of beamline detectors used for particle identification. The TOF is measured with two plastic scintillation counters installed at F3 and F7, with a central flight-path length of 46.6m. The $B\rho$ values are obtained from position measurement from double PPAC detector configurations. Energy loss, necessary to deduce the Z of the ion, was measured in the MUSIC placed at the F7 focal plane. Applying above equations [4.1-4.2] to the measurements made in the the BigRIPS spectrometer, we have the following relation:

$$TOF = \frac{L_{35}}{\beta_{35} c} + \frac{L_{57}}{\beta_{57} c} \tag{4.4}$$

$$\frac{A_{35}}{Q35} = \frac{B\rho_{35}}{\beta_{35}\gamma_{35}} \frac{c}{m_u} \tag{4.5}$$

$$\frac{A_{57}}{Q57} = \frac{B\rho_{57}}{\beta_{57}\gamma_{57}} \frac{c}{m_u} \tag{4.6}$$

Here the subscripts 35 and 57 indicate the quantities related to the F3–F5 and F5–F7 sections, respectively. If the $\frac{A}{Q}$ value does not change at F5, then

$$\frac{\beta_{35}\gamma_{35}}{\beta_{57}\gamma_{57}} = \frac{B\rho_{35}}{B\rho_{57}} \tag{4.7}$$

In this case the fragment velocities before (β35) and after (β57) can be deduced from Eqn [4.4] and Eqn [4.7] using the measured TOF, $B\rho$, ΔE, Bρ35 and Bρ57 values, allowing the determination of absolute $\frac{A}{Q}$ value. The mean velocity can be considered as the velocity of particles at BigRIPS. The absolute Z value is derived using the measured ΔE and β57values based on Eqn [4.3].

4.1.2 Particle identification in ZeroDegree

The particle identification in ZeroDegree spectrometer was performed with same above mention procedures followed in ZeroDegree. However, the PID process in ZeroDegree begins from F8 till F11 focal point. Figure [4.1] shows the schematic of ZeroDegree where we cannot see any energy degrader. As mentioned earlier the same equation of TOF-$B\rho$-ΔE method is applicable in the case of a ZeroDegree spectrometer for obtaining Z vs. A/Q plot. Similar to the BigRIPS path, TOF and the positions of the reaction products after the target is determined from the plastic scintillators (installed at F8 and F11) and PPAC (installed at F8, F9 and F11) detectors, while the energy loss is measured using the MUSIC detector at F11.

$$TOF = \frac{L_{811}}{\beta_{811} c} \tag{4.8}$$

$$\frac{A}{Q} = \frac{B\rho_{911}}{\beta_{811}\gamma_{811}} \frac{c}{m_u} \tag{4.9}$$

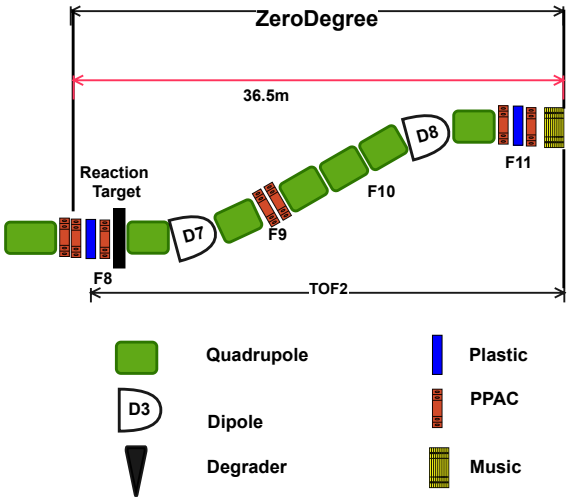

Figure 4.1. Schematic diagram of ZeroDegree spectrometers.

In the case of ZeroDegree, the TOF is the measure between two plastic scintillation detectors installed between F8 and F11 with a distance of 36.5m. The magnetic rigidity is measured with the help of PPAC detectors installed in F9 and F11. Also, the MUSIC detector installed at F11 is used to measure the energy loss. The respective equations [4.3, 4.8 and 4.9] are used (as mentioned in case of BigRIPS) to calculate A/Q with help of determined value of TOF, $B\rho$ and ΔE.

A two-dimensional plot of Z versus $\frac{A}{Q}$ is used for the particle identification in BigRIPS and ZeroDegree spectrometer. Figure [4.2] shows the PID plots with Au as the reaction target (secondary target). Figure [4.2(a)] is the PID plot before the reaction target whereas Figure [4.2(b)] is the PID plot after the reaction target. The identified Zn particles are encircled with red color. Remember that, the reaction target is located in between BigRIPS and ZeroDegree spectrometer. So, PID before reaction target indicates PID in BigRIPS and after target means PID in ZeroDegree spectrometer. Similarly, Figure [4.3(a) and (b)] shows the PID plots before and after the reaction target. The reaction target used in this case is C and the identified Zn particles are encircled with black color.

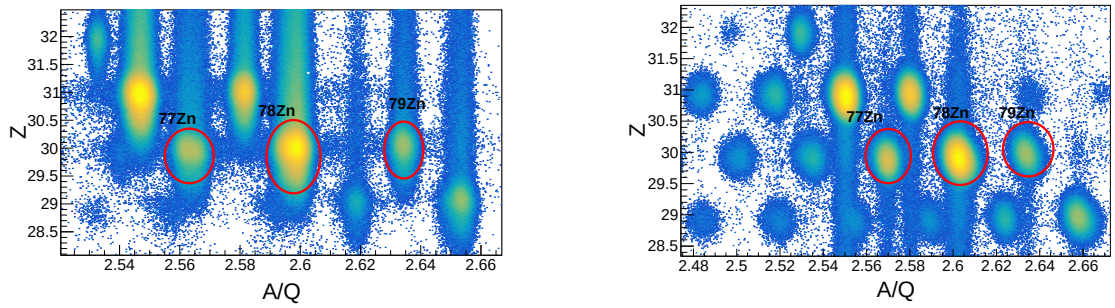

(a) PID before the Au target

(b) PID after the Au target

Figure 4.2. A 2D plot for particle identification for Au as as reaction target. The identified Zinc isotopes are shown inside the red circles with their respective names.

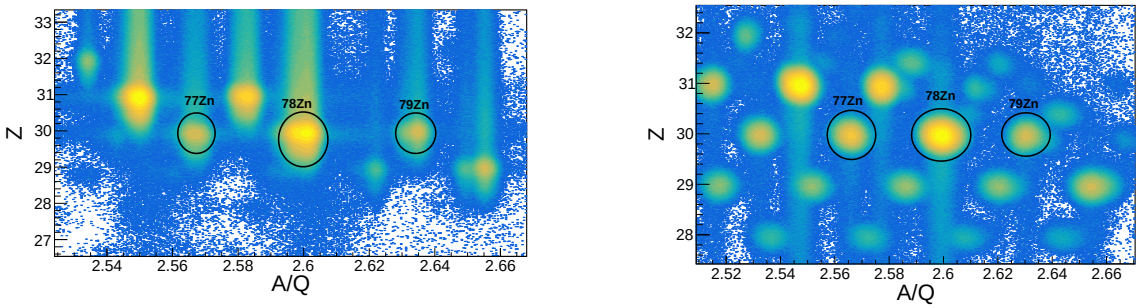

(a) PID before the C target

(b) PID after the C target

Figure 4.3. A 2D plot for particle identification with C as a reaction target. The respective identified Zinc isotopes are shown inside the black circle.

4.2 The DALI2 gamma-ray Spectrometer

4.2.1 DALI2 Energy calibration

The energy calibration for the detectors was performed using several γ-ray sources with different energies which cover the range of interest within these experiments. The DALI2 energy calibration runs were performed in three runs; beginning of the experiment, during the experiment and end of the experiment. The calibration was performed with three different γ-ray sources:

- ^{60}Co with 2 γ-ray energies 1173.23 keV and 1332.49 keV,
- ^{88}Y with 2 γ-ray energies 898 .04 keV and 1836.07 keV, and
- ^{137}Cs with a γ-ray energy 661.66 keV.

Each of these sources were placed inside the 4π DALI2 array, on the beam-pipe, close to the detectors to collect enough statistics for the calibration measurements. The data calibration for each source was accumulated for about 30 minutes. The ADC input has 4096 channels which corresponds energies up to $\approx$ 12 MeV and the energy calibration was done by converting the ADC signal to known source energies. For each NaI DALI2 crystal, the five source energy transitions were fitted with a Gaussian function to determine the centriod of the photopeak and with an exponential function to describe the background underneath the peak. Figure

[4.4] shows a 2D plot of calibrated energy versus the detector ID for three different source. It is clearly visible that, the detector number 97, 98 and 168 did not produce signal and was inoperable during the entire experiment. Similarly, detector number 127, 128 and 142 have worse energy resolution and were removed from the analysis.

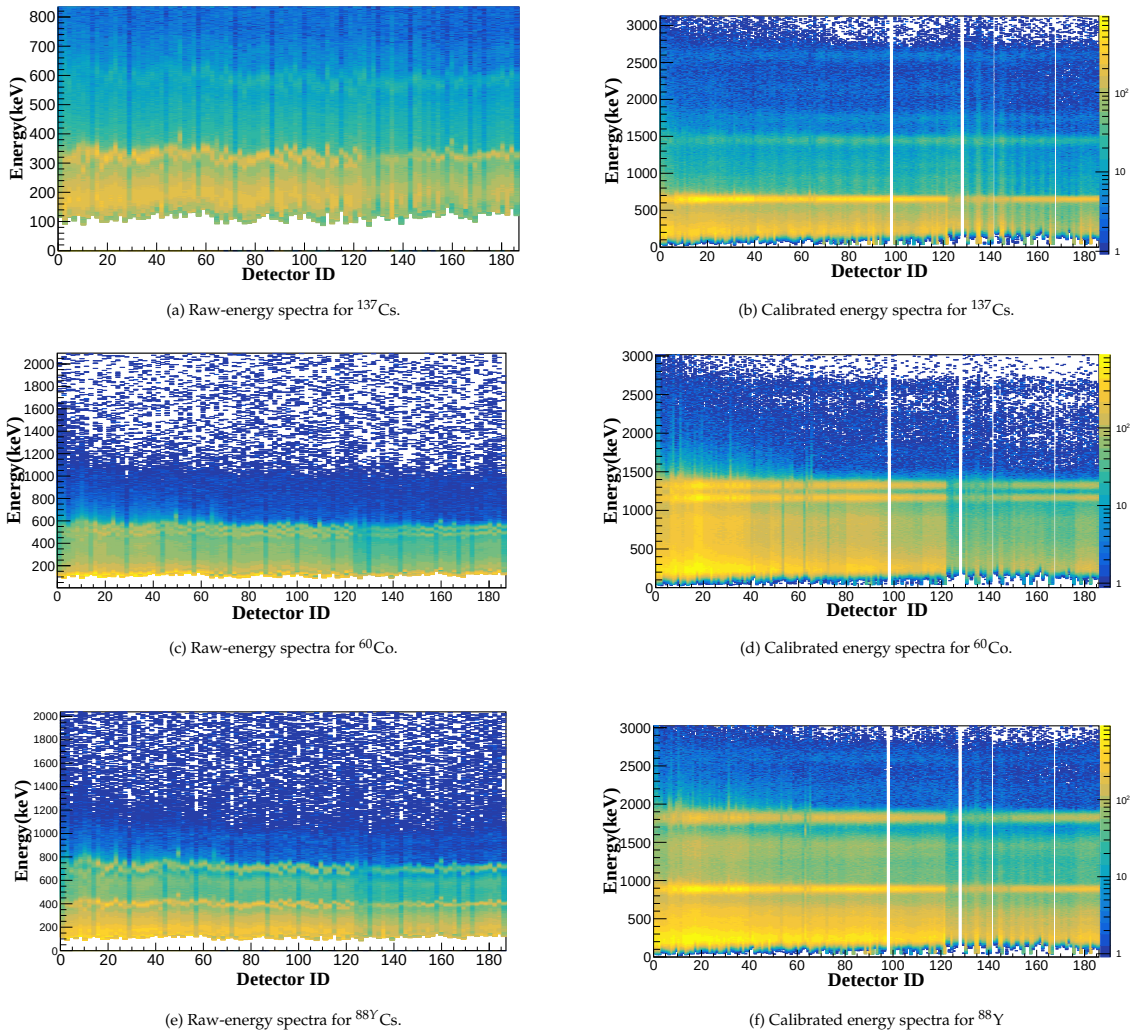

(a) Raw-energy spectra for ^{137}Cs.

(b) Calibrated energy spectra for ^{137}Cs.

(c) Raw-energy spectra for ^{60}Co.

(d) Calibrated energy spectra for ^{60}Co.

(e) Raw-energy spectra for ^{88Y}Cs.

(f) Calibrated energy spectra for ^{88}Y

Figure 4.4. Calibrated energy spectra for three different energy source used in the experiment. The 6 detectors with detector ID 97, 98, 168, 127, 128 and 142 had poor quality and were removed.

4.2.2 DALI2 Time Alignment

The time signal starts when the plastic scintillation detector in F7 generates a signal due to ion passing through it and ends when the DALI2 crystal detects a γ-ray. Each of the DALI crystal has an individual time signal and all the time signals were aligned to obtain a unique time distribution. In order to reduce background events in the γ-ray spectra, lower and upper limits of the time distributions was necessary to determine. This was done using the γ-ray transition from the first excited 2^+ state in ^{78}Zn. The γ-peak at 730 keV of ^{78}Zn at different time window was fitted to calculate number of gammas under the peak and hence the peak-to-total ratio. ^{78}Zn is best suited for this task because the spectrum has only one transition and rather well populated. The fitted plots are shown in Figure [4.5]. The green peak is the signal function, the blue dotted line is the background function and the red line in the histogram is the sum

of the signal function and the background function. The calculated peak-to-total ratio values are listed in Table [4.1]. Looking at these values, there is a very small change in peak-to-total ratios for different offseted parameters. However, it is very easy to decide to choose -13 to 5 as a optimum parameter as we can see the the ratio is maximum and we can assume that all the events will be included with in this time range.

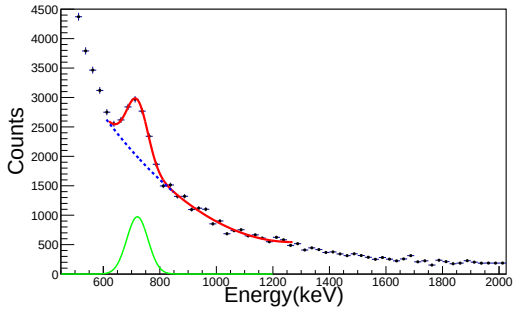

(a) The TimeOffseted plots with offseted parameters -13 to 0.

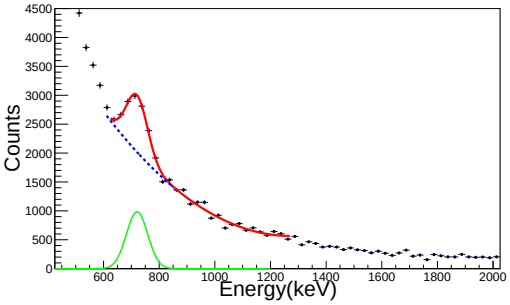

(b) The TimeOffseted plots with offseted parameters -13 to 1

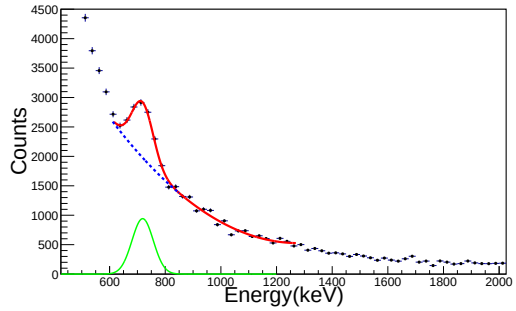

(c) The TimeOffseted plots with offseted parameters -13 to 2

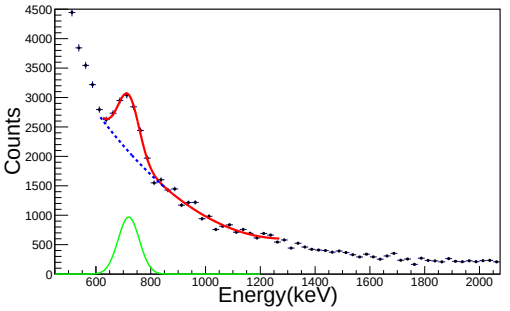

(d) The TimeOffseted plots with offseted parameters -13 to 3

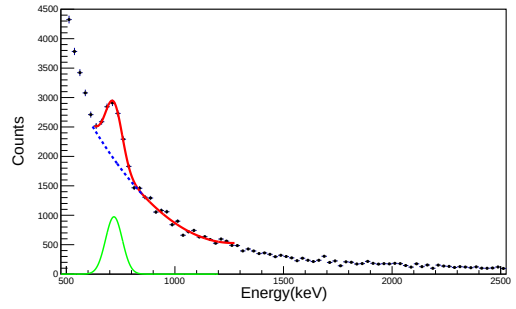

(e) The TimeOffseted plots with offseted parameters -13 to 4

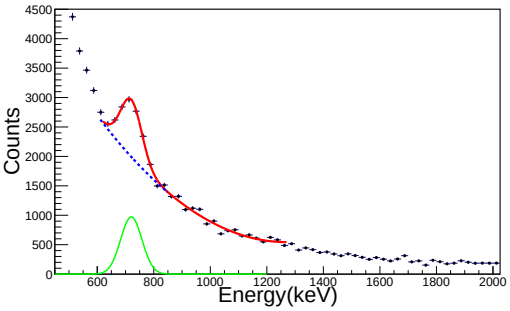

(f) The TimeOffseted plots with offseted parameters -13 to 5

Figure 4.5. The TimeOffseted plots with offseted parameters -13 to 0,1,2,3,4,5 respectively. The green peak is the signal function, the read line in the histogram is the sum of the background and the signal function whereas the blue dotted line is the background function fitted with the experimental data in between the energy range 660 keV and 800 keV for ^{78}Zn

TABLE 4.1. The calculated peak-to-total ratios for different time-offseted parameters for ^{78}Zn.

Time-window [ns]	Total number of counts under peak	Peak-to-total Ratio
-13 to 0	19042	0.0158
-13 to 1	19854	0.0165
-13 to 2	20499	0.0170
-13 to 3	21779	0.0181
-13 to 4	22212	0.0184
-13 to 5	22814	0.0189

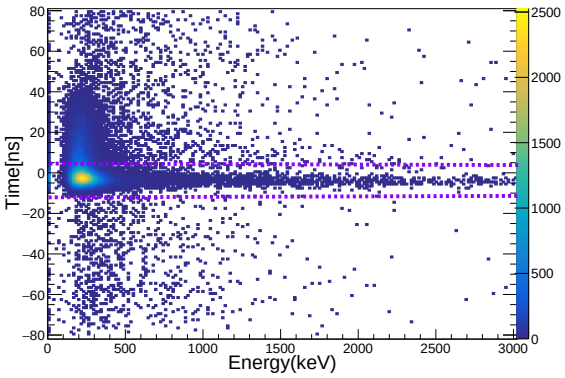

(a) Time-Energy correlation, showing the selected and rejected events for ^{77}Zn.

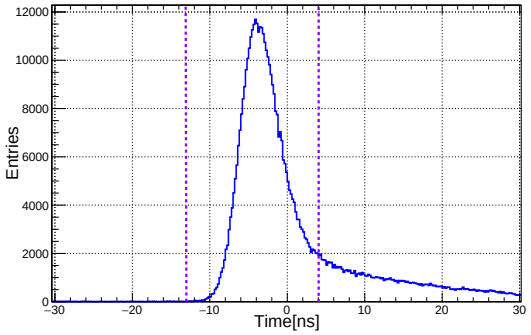

(b) Raw time spectrum for ^{77}Zn. The vertical bars shows the cutoff in between the parameter of -13 and 4 to remove the uncorrelated the background.

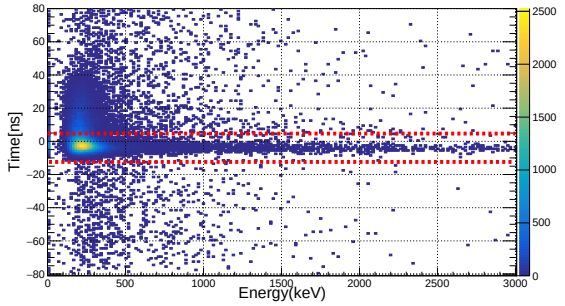

(c) Time-Energy correlation, showing the selected and rejected events for ^{79}Zn.

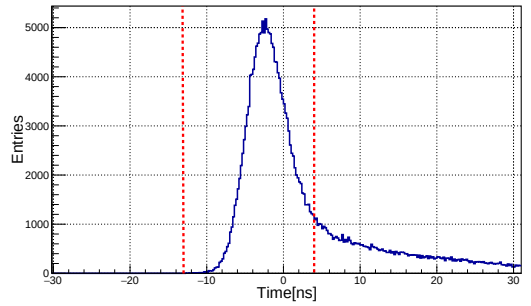

(d) Raw time spectrum for ^{79}Zn. The vertical bars shows the cutoff in between the parameter of -13 and 4 to remove the uncorrelated the background.

Figure 4.6. Time-Energy correlation showing selected and rejected events for respective isotopes in figure (a), (c) and the time projection of the selected time window for DALI2 in figure (b) and (d).

Once we confirm the offset parameter for time window, we can set the time cut on the time signal of the full array versus the energy of the γ-ray. It is applied on the time signal plot of both ^{77,79}Zn to reject uncorrelated events. Figure [4.6] shows the chosen time window that is considered for the analysis for both ^{77,79}Zn. On the right side of the distribution, a considerable amount of delayed events can be seen that are produced mainly by the charged particles hitting the crystals with low energy background events on both sides.

4.2.3 Addback

In an ideal γ-ray spectrometer the response function of the the detected γ-ray should consist of only the photopeak. However, the photopeak is associated by a continuum of Compton scattered events. In a Compton scattering event the γ-ray will deposit some of its energy in a DALI2 crystal before scattering and depositing its remaining energy in another DALI2 crystal. To recover the full γ-ray energy an addback routine is applied in the analysis which combines the energy in these related scattering events. The main idea of the addback algorithm is: if two or more energy depositions are registered in neighboring detectors, the energy in each of the adjacent detectors are summed to recover the full energy γ-ray i.e. E_γ = E1 + E2 + E3 +... . However, it is of course also possible that the scattered gamma ray escapes the detectors altogether. In that case it is not possible to recover the full energy. To determine in which events the addback routine is applied on we exercise an upper limit on the distance between the mean interaction point of γ-rays . A maximum distance of 15 cm is used in the analysis. The mean interaction points of each DALI2 crystal was determined using the GEANT4 simulation of DALI2. To obtain the optimum value of the maximum distance in the addback algorithm,

we used GEANT4 simulations. Figure [4.7] displays the photopeak response of DALI2 for a γ-ray at 730 keV for ^{78}Zn when different addback distances are used in the reconstruction of the energy. The addback distance 0 cm means no addback is applied. The addback distance 5 cm is equivalent to distance within the same detector so it is not necessary to include addback distance 5cm. With the increase in addback distance the intensity of the photopeak increases up to certain point but with further increase in addback distance, there will be a point where the intensity of the photopeak does not increase. As it is evident from the figure [4.7], beyond the addback distance of 15 cm we do not gain more in photopeak and, therefore, 15 cm was the addback distance used in the analysis and GEANT4 simulations when the addback algorithm was applied.

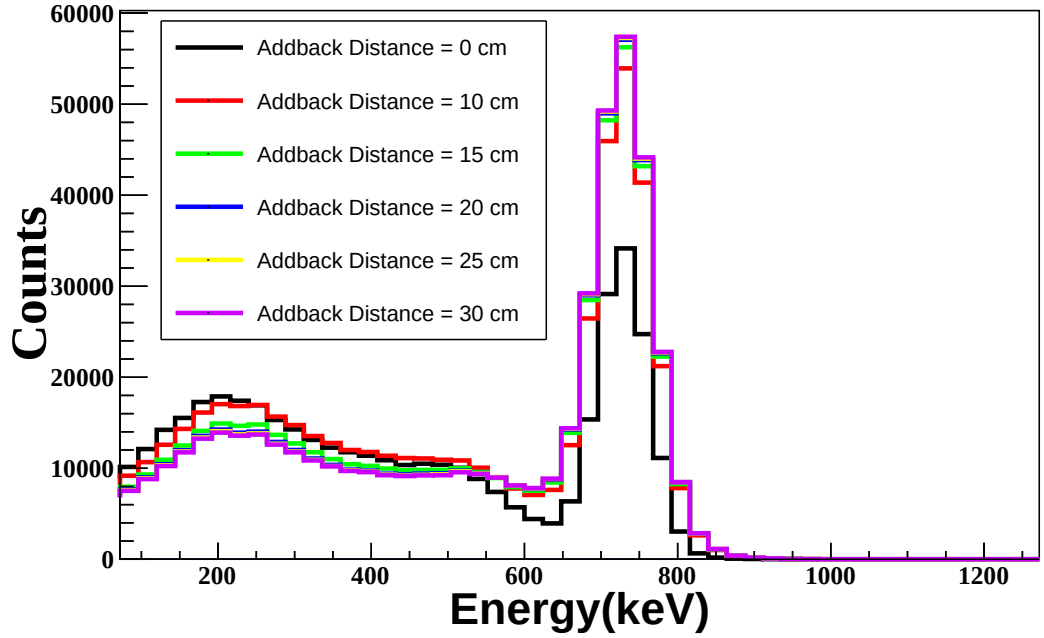

Figure 4.7. Effect of the addback procedure when different addback distances are used in the reconstruction of 730 keV energy of ^{78}Zn. The maximum gain in peak intensity is seen at a addback distance of 15 cm and beyond that we see a very less gain.

The output of the simulation is the addback table for each DALI2 crystal listing the crystals within the maximum addback distance. Figure [4.8] shows the enhancement in the peak-to-total ratio on the experimental γ ray spectrum measured with three different sources ^{137}Cs, ^{60}Co, and ^{88}Y with (red histogram) and without (blue histogram) addback. The radioactive beam experiments suffer greatly from background events and to increase the peak-to-total ratios of reaction γ-rays, addback should be considered. As shown in Figure [4.7] no background is assumed (other than Compton). However, in reality there is background from other sources as well and increasing the "addback radius" will make a spectrum a lot worse and actually remove good events from full-energy peak. (This effect is not included in the GEANT4 simulation). Also, the reconstruction of the addback has greater effect for the transition at higher energy for ^{60}Co and ^{88}Y and the effect is visible in the experimental spectrum while the Compton scattering is less for the 667 keV peak of ^{137}Cs.

Figure [4.9] shows experimental and GEANT4 simulated γ-spectrum of ^{78}Zn with and without addback. The red line in the histogram is with addback while the blue one is without addback. From the two different figures, we can see the gain we have in the simulated peak is much higher than the gain in the experimental peak. This might be because of large atomic background in the experimental spectrum while we do not consider the background in the

simulation. Because of the uncertainty in the addback procedure related to the large atomic background, addback was not applied in the further analysis of the ^{77,79}Zn data.

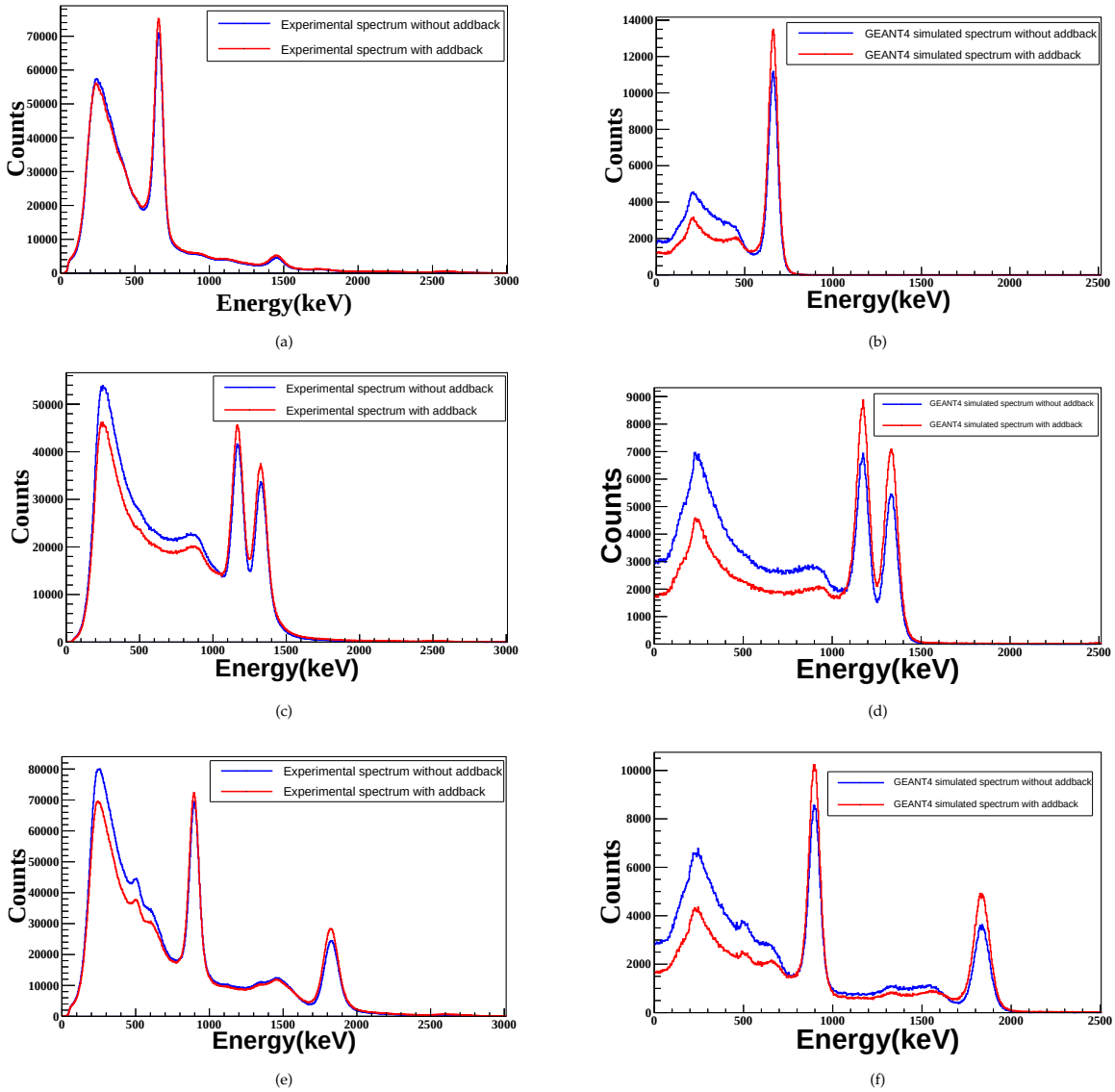

Figure 4.8. The enhancement in the peak-to-total ratio after applying a addback(distance of 15cm) between the (a,c,e) experimental γ ray spectrum and (b,d,f) GEANT4 simulated γ-ray spectrum measured with ^{137}Cs, ^{60}Co, and ^{88}Y sources respectively. The red histogram is measured with addback whereas the blue is measured without addback.

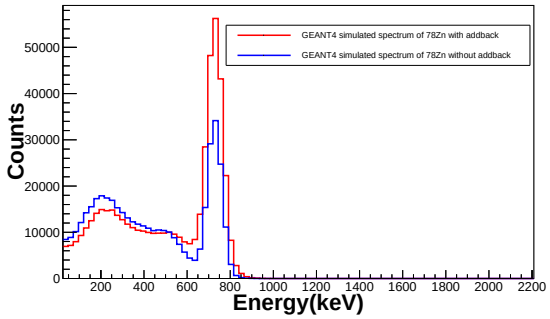

(a) GEANT4 simulated γ-ray spectrum of ^{78}Zn with and without addback.

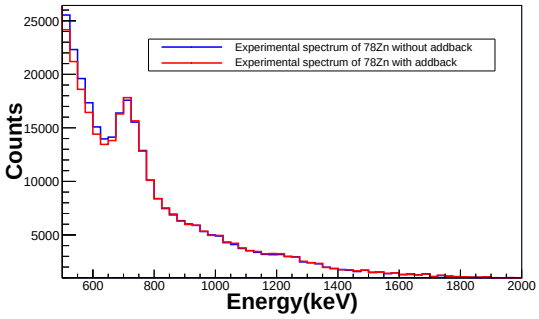

(b) Experimental γ-ray spectrum of ^{78}Zn with and without addback.

Figure 4.9. The GEANT4 simulated (left) and the experimental (right) γ-ray spectra of ^{78}Zn with and without addback. The gain in the photopeak intensity is much higher in GEANT4 simulated spectra when considering addback while the effect of addback is much less in case of experimental spectra. Note that the simulation considers only Compton background.

4.2.4 Doppler Correction

The Doppler effect is the change in frequency (wavelength) of the γ-ray emitted from a moving particle in relation to a constant particle detector. The high velocity ions ($\beta \approx 0.5$) are subjected to Doppler shift in relation to the fixed particle detector (DALI2) in our case. The relation between the energy in the laboratory system of $\gamma-$rays emitted from fast-moving ions, E_{lab} , and its energy in the center of mass, E_{CM} , is given by the relation:

$$E_{CM} = \gamma(1 - \beta cos\theta_{lab})E_{lab} \tag{4.10}$$

Where,

- θ_{lab} = The γ- ray emission angle with respect to the direction of ion (^{77,79}Zn).
- β = the velocity of the ion (^{77,79}Zn) at the moment of emission.
- E_{cm}= γ energy value when the ion moves with β velocity (center of mass).
- E_{lab} = γ energy value when ion is at rest

The angle between the ion direction and the direction of emitted γ rays (θ) can be determined via position of the DALI crystals. It is obtained by GEANT4 simulations to determine the mean interaction point of each detector in which the γ ray is detected. Figure [4.10] shows the the typical result of the Doppler shift correction on γ-ray energy spectrum measured by DALI2 for the Coulomb excitation on the Au target. The γ-ray peak at 730 keV with Doppler shift correction (red histogram) corresponds to the transition from the 2^+ state to the 0^+ ground state in ^{78}Zn. However, the spectrum at the laboratory system (blue histogram) does not show any peak.

The velocity of the ion at the moment of emission (β velocity) was experimentally measured, which corresponds to the velocity of the ions after the F5 degrader in case of BigRIPS (β_{BR}) spectrometer. Similarly, the measure β velocity for ZeroDegree (β_{ZD}) spectrometer corresponds to the velocity after F10 PPAC. Between F5 degrader and the target there are several layers of materials (dipoles and quadrupoles magnets, degraders, detectors etc.) which causes the β value to change until the ions reach the reaction target. The same phenomenon happens in ZeroDegree between F9 and F11 focal point. For Doppler correction, it is important to know the β values before, after and in middle of the reaction target. To calculate the velocities before,

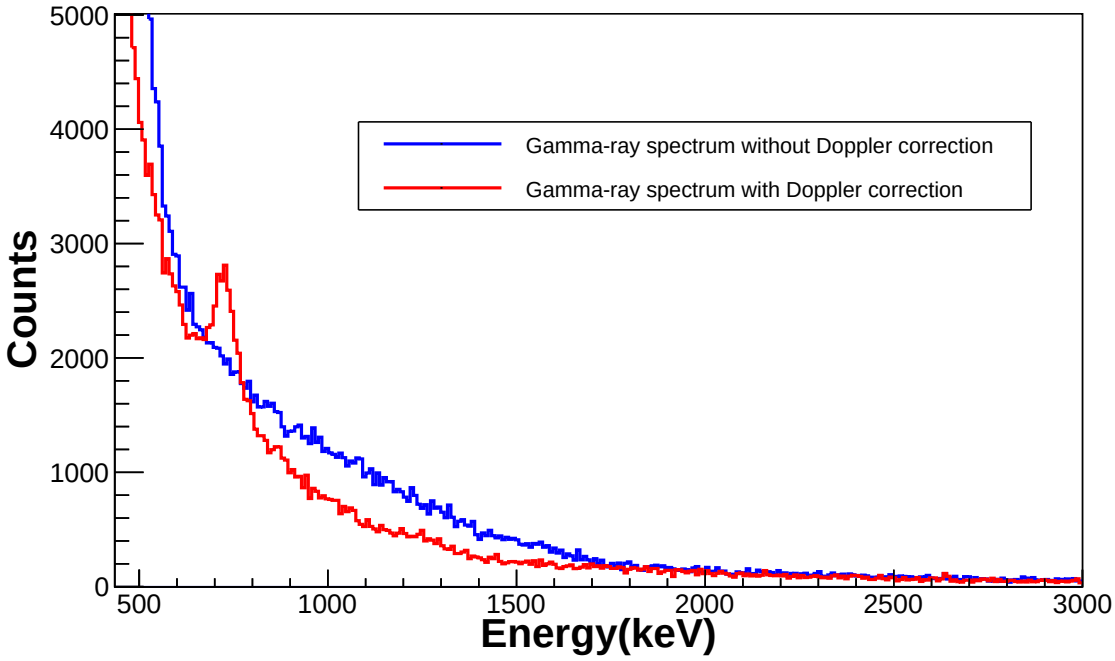

Figure 4.10. γ-ray energy spectrum obtained from the Coulomb excitation of ^{78}Zn on Au target with Doppler correction (red histogram) and without Doppler shift correction (blue histogram).

after and in middle of the target, we use LISE^{++} simulation [49]. LISE^{++} simulates the real experimental setup and the conditions for BigRIPS and ZeroDegree. All the optical elements (dipoles and quadrupoles magnets), detector materials, target materials, and the degrader materials used in BigRIPS and ZeroDegree are included in the LISE^{++} with the exact thickness and order. We inserted the $B\rho$-value for the D1 to D8 dipole magnets, the Al-degrader thickness (degrader-1 of 8 mm and degrader-2 of 10 mm), the beam value (^{238}U of 345 MeV/nucleon), primary target thickness target (^{9}Be of 3 mm), and the secondary target thickness (^{197}Au target of 948 mg/cm^2 and ^{12}C target of thickness 903 mg/cm^2). D1 - D8 values for respective Au and C target are shown in Table [3.3]. With these beam line conditions we calculate the velocities before, after and middle of the target at BigRIPS and tabulated in Table [4.2]. For the verification of the simulations, we also calculate the velocity in the ZeroDegree and compare the values with the experimentally measured ZeroDegree velocity (β_{ZD}). The energy information on each target is also listed in Table [4.2] and Table [4.3].

TABLE 4.2. The average velocity of the isotopes in BigRIPS (experimental), before the target, mid-target and end of target (calculated with LISE^{++}) are calculated and tabulated on the table. Also, the calculated and experimental ZeroDegree β value is tabulated. The respective energy values on the respective target is tabulated on the table and the energy values are given in unit [MeV/u]. The secondary target for this setup is ^{197}Au.

Isotopes	BReng	BR_β	B-Target$_{eng}$	B-Target$_\beta$	M-Target$_{eng}$	M-Target$_\beta$	A-Target$_{eng}$	A-Target$_\beta$	ZD-LISE$^{++}_{eng}$	ZD-LISE$^{++}_{\beta}$	βZD_{exp}
^{79}Zn	185.437	0.5518	177.37	0.5425	162.37	0.5242	147.48	0.5046	146.08	0.5027	0.5026
^{78}Zn	190.367	0.5573	182.33	0.5482	167.39	0.5305	152.6	0.5115	151.22	0.5097	0.5097
^{77}Zn	193.197	0.5604	185.12	0.5514	170.12	0.5338	155.29	0.5151	153.91	0.5133	0.5139

TABLE 4.3. The average velocity of the isotopes in BigRIPS (experimental), before the target, mid-target and end of target (calculated with LISE^{++}) are calculated and tabulated on the table. Also, the calculated and experimental ZeroDegree β value is tabulated. The respective energy values on the respective target is tabulated on the table and the energy values are given in unit [MeV/u]. The secondary target for this setup is ^{12}C.

Isotopes	BReng	BR_β	B-Target$_{eng}$	B-Target$_\beta$	M-Target$_{eng}$	M-Target$_\beta$	A-Target$_{eng}$	A-Target$_\beta$	ZD-LISE$^{++}_{eng}$	ZD-LISE$^{++}_\beta$	βZD_{exp}
^{79}Zn	185.171	0.5515	176.194	0.5411	152.570	0.5115	126.215	0.4737	126.200	0.4706	0.4719
^{78}Zn	190.004	0.5569	181.086	0.5468	157.597	0.5181	131.547	0.4818	130.014	0.4795	0.4803
^{77}Zn	192.521	0.5600	183.546	0.5496	159.988	0.5212	133.883	0.4853	132.349	0.4830	0.4853

- BR_{eng}= Energy value at BigRIPS spectrometer.
- BR_β= β value at BigRIPS
- B-Target$_{eng}$= Energy value before the target
- M-Target$_{eng}$= Energy value at middle of the target
- A-Target$_{eng}$= Energy after the target
- ZD-LISE$^{++}_{eng}$= LISE^{++} energy value at Zero-Degree
- ZD-LISE$^{++}_\beta$= LISE^{++} simulated β value
- βZD_{exp}= Experimental β value

4.2.5 DALI2 Efficiency

The Coulomb excitation cross-section is determined from the γ-ray transition decaying from the state populated in the reaction for eg. [^{79}Zn + ^{197}Au $\rightarrow$ $^{79}Zn^*$.] Therefore, we have to include DALI2 efficiency into the analysis carefully. To determine the cross-sections for the inelastic scattering channels, we have to take care of the number of emitted γ-rays and this information is extracted by fitting the measured energy spectrum to the simulation. Hence, both experimental measurement and simulation is crucial for verification.

1. DALI2 Efficiency from the Calibration Source: The efficiency of the detector is defined as the ratio of the number of events detected to the number of total events emitted.

$$\epsilon_{DALI} = \frac{I_\gamma(Detected)}{I_\gamma(Emitted)} = \frac{I_\gamma(Detected)}{A.t.\epsilon_{live}} \tag{4.11}$$

where I_γ is the number of the counts in the photopeak area for specific energy, A the activity of the gamma source, t the duration of the data taking time of the calibration sources in seconds. ϵ_{live} is the livetime of the DALI2 data acquisition system which is written as

$$\epsilon_{live} = \frac{N_{accepted-trig}}{N_{requested-trig}} \tag{4.12}$$

The duration of the data taking time for each calibration source including the empty target run and the live time (ϵ_{live}) are shown in Table [4.4]. The livetime is the lowest for ^{60}Co source since this source had the highest activity thus, too high counting rate at the date of the experiment.

The quantity I_γ detected by the detector can be obtained from the number of the counts in photopeak of the transition of the interest. Since the measurement from the DALI2 was

TABLE 4.4. Duration of the data taking time of different calibration source including the empty run target.

Isotopes	start time	End time	Time Duration	$\epsilon_{live}(\%)$	$A_0(Bq)$	A(Bq)
^{137}Cs	21:56:17	22:20:39	24m 22s	55.64	$8.23.10^3$	$7.32.10^3$
^{88}Y	22:24:15	22:52:59	28m 04s	39.61	$8.52.10^5$	$1.13.10^4$
^{60}Co	23:10:41	23:33:33	22m 52s	15.65	$8.81.10^4$	$4.52.10^4$
Empty-Run	10:57:53	11:26:55	28m 22s	-	-	-

taken with the empty frame in order to characterize the natural background, we could directly subtract the experimental background. First of all, the background spectrum was normalized according to the natural background peak of 40K at 1460 keV to subtract the backgrounds from the source spectra. And we know that the source spectra are taken for about 22 minutes each and the exact time are tabulated in Table [4.5]. Figure [4.11] shows the comparison between the experimental spectra of three different sources (pink histogram) together with the normalized background (blue histogram).

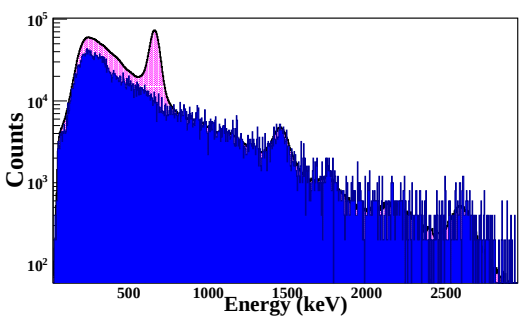

(a) Image a

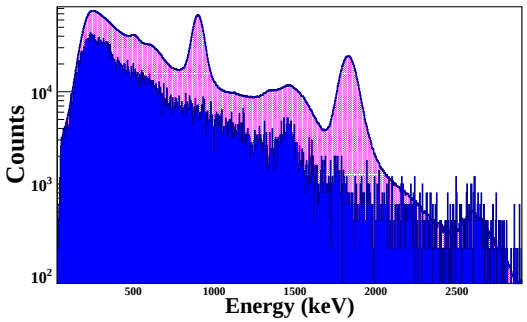

(b) Image b

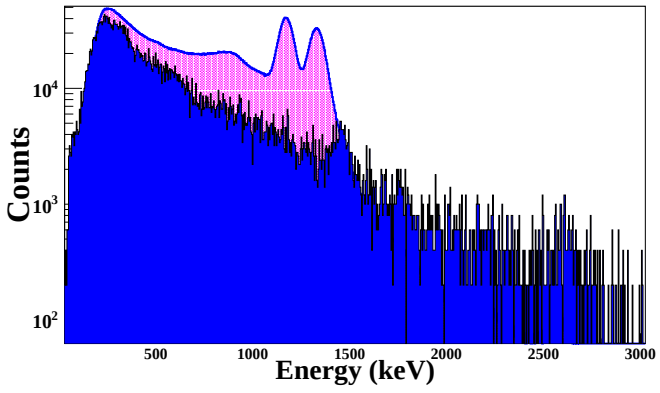

(c) Image c

Figure 4.11. Comparison between the experimental source (red histogram) and the normalized background (blue histogram) spectra for Image a. ^{137}Cs, Image b. ^{88}Y and Image c. ^{60}Co.

To calculate the activity of the source at the measurement date (Act), we can use the following relation:

$$A = A_0.e^{-\lambda\Delta t} \tag{4.13}$$

Here, A_0 is the known activity of the given source at specific date, Δt the time passed between the measurement date of A_0 and the calibration date of the experiment, and λ the decay constant of each sources. The Time duration *(t)*, live time (ϵ_{live}), and the activities (A_0) and *Act)* are also listed on the Table [4.5].

2. DALI2 Efficiency from Simulations: From the simulation, a sum of the Gaussian and background function was used to fit and calculate the integral of this function in the region of the peak, i.e. intensity of the simulated peak $I_\gamma(sim)$. The ratio of the simulated peak and the number of the simulated γ events gives the DALI2 efficiency from the simulations.

$$\epsilon_{sim} = \frac{I_\gamma(sim)}{N_{sim}} \tag{4.14}$$

Here, the number of the simulated events was taken as N_{sim}=1000000 in the analysis. The efficiency values from the experimental γ-ray source and the simulated measurement should be in good agreement to trust the simulation. It is very important step because the response function of the DALI2 obtained with GEANT4 will be used to fit the Doppler-corrected γ-ray spectra and to extract the intensity of each transition of the nuclei of interest. Figure [4.13] shows the comparison between the experimental and the GEANT4 simulated three different sources. The peaks of different sources at different energies were fitted to calculate and compare the efficiency for both experimental and GEANT4 simulated source. The number of detected gammas were obtained from the integral of the counts under the peaks. The red lines corresponds to the fit to the peak function (sum of the signal and the background function), blue lines are the fit for the background function and the green for the Gaussian signal function. The calculated efficiency from both the experimental and the GEANT4 simulations sources are listed in Table [4.5]. The errors in the efficiency is the total sum of the error from the number of counts in the peak, which is calculated as error in the integral of the gamma peak fit function, the error in the activity at the measurement date (a 5% error was considered) and a 5% statistical error was also considered while setting the range of the integral of the gamma peak functions. Figure [4.12] shows the comparison between the experimental and GEANT4 simulated γ-ray efficiencies with and without addback. The experimental efficiencies are shown with calculated error bar. The agreement between the experimental and simulated values with and without Addback are clearly seen for the lines of the ^{137}Cs and ^{88}Y sources while it is rather poor for the two lines of the ^{60}Co source. This is related to the difficulty in the determination of the background level for the both peaks and needs to be further investigated.

TABLE 4.5. Dali2 efficiency from experimental and GEANT4 simulated data: with and without addback.

Gamma Efficiency(%)				
With Addback			Without Addback	Without Addback
Energy(keV)	Experimental	GEANT4	Experimental	GEANT4
661.66 (^{137}Cs)	27.31 (7)	27.39	24.05 (7)	23.05
898.04 (^{88}Y)	24.29 (9)	24.83	20.67 (11)	21.07
1173.23(^{60}Co)	18.18 (9)	18.07	17.04 (9)	17.08
1332.49(^{60}Co)	15.56 (8)	17.24	13.11 (6)	16.04
1836.07 (^{88}Y)	14.84 (7)	15.55	11.92 (5)	11.16

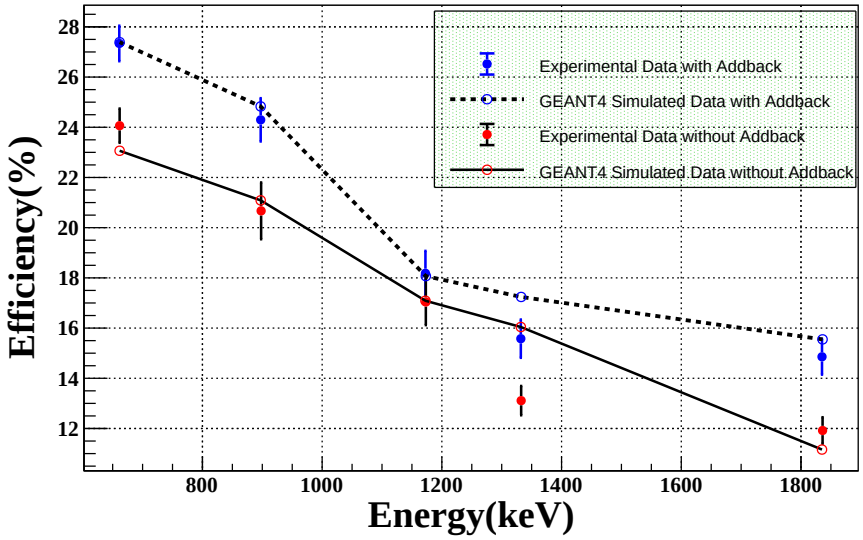

Figure 4.12. Experimental (error points) and GEANT4 simulated (lines) efficiencies with and without addback. The plotted efficiencies are shown in Table[4.5].

3. DALI2 GEANT4 simulations: After confirming that the simulations are in very good agreement with experimental spectra, we can now determine the number of γ-rays produced in the reaction for a given transition, i.e. $N(\gamma)$. For this, we use the efficiency from the simulations.

$$N(\gamma) = \frac{I_\gamma(detected)}{\epsilon_{sim}} \tag{4.15}$$

Where ϵ_{sim} is mentioned in equation 4.14, so that:

$$N(\gamma) = \frac{I_\gamma(detected)}{I_\gamma(sim)} \times N_{sim} \tag{4.16}$$

1000000 number of events were used in the simulation and the efficiency was calculated by fitting the response function, in the same way it was done for the source measurements explained above.

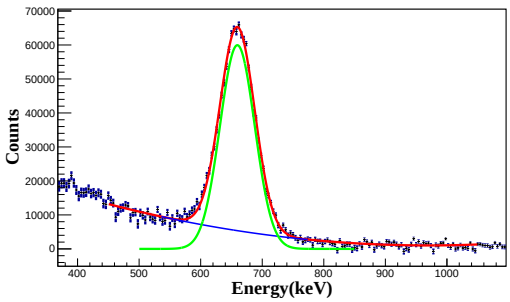

(a) ^{137}Cs background subtracted experimental source.

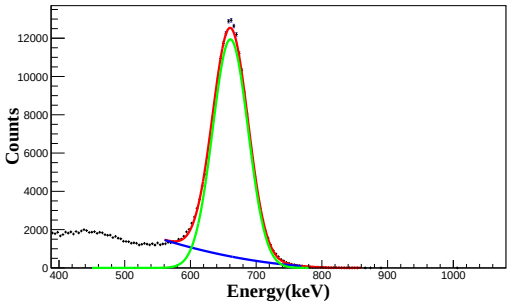

(b) ^{137}Cs GEANT4 simulated source.

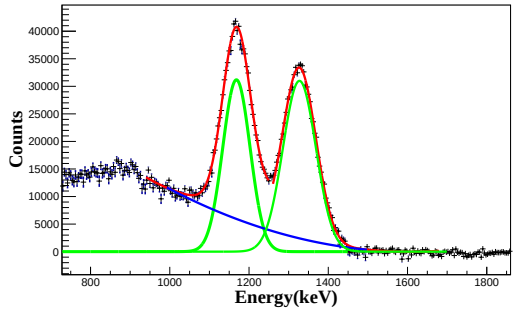

(c) ^{60}Co background subtracted experimental source.

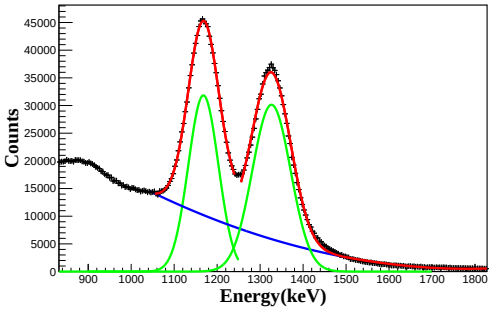

(d) ^{60}Co GEANT4 simulated source.

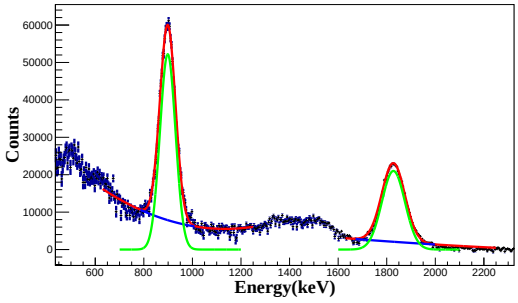

(e) ^{88}Y background subtracted experimental source.

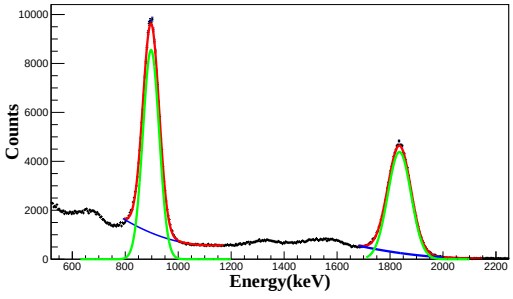

(f) ^{88}Y GEANT4 simulated source.

Figure 4.13. Comparison between the experimental background subtracted and GEANT4 simulated spectra for three different sources. The experimental and simulated spectra correspond to the black histograms, the green histogram are the global signal function, and the blue lines are the fit for the background function. The sum of the signal function and the background function is represented by the red lines in the histogram. No addback was applied.

Chapter 5

Experimental Results and Discussion

It doesn't matter how beautiful your theory is, it doesn't matter how smart you are. If it doesn't agree with experiment, it's wrong.

RICHARD P. FEYNMAN

In this chapter, the results obtained from the inelastic scattering of the selected and identified isotopes of interest (^{77,79}Zn) on ^{12}C and ^{197}Au targets are presented. The main aim of the experiment was to study the collective properties of the neutron-rich ^{77}Cu nucleus via Coulomb excitation. However, in addition to ^{77}Cu, the neighboring ^{77,79}Zn isotopes were populated simultaneously in the same experiment. The analysis has been performed firstly for ^{78}Zn since it is an even-even nucleus and thus a clean gamma-ray spectrum, at most the 2^+ state at 730 keV, was expected to be populated via Coulomb excitation. The results obtained for ^{78}Zn were then used to verify the method and to optimize the conditions for the scope nuclei, i.e. ^{77,79}Zn. For each beam and target combination, the γ-ray intensity of the identified transitions was determined from the number of γ-rays under the peak for incoming and outgoing beam particles, the target thickness, detector efficiency etc.

5.1 Neutron-rich Zn Isotopes

Having two extra protons outside the Z = 28 proton shell closure, the Zn isotopes form an interesting set of nuclei to study the evolution of the nuclear shell structure near ^{78}Ni shell closure. As explained in chapter 2, the evolution of single particle energies and shell gaps has been recently set down to the strongly attractive (or repulsive) tensor force acting between protons and neutrons with opposite (or similar) orientation of their intrinsic spin with respect to their orbital angular momentum. In neutron-rich Zn isotopes, neutrons occupy the $1g_{9/2}$ orbit, which separates the N = 40 and the N = 50 shell gaps. In addition to the shell evolution or even as a result of shell evolution, collectivity is expected along the Zn isotopes between N=40 and N=50 shell closures. One of the distinctive way to investigate the signature of collectivity is the reduced transition probability. It is very essential in the sense that the systematic study of the B(E2) serves as a benchmark to establish the theoretical models, predicting the nuclear properties of doubly magic ^{78}Ni. The $B(E2 : 2^+ \rightarrow 0^+)$ values for the $^{74-80}$Zn were extracted from low-energy Coulomb excitation experiment with radioactive ion beams at ISOLDE [19] while $B(E2 : 2^+ \rightarrow 0^+)$ values were studied later for $^{70-74}$Zn from a lifetime measurement at

LNL, Italy [50]. The extracted B(E2) values in these works suggested a (BE2) seniority parabola with maximum collectivity centered at N=44 in the Coulomb excitation and at N=42 in the lifetime experiment.

The even-odd, ^{77,79}Zn, having 30 protons and 47 and 49 neutrons, respectively, are currently the most exotic isotopes populated via Coulomb excitation. Note that prior to this work, there has been no information reported on B(E2) reduced transition probabilities in any of the even-odd Zn isotopes from ^{71}Zn to ^{79}Zn. This can be related to the fact that the structure of odd-even isotopes is expected to be more complicated compared to even-even nuclei. They show rather complicated level structure due to a multitude of configurations such as proton single-particle excitation, core-coupled states, and low lying collective modes.

The ground state spin-parity of $7/2^+$ and $9/2^+$ in ^{77}Zn and ^{79}Zn, respectively, was reported first time from the measurements of Q_β values [51]. The excited states of ^{77}Zn are known from the beta-decay of ^{77}Cu up to $\approx$ 4.6 MeV [52] while excited states up to $\approx$ 3.3 MeV in ^{79}Zn were populated in a $^{78}Zn(d,p)^{79}Zn$ transfer reaction [53]. Lower-mass Zn isotopes from ^{71}Zn to ^{75}Zn are primarily known from the beta decay of ^{71}Cu to ^{75}Cu and detailed information can be found in from Ref. [54].

5.1.1 ^{78}Zn

The γ-rays emitted by the decay of excited states populated through the inelastic scattering reactions with Au target were detected using the DALI2 spectrometer. The usage of a heavy target (Au in the present case) enabled the study of the intermediate energy Coulomb excitation. As already mentioned, for in-beam γ-ray spectroscopy experiments performed at relativistic energies, the γ-ray energy spectrum always presents a background component which is caused by atomic processes and is strongly depends on the atomic number of the projectile and the target. In the case of our Coulomb excitation experiment, the amount of background also depends on the detector angle. To get rid of these background component the most backward detectors (DALI2 ID lower than 60, which corresponds to angles larger than 94° in the laboratory frame) were deactivated. In order to determine the conditions on how many detectors to exclude and on the γ-ray multiplicity, γ-ray spectra were created in different combinations of detector ID and multiplicities. The details can be found in Appendix [A]. Finally, the benchmarked conditions in order to determine the cross sections from the γ yield are obtained as:

- The backward detectors counting from 1 to 90 excluded and multiplicity up to 3 at maximum for the Au runs and
- The backward detectors counting from 1 to 60 excluded in the case of $^{77,78}Zn$ and all the detectors were included in case of ^{79}Zn with multiplicity up to 3 at maximum for the C run

Figure [5.1 (a)and (b)] shows the Doppler corrected γ-ray spectra measured in coincidence with ^{78}Zn ions detected in BigRIPS and ZeroDegree spectrometer for the Au at multiplicity 1 and multiplicity $\leq$ 3, respectively. Similarly, Figure [5.1 (c)] is the Doppler corrected γ-ray spectra measured in coincidence with ^{78}Zn ions detected in BigRIPS and ZeroDegree spectrometer for the C target at multiplicity $\leq$ 3. The mid-target velocities (β = 0.5305 for Au target and β = 0.5181 for C target) were used for Doppler correction. The first excited 2^+ state has a lifetime of 18(4) ps [19] and included in the GEANT4 simulations. For those with

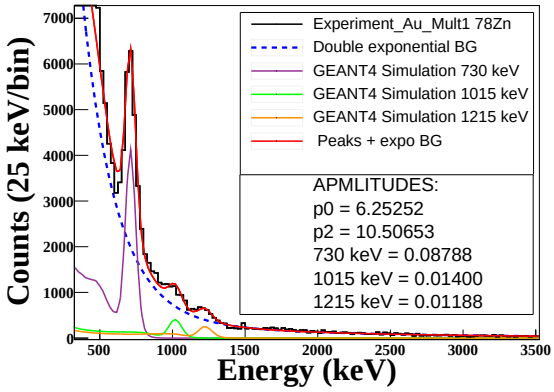

(a) For Au target with multiplicity 1

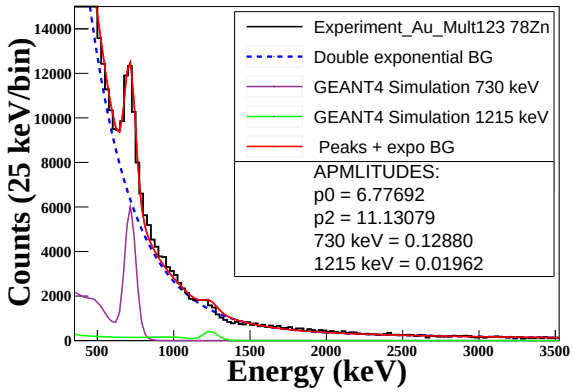

(b) For Au target with multiplicity$\leq$ 3

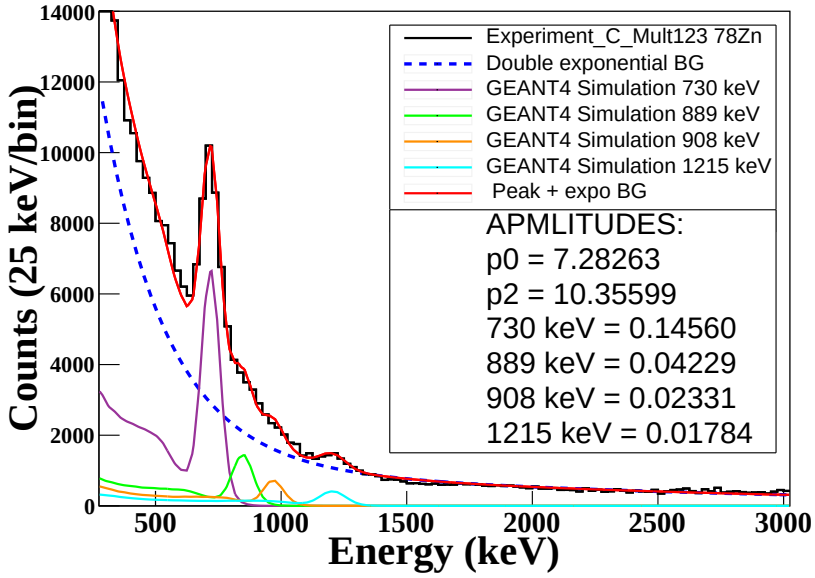

(c) For C target with multiplicity $\leq$3

Figure 5.1. Doppler corrected γ-ray spectra for ^{78}Zn from inelastic scattering on the Gold target and Carbon target.

unknown lifetimes, it was always considered as prompt in the simulations. The number of emitted γ-rays were determined by fitting the measured spectra with the simulated response function of the DALI2 array, keeping the line shapes and only scaling the amplitude of the peaks. The experimental spectra shown in Figure [5.1] were fitted with the DALI2 response functions simulated with GEANT4 code and the double exponentials for the background (blue dashed line). The total fit is shown by the red solid line for both targets.

Figure [5.1 (a) and (b)] shows the inelastic scattering of ^{78}Zn on Au target leading to the observation of a single transition at around 730 keV de-exciting from the 2^+ state to the ground state. The literature value is 730.2 keV [18, 19, 55]. The transition at 1015 keV is barely visible at multiplicity 1 but it is no more visible with multiplicity $\leq$ 3. In addition, the 1215 keV transition is clearly seen for multiplicity 1 and multiplicity $\leq$ 3. All of these transitions are fitted at multiplicity 1 and $\leq$ 3 to compare the γ intensity. 14000 number of gammas are obtained for 1015 keV transition at multiplicity 1 for Au target. Whereas 11880 and 19620 gammas are obtained for 1215 keV transition at multiplicity 1 and multiplicity $\leq$ 3, Au target condition. This shows that the γ-ray intensity is almost twice with multiplicity $\leq$ 3 for 1215 keV. This can be one of the evidence that γ transition at 1215 keV does not decay directly to the ground state.

Looking at the γ-ray spectrum measured for inelastic scattering of ^{78}Zn on the C target shown on Figure [5.1 b)], the peaks at 889 keV and 1215 keV are more visible along with the transition at 730 keV. The number of gammas obtained at 1215 keV for multiplicity 1 and $\leq$3 are 8090 and 17840, respectively. In this case also, the gamma intensity is twice with multiplicity $\leq$3. 730-keV and 889-keV energy peaks were already reported corresponding to $2^+ \rightarrow 0^+$ and $4^+ \rightarrow 2^+$ [56] transitions, respectively. However, the transition at 1215 keV energy is observed for the first time in this thesis work. To place the 1215 keV transition in the level scheme, a $\gamma\gamma$ coincidence analysis was performed. Figure [5.2] shows the $\gamma\gamma$ matrix for ^{78}Zn. The γ coincidences were analyzed by putting a gate on each transition. Some of the observed coincidences used to build the level scheme are shown in Figure [5.4]. The γ-ray coincidences with 730-keV transition show that all transitions are in coincidence with the first excited 2^+ state. Also, the 730 keV transition is observed in self-coincidence due to Compton events of the high energy transition. The gated spectra on 889 keV (Figure [5.4], red histogram) shows that the transition at 889 keV is clearly in coincidence with the transition at 730 keV. Similarly, blue histogram in Figure [5.4] shows the γ-ray with 1215 keV transition. This $\gamma - \gamma$ coincidence spectrum is very clean due to the low background in the energy gating region and since there are no coincidences with Compton events originating from higher energy transition, showing that the transition at 1215 keV is clearly in coincidence with the transition at 730 keV. Figure [5.3] shows the experimental level scheme of ^{78}Zn established from the $\gamma - \gamma$ analysis. The calculated γ-ray intensity for different energy transition of ^{78}Zn is shown in Table [5.1]. From the relative intensities given in the table for the transitions at 730 and 1215 keV on the Au and C targets indicate a (2_2^+) spin-parity assignment for the state at 1215 keV. Note that the uncertainties for the intensity values are not given in the table but expected to be between 10 and 15%. The detailed error analysis will be done in the future.

TABLE 5.1. Gamma intensity at multiplicity 1 and $\leq$3 with Au and C target for ^{78}Zn.

Gamma-ray intensity of ^{78}Zn		
Energy (keV)	Multiplicity = 1	Multiplicity$\leq$3
730 (for Au Target)	87880	128800
730 (for C Target)	88000	145600
1215 (for Au Target)	11880	19620
1215 (for C Target)	8090	17840

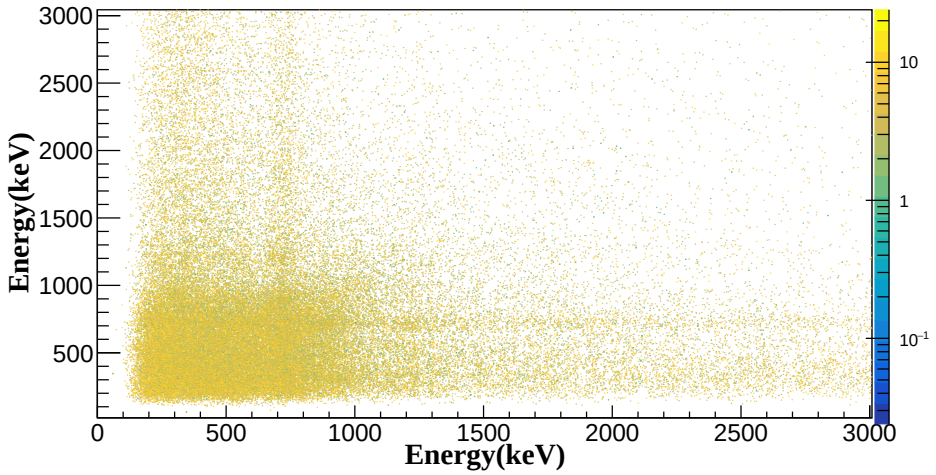

Figure 5.2. $\gamma - \gamma$ matrix for the ^{78}Zn isotope

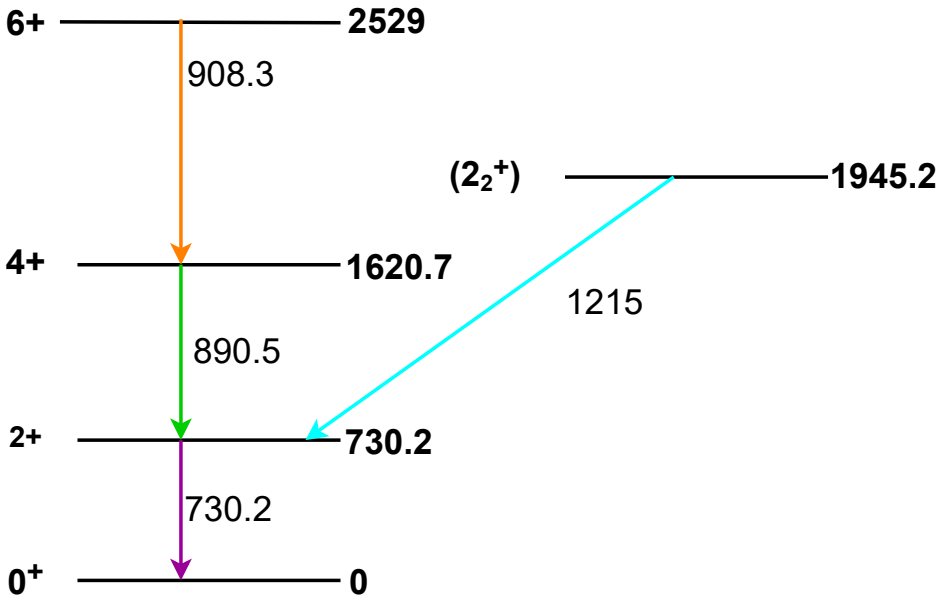

Figure 5.3. Experimental level scheme of ^{78}Zn established from the $\gamma - \gamma$ analysis. The energies are quoted in keV. Each transition is given in different color that corresponds to the simulated response functions of these transition in Figure [5.1] Carbon target.

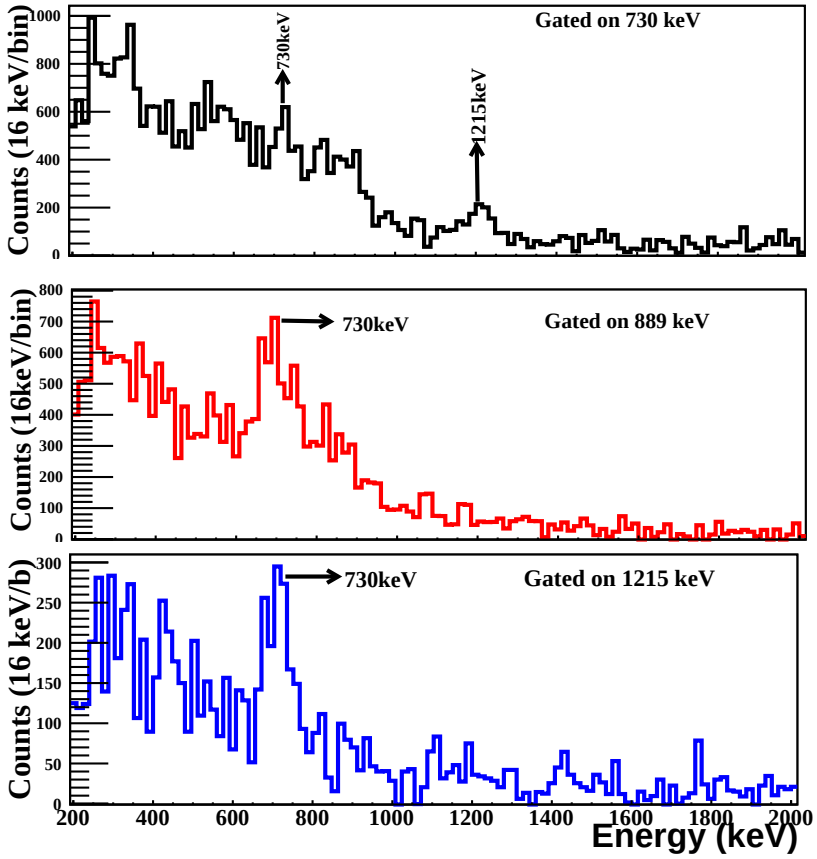

Figure 5.4. Co-incidence gate on 730 keV, 889 keV, and 1215 keV peaks

5.1.2 ^{79}Zn

Excited states of the ^{79}Zn were investigated through the inelastic scattering on the Au and C targets. Doppler corrected γ-ray energy spectra for the inelastic scattering of ^{79}Zn on both Au and C target are shown in Figure [5.5] considering without addback. Similar to that of ^{78}Zn isotope, the γ-ray spectra with Au target is obtained considering only the most forward detectors i.e. DALI2 ID higher than 90, while all the detectors were considered in the analysis with C target. The mid-target velocities (β = 0.5242 for Au target and β = 0.5115 for C target) were used for Doppler correction.

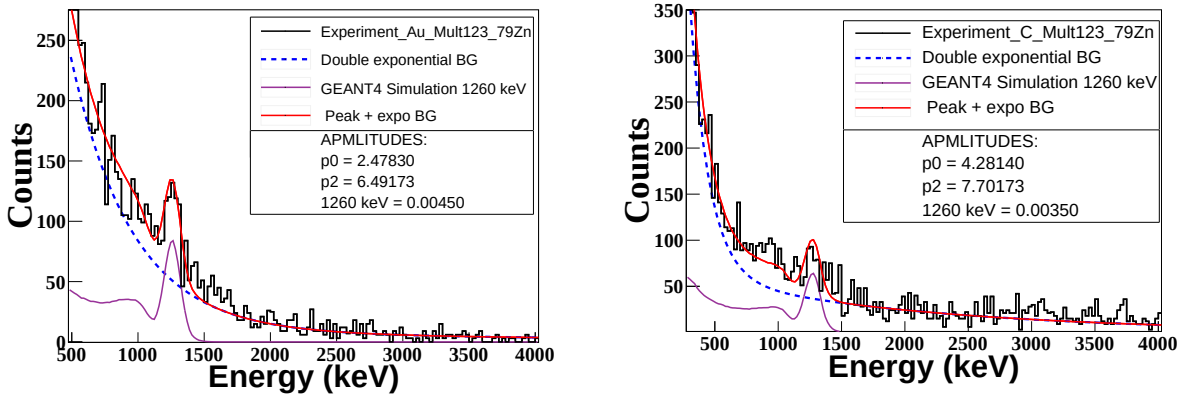

(a) Au target

(b) For C target

Figure 5.5. Doppler corrected γ-ray spectra for ^{79}Zn from inelastic scattering on the Gold target and Carbon target.

The number of emitted γ-rays were determined by fitting the measured spectra with the simulated response function of the DALI2 array, keeping the line shapes and only scaling the amplitude of the peaks. The experimental spectra shown in Figure [5.5] were fitted with the DALI2 response functions simulated with GEANT4 code and the double exponential for the background (blue dashed line). The total fit is shown by the red solid line for both targets. The number of gammas under 1260 keV peak of ^{79}Zn, obtained for different multiplicity, are shown in Table [5.2]. The uncertainties for the intensity values (expected to be between 10 and 15%) are not given and need to be estimated in Table [5.2].

TABLE 5.2. Gamma ray intensity at multiplicity up to 3 with both Au and C target for ^{79}Zn.

Gamma-ray intensity of 1260-keV transition		
^{79}Zn Isotope	Au Target	C Target
Multiplicity = 1	3240	2660
Multiplicity$\leq$2	3960	3440
Multiplicity$\leq$3	4500	3500

The first excited state (983 keV, $5/2^+$) decays directly to the ground state ($9/2^+$) and it is fed by the 441 keV transition [53]. Looking at the γ-ray spectra of ^{79}Zn in Figure [5.5], the strongest transition was observed at energy of 1260 keV for both targets. This transition was not observed in the previous $^{78}Zn(d,p)^{79}Zn$ transfer reaction of Orlandi et al [53] and newly observed in the present work for the first time. The Coulomb excitation will most likely populate the states with E2 electric quadrupole transitions and therefore, the state at 1260 keV can be either $5/2^+$ or $13/2^+$. If this state had a $5/2^+$ spin parity, it should have been fed by the states above in the work of Orlandi et al. A $13/2^+$ state, on the other hand, would not have been populated in the (d,p) transfer reaction due to the required high angular momentum transfer.

While the shell model calculations are necessary to better understand the origin and the spin-parity of the observed state, this state can appear as a result of the core-coupled excitation. In the case of ^{79}Zn, the core-coupling excitation is due to the coupling of a neutron hole in $g_{9/2}$ to the 2^+ state of the even-even ^{80}Zn core. Such coupling will result in a similar excitation energy and the observed 1260 keV is not very far from the first excited 2^+ state of ^{80}Zn, 1492 keV, as shown in Figure [5.6]. Furthermore, if the 1260-keV state-observed is due to particle-core coupling where the even-even core is ^{80}Zn, the $B(E2 : 13/2^+ \rightarrow 9/2^+)$ in ^{79}Zn should be similar to the $B(E2 : 2^+ \rightarrow 0^+)$ in ^{80}Zn. This will be further investigated. Such particle-core coupling mechanism is expected in the odd-even nuclei in the ^{78}Ni region [57]. Indeed, the 946-keV state in ^{77}Cu was predicted to be due to the coupling of a proton in $f_{5/2}$ to the 2^+ state of the even-even ^{76}Ni core [17, 58] and the present data subject to this thesis have clearly shown the presence of this state in ^{77}Cu through Coulomb excitation [59].

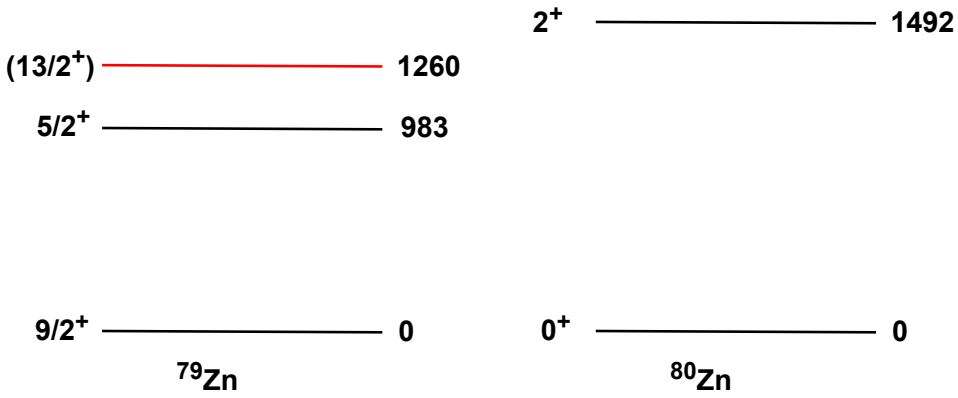

Figure 5.6. Partial level scheme of ^{79}Zn and ^{80}Zn. The 1260-keV transition shown with red level is newly observed in the present work for the first time. Higher energy transitions are not included in the level scheme. The known transitions of ^{79}Zn are obtained from Orlandi et al [53] whereas the level scheme of ^{79}Zn is taken from NNDC [54].

The γ-ray spectrum observed from the C target in Figure 5.5, indicates another peak at around 1380 keV. In order to further investigate this peak, the $\gamma\gamma$ coincidence analysis would be necessary, similar to the case of ^{78}Zn. However, present data do not allow to perform coincidence analysis for ^{79}Zn as seen in Figure [5.7]. Figure [5.7] shows the $\gamma - \gamma$ matrix for ^{79}Zn isotope and the $\gamma - \gamma$ matrix do not looks very promising because of the low statistics of the presented data.

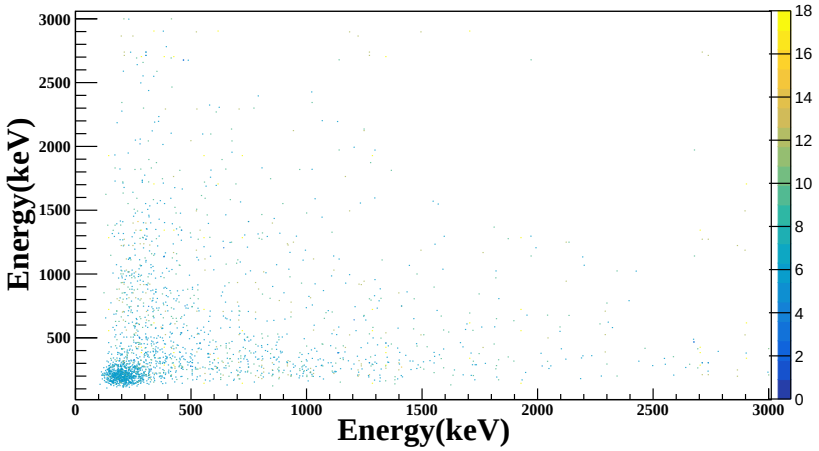

Figure 5.7. Gamma coincidence matrix of ^{79}Zn, created for the C-target data.

5.1.3 ^{77}Zn

The Doppler corrected γ-ray energy spectra from the inelastic scattering of ^{77}Zn on C and Au target are shown in Figures [5.8 and 5.9] with no addback condition applied. From the scattering on the Au target, five γ-ray transitions with energies of 890 keV, 1364 keV, 1410 keV, 1580 keV and 2040 keV were observed. These observed transitions are fitted with the DALI2 response functions simulating with GEANT4 code to calculate the γ-ray intensity of each peak. The 1364 keV and 1409 keV transitions are already known. The transitions with the energy around 1583 keV and 2037 keV with the cyan and orange line in Figure [5.8], are not well separated. However, these transition is added to improve the fit and determine its impact on the number of γ-ray intensity on 1364 keV and 1410 keV transitions.

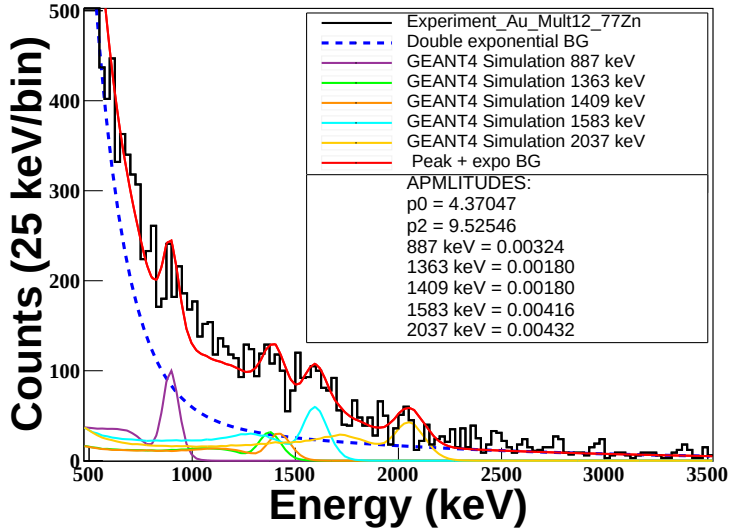

Figure 5.8. Doppler corrected γ-ray spectra for ^{77}Zn from inelastic scattering on the Gold target.

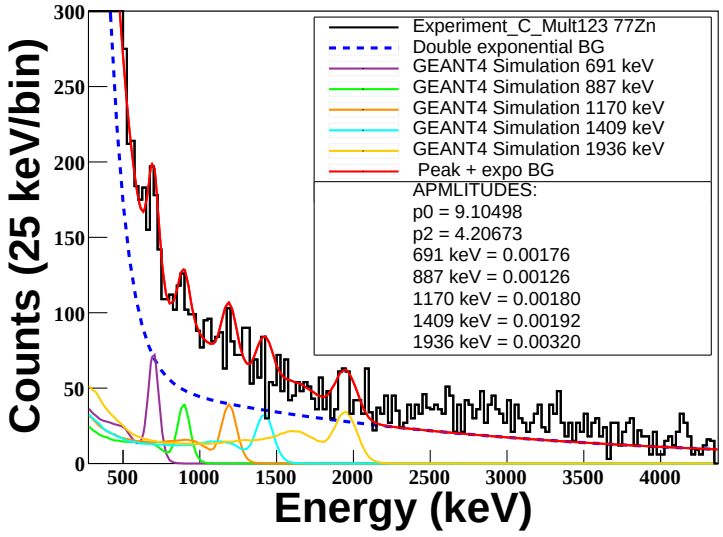

Figure 5.9. Doppler corrected γ-ray spectra of ^{77}Zn from the inelastic scattering on the Carbon target

The γ-ray spectrum of ^{77}Zn from the Coulomb excitation on the Au target shows distinct differences compared to those of ^{78}Zn and ^{79}Zn. Multiple peaks are visible and can be populated via Coulomb excitation with a certain fraction from the nuclear excitation. However, the statistics, especially for the C target as seen in Figure [5.9], do not allow us to perform

further analysis on these observed peaks. Nevertheless, multiple peaks observed can be related to a different excitation mechanism for ^{77}Zn [51, 52, 60]. It was discussed in several earlier works that the deformation can appear as a result of the $(\nu 1g_{9/2})^{-3}$ three quasi-particle interaction. A spin multiplet of states from $3/2^+$ to $21/2^+$ was observed in the silver isotopes due to the similar configuration but with protons, $(\pi 1g_{9/2})^{-3}$ and the states were found to be deformed [61]. $(\nu 1g_{9/2})^{-3}$ configuration in ^{77}Zn can be the reason why its ground state spin-parity is not $9/2^+$ as in ^{79}Zn but $7/2^+$. Future experiments are necessary to further investigate the low-lying states in ^{77}Zn isotope.

Summary and Outlook

The γ-ray spectroscopy at intermediate energy Coulomb excitation of ^{77,79}Zn isotopes in the ^{78}Ni region has been discussed in this thesis work. The inelastic scattering of ^{77}Zn, ^{78}Zn and ^{79}Zn isotopes on the Au and C target at the energy around 175 MeV/u has been studied. These isotopes are produced at the Radioactive Ion Beam Factory (RIBF), RIKEN Nishina Center, Japan. A ^{238}U primary beam with an energy of 345 MeV/u was impinged on a ^{9}Be target of thickness 3 mm to produce the ions of interest as a secondary beam. Thus produced ions are selected, separated and identified with the help of the BigRIPS fragment separator. The identified particles of interest are then delivered to the secondary target (reaction target) for inelastic measurements with the Au and C targets. The $B\rho - \Delta E - TOF$ method was used for the identification of the reaction products whereas the γ-rays emitted due to the de-excitation were measured in coincidence by an array of γ-ray DALI2 detector. The secondary target was placed in between the DALI2 γ-ray detector, which is an array formed by 186 NaI(Tl) detectors, for highly efficient γ-ray detection.

The experimental conditions were simulated to obtain the DALI2 γ-ray response functions of the transitions. For this, the GEANT4 simulation package for DALI2 detectors was used. The response function of the DALI2 obtained with the GEANT4 was used to fit the Doppler-corrected γ-ray spectra of ^{77,79}Zn and to extract the γ-ray intensity of each transition. We have discussed the details followed in the analysis of the data in order to improve the quality of γ-ray spectra detected with DALI2 detectors. Using the Doppler corrected γ-ray spectra for ^{79}Zn, a new transition at 1260 keV has been obtained in the present experiment. The tentative spin assignment and origin of this newly identified collective state were discussed. In addition to this, the newly observed 1215 keV transition was observed for ^{78}Zn, and to place this transition in the level scheme, a $\gamma\gamma$ coincidence analysis was performed. The γ-ray spectrum obtained for ^{77}Zn shows a rather scattered structure with several transitions. A distinct difference is seen in the case of ^{77}Zn compared to ^{78}Zn and ^{79}Zn. This was also discussed in this thesis work. To study the collective properties of the even-odd ^{77,79}Zn in detail, the next step is to obtain the reduced transition probabilities, B(E2) values. The calculated γ-ray intensity can be used to achieve the cross-section and finally to calculate the B(E2) values. To obtain this value further analysis is needed and I will mention it as the future continuation of this thesis work. The possible continuations of the studies presented in this thesis are:

- **Scattering angle determination**: To obtain the differential inelastic scattering cross-section, we need to know the angular distribution of the scattered ions. To measure the scattering angle two PPACs were installed before the reaction target (to obtain the incoming angle) and one extra PPAC situated behind the target (to obtain the outgoing angle).
- **Particle transmission through BigRIPS and ZeroDegree spectrometer**: The next requirement to determine the cross-section is to measure the number of particle losses along the

BigRIPS and ZeroDegree spectrometer. The transmission of the ZeroDegree spectrometer is not 100% but depends on the scattering angle, θ, the observed γ-ray intensity for each angular gate has to be corrected with the average transmission of the angular bin. The transmission of each angular bin can be obtained by comparing the number of ions measured in BigRIPS to the number of ions measured in ZeroDegree spectrometer.

- The obtained absolute cross sections from the experiment will be converted into B(E2) values using a proper reaction code. In the present case the code called FRESCO [62] is planned to be used for this purpose.
- As mentioned in the result section, 1260-keV transition observed in ^{79}Zn might be because of the particle-core coupling of a neutron hole in $g_{9/2}$ to the 2^+ state of the even-even ^{80}Zn core. In order to confirm this the $B(E2 : 13/2^+ \rightarrow 9/2^+)$ has to be determined and compare this with the $B(E2 : 2^+ \rightarrow 0^+)$ of ^{80}Zn. Furthermore, to better understand and accurately assign the spin parity to this transition at 1260 keV for ^{79}Zn, the shell model calculations are also necessary.
- Finally the results will be published in a scientific journal.

Appendix A

DALI2 γ-ray spectra of ^{78}Zn

As mentioned in the very first chapter, the well known 730 keV transition of ^{78}Zn was used to check the validity of the method for obtaining the γ-ray intensity. The γ-ray peak at 730 keV of ^{78}Zn is best suited for this task because the spectrum has only one transition and rather well populated. I have not included all those fitted plots and results in the result section, which I am going to include here. In-beam γ-ray spectroscopy experiments performed at relativistic energies present a background component caused by atomic process. This atomic background is strongly dependent on the atomic number of the projectile and the target. Therefore, while choosing Au target the most downstream detectors with DALI2 ID less than 90 were deactivate during the analysis. Similarly, in case of C target DALI2 ID lower than 60 were deactivated during analysis. In this section I will present the results when considering different DALI2 ID cuts and conditions. Remember that, all the γ-ray spectra present in result and appendix sections were produced without addback. The reason for this is mentioned in section 4.2.3. Figure [A.1] shows the Doppler corrected γ-ray spectrum for ^{78}Zn from the inelastic scattering on Au target plotted against DALI2 detector number when first 60 DALI2 detectors deactivated. Figure [A.2] shows the DALI2 gamma ray spectra of ^{78}Zn in which first 60 DALI2 detector IDs were deactivated during the analysis whereas, in Figure [A.3], the first 90 detectors were deactivated. It is very clear from these two figures that, the γ-ray peak at 730 keV is very prominent and the fits are better when first 90 detectors were blacklisted. In a similar way, the analysis with first 80 and 100 detectors deactivated conditions (fitted spectra not shown here) was also done to further verify and obtain the best possible fit and hence the gamma intensity. However, the maximum number of γ-ray intensity is obtained when first 90 detectors were deactivated. In conclusion, the maximum number of γ-ray intensity is obtained from the spectra when the first 90 detectors deactivated during analysis. Also, the maximum number of counts was obtained when the multiplicity is $\leq$3 for both conditions. Table [A.1] shows the calculated γ-ray intensity at different multiplicities for Au and C target when the most forward detectors were (first 60 and 90 detectors) deactivated during analysis.

TABLE A.1. Gamma intensity for different multiplicity for both Au and C target for $2^+ \rightarrow 0^+$ transition of ^{78}Zn.

Gamma-ray intensity			
^{78}Zn Isotope	DALI2 ID $\leq$60 off (Au)	DALI2 ID $\leq$90 off (Au)	DALI2 ID $\leq$60 off (C)
Multiplicity$\leq$ 2	216000	238000	175200
Multiplicity$\leq$3	224200	245100	200000
Multiplicity$\leq$4	230400	201600	218400
Multiplicity$\leq$5	216000	184600	217800

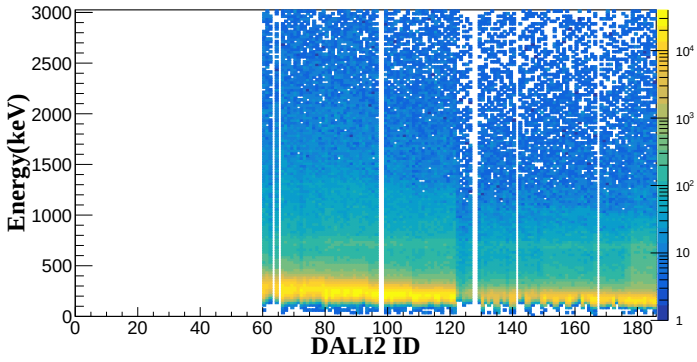

Figure A.1. Doppler-corrected -ray spectrum for ^{78}Zn from the inelastic scattering on the Au target plotted against the DALI2 detector number. Detector number 97, 98 and 168 did not produce signal and was inoperable during the entire experiment. Detector number 127,128 and 142 have worse energy resolution and were removed from the analysis.

The same analysis procedure was followed in the case of the C target run and the optimum condition was obtained when the first 60 detectors were deactivated. Figure [A.4] shows the Doppler corrected γ-ray spectra for ^{78}Zn from inelastic scattering on the Carbon target with DALI2 ID lower than 60 were deactivated. The calculated γ-ray intensity at different multiplicities are shown in Table [A.1].

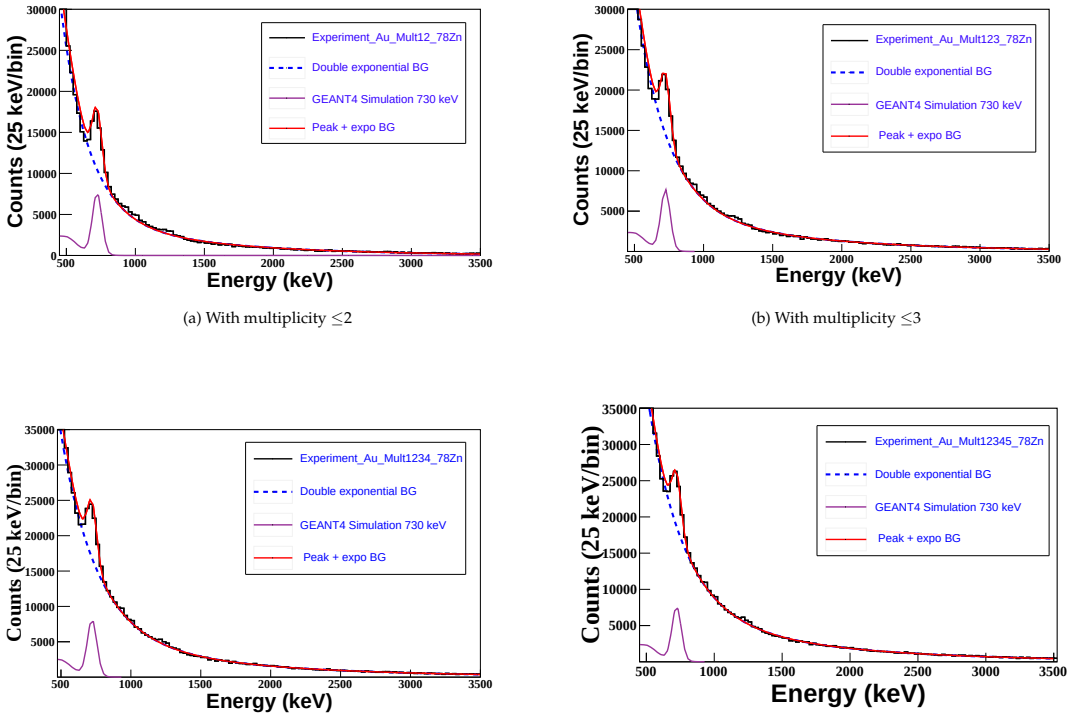

(a) With multiplicity ≤2

(b) With multiplicity ≤3

(c) With multiplicity ≤4

(d) With multiplicity ≤5

Figure A.2. Doppler corrected γ-ray spectra for ^{78}Zn from inelastic scattering on the Gold target with DALI2 ID lower than 60 were deactivated during the analysis

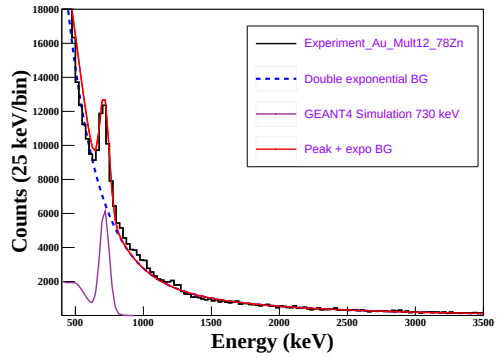

(a) With multiplicity ≤2

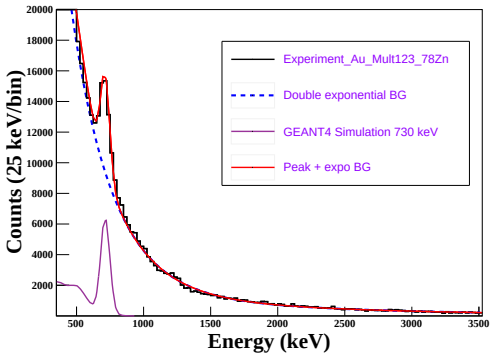

(b) With multiplicity ≤3

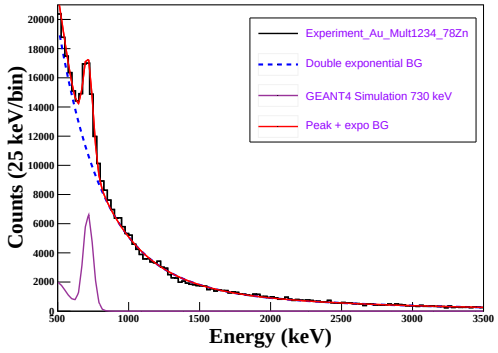

(c) With multiplicity ≤4

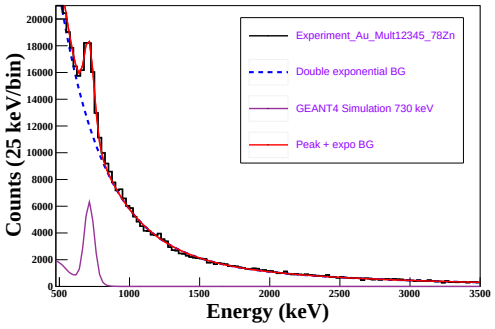

(d) With multiplicity ≤5

Figure A.3. Doppler corrected γ-ray spectra for ^{78}Zn from inelastic scattering on the Gold target with DALI2 ID lower than 90 were deactivated during the analysis

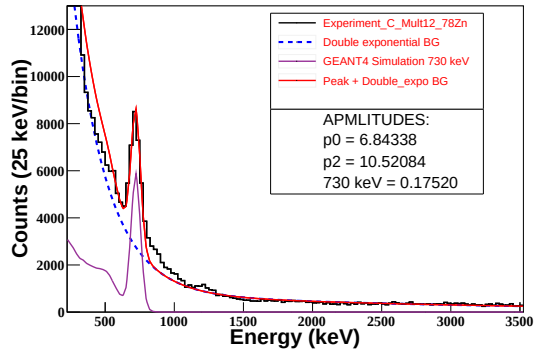

(a) With multiplicity ≤2

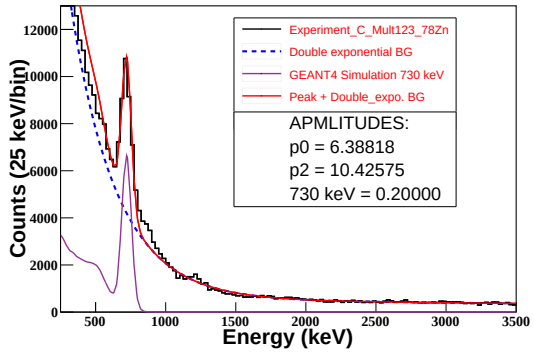

(b) With multiplicity ≤3

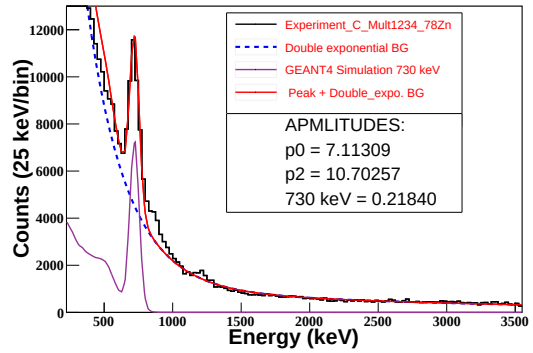

(c) With multiplicity ≤4

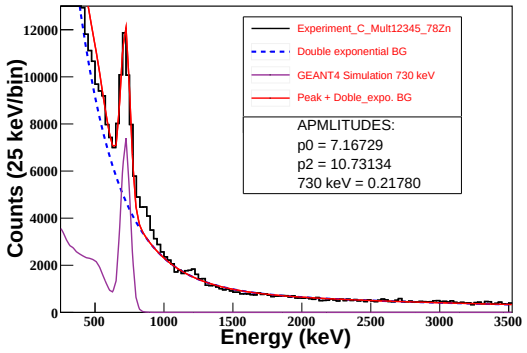

(d) With multiplicity ≤5

Figure A.4. Doppler corrected γ-ray spectra for ^{78}Zn from inelastic scattering on the Carbon target with DALI2 ID lower than 60 were deactivated.

DALI2 γ-ray spectra of ^{79}Zn

In the result section of ^{79}Zn, the γ-ray intensity of ^{79}Zn with multiplicity up to 3 at maximum, obtained for both Au and C was presented. Similarly, the γ-ray spectra of ^{79}Zn with multiplicity ≤ 3 was shown there. In this section, the DALI2 γ-ray spectra of ^{79}Zn at multiplicities 1 and ≤ 2 are shown. Figure [A.5] shows the Doppler corrected DALI2 γ-ray of ^{79}Zn from the inelastic scattering on the Gold target with multiplicity a) 1 and b) $\leq$2. Similarly, Figure [A.6] shows the Doppler corrected DALI2 γ-ray of ^{79}Zn from the inelastic scattering on the C target with multiplicity a) 1 and b) $\leq$2.

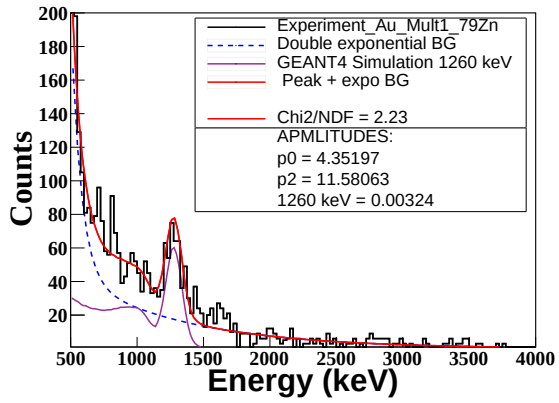

(a) With multiplicity = 1

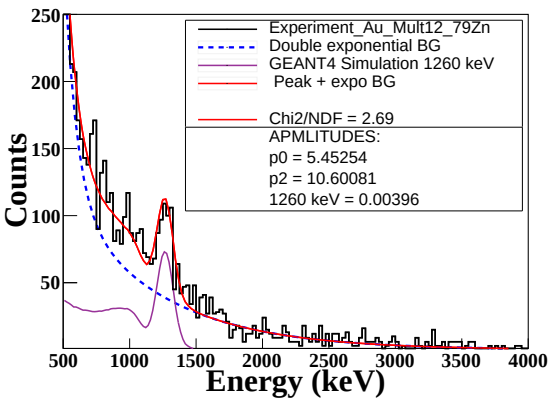

(b) With multiplicity $\leq$2

Figure A.5. Doppler corrected γ-ray spectra of ^{79}Zn from inelastic scattering on the Gold target with multiplicity a) 1 and b) $\leq$2.

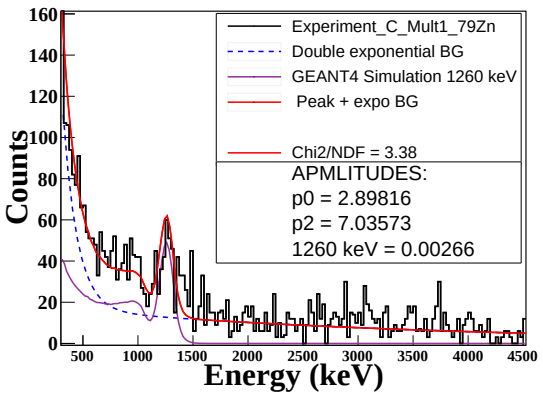

(a) With multiplicity = 1

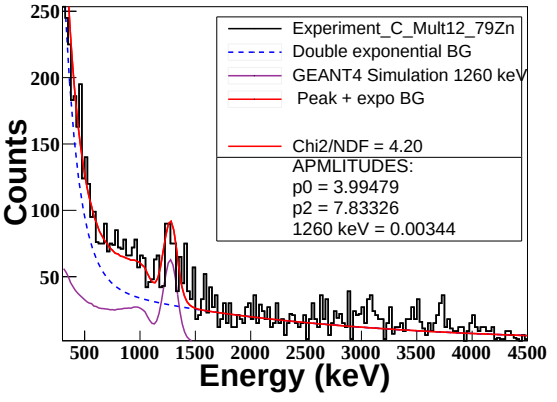

(b) With multiplicity $\leq$2

Figure A.6. Doppler corrected γ-ray spectra of ^{79}Zn from inelastic scattering on the Carbon target with multiplicity a) 1 and b) $\leq$2.

Appendix B

The GEANT4 Simulation Code for DALI2 γ-ray Detector

The GEANT4 simulation for the DALI2 γ-ray detectors was briefly explained in section 3.7. The simulation code for the DALI2 γ-ray detectors used in RIKEN-RIBF includes the geometry of the DALI2 crystals, the beam pipe, absorbers, and the target holders. The simulation package is divided into three steps (EventGenerator, EventBuilder and Reconstructor) and are already explained in section 3.7. In this section, all the parameters used in EventGenerator, EventBuilder and Reconstructor are now discussed subsequently.

B.1 EventGenerator

The EventGenerator is the first step of the simulation. All the input parameters of EventGenerator, as defined in section 3.7, are now defined subsequently below. If not specified differently, the units are cm and degrees, respectively.

- **BEAMISOTOPE** [A_P Z_P Q_P]: It contains the information on the type of the projectile P in the order, mass (A_P), the element number (Z_P) and the charge state (Q_P).
- **BEAMENERGY** [E_P $\Delta E(FWHM)_P$]: The total energy of the projectile E_P before striking on the the target and the width of the energy distribution $\Delta E(FWHM)_P$ in MeV/u is defined.
- **BEAMPOSITION and BEAMANGLE**: The position and angle of the projectile before impinging on the target.
- **TARGET** $Type$ $Size_X$ $Size_Y$ $Thickness_Z$: The types of target (for example 1 for Au and 3 for C as shown in Listing [B.1, B.2]), its size and thickness is defined here. The target thickness is given in mg/cm^2.
- **BORREL** Option_{Borrel} B_n: If Option_{Borrel} = 0, the velocity shift for the fragmentation process is not defined. B_n is the binding energy (in MeV) per ablated nucleon.
- **GAMMAINPUT**: It specifies the location of the file which includes the level and decay scheme to be simulated.

- **THETARANGE** $\theta_{\gamma min}$ $\theta_{\gamma max}$: Polar angular range in the moving frame is defined here. If the detectors cover only extreme forward angles, $\theta_{\gamma min}$ can be set to 0 and $\theta_{\gamma max}$ to 180, thereby reducing the simulation time and file-size.
- **NUMBEROFEVENTS** N_{events}: The number of reactions to be simulated is defined here.
- **DEFAULTCUTVALUE** L_{cut}: It specifies the default cut value in mm used in the simulation.
- **DEDXTABLE** $Option_{dEdX}$ $File_P$ $File_E$: If $Option_{dEdX}$ = 1, then the energy loss of the projectile and the ejectile should be included. In our it was calculated from LISE^{++}. $File_P$ $File_E$ specify the location of these tables for projectile and ejectile, respectively.
- **OUTPUFILENAME** $File_{out}$: It specifies the location of the output file name. The output file generated by the EventGenerator is saved as root file.

The EventGenerator input files with above defined parameters for the beam isotope ^{78}Zn, with the Au and C target are shown in Listing [B.1] and [B.2]. The simulation was performed in a similar way for ^{77}Zn and ^{79}Zn.

```

BEAMISOTOPE 78 30 30
BEAMENERGY 182.33 2
BEAMPOSITION 0 1. 0 1.
BEAMANGLE 0.0 0.0 0.0 360.0
TARGET 1 3.0 3.0 948
TARGETANGULARBROADENING 0 0.00
MASSCHANGE 0 0
BORREL 0 8.
GAMMAINPUT .../78Zn/78Zn_level_730kev.in
THETARANGE 0.0 180.0
NUMBEROFEVENTS 1000000
DEFAULTCUTVALUE 0.001
OUTPUTFILE ../78Zn/78Zn_GOLD_generator.root
DEDXTABLE 1 .../78Zn/dEdx_78Zn_GOLD.in .../78Zn/dEdx_78Zn_GOLD.
END
```

Listing B.1. EventGenerator.in ^{78}Zn Gold Target

```
BEAMISOTOPE 78 30 30
BEAMENERGY 181.086 2
BEAMPOSITION 0 1. 0 1.
BEAMANGLE 0.0 0.0 0.0 360.0
TARGET 3 3.0 3.0 903
TARGETANGULARBROADENING 0 0.00
MASSCHANGE 0 0
BORREL 0 8.
GAMMAINPUT ..../78Zn/78Zn_level_730kev.in
THETARANGE 0.0 180.0
NUMBEROFEVENTS 1000000
DEFAULTCUTVALUE 0.001
OUTPUTFILE OUTPUTFILE ../78Zn/78Zn_CARBON_generator.root
DEDXTABLE 1 ..../78Zn/dEdx_78Zn_CARBON.in ..../78Zn/dEdx_78Zn_CARBON.in
END
```

Listing B.2. EventGenerator.in ^{78}Zn Carbon Target

B.2 EventBuilder

The EventBuilder is the second step of simulation which simulates the γ-ray detection responses and uses the output of EventGenerator as the input file. The different parameters used in this step are defined as follows:

- **INPUTFILE and OUTPUTFILE** FILE$_{in}$ FILE$_{out}$: The location of the input root file generated by the EventGenerator is defined here. Similarly, FILE$_{out}$ gives the location of the output root file generated in this step.
- **DALI2INCLUDE** i: If i=1, the geometry of the DALI2 detector arrays are included in the simulation. They require an input file that specifies the position and rotation relative to the target.
- **DALI2FIINCLUDE** i: If i=1, the first interaction point of a γ-ray is determined for every crystal of the DALI2 array.
- **ZPOSSHIFT** f: I specifies how many cm the detectors are shifted relative to the target. Positive values correspond to an upstream shift, negative to a downstream shift.
- **DALI2ENERGYRESOLUTIONINDIVIDUAL** i: If i=1, the energy resolution is of the DALI2 detector is included in the simulation. The energy resolution of the DALI2 is read from the text file.
- **POSDETECTORONTARGETRESOLUTION** x: x determines the precision of the tracking onto the target position from imaginary detectors. x is given in cm.
- **POSDETECTORAFTERTARGETDISTANCE and POSDETECTORAFTERTARGETRESOLUTION** a b: The distance a (in cm) of a position sensitive detector after the secondary target and its resolution b in x and y is defined here.
- **BETARESOLUTION** a: The β-resolution a = $\Delta\beta/\beta(FWHM)$ for the time-of-flight measurement before the target. This parameter is necessary for event-by-event Doppler correction of the emitted γ-rays based on the particles' velocities.
- **BEAMPIPEINCLUDE** i: If i=1, the beam pipe will be included in the simulation.
- **SHIELD** r D$_{Pb}$ D_{Sn}: It specifies the thickness of absorber material placed along beam pipe. r is the inner radius of the absorber tube. D$_{Pb}$ D_{Sn} the thickness in cm of the Pb and Sn.
- **TARGETHOLDERINCLUDE** i: If i=1, the target-holder will be included in the simulation. i=0 means the target-holder is not included in the simulation.

The EventBuilder input file with above defined parameters for the beam isotope ^{78}Zn is shown in Listing [B.3]. All the parameters are also same for ^{77,79}Zn.

```
INPUTFILE  .../78Zn/78Zn_Au_generator.root
OUTPUTFILE .../78Zn/78Zn_Au_builder.root
DALI2INCLUDE 1
DALI2FIINCLUDE 1
ZPOSSHIFT -2.75
DALI2ENERGYRESOLUTIONINDIVIDUAL 1
POSDETECTORONTARGETRESOLUTION .3
POSDETECTORAFTERTARGETDISTANCE 100.
POSDETECTORAFTERTARGETRESOLUTION .3
BETARESOLUTION 0.001
BEAMPIPEINCLUDE 1
SHIELD 7.5 0.1 0.1
TARGETHOLDERINCLUDE 0
END
```

Listing B.3. EventBuilder.in ^{78}Zn

B.3 The Reconstructor

The Reconstructor is the final step of the simulation which performs the Doppler correction of the simulated γ-rays including addback procedures. Following parameters are specified in the Reconstructor:

- **INPUTFILE and OUTPUTFILE** FILE$_{in}$ FILE$_{out}$: The location of the input root file generated by the EventBuilder is defined here. Similarly, FILE$_{out}$ gives the location of the output root file generated in this step.
- **DECAYPOSITIONZ** f: It specifies average z-positon along the beam-axis shifts as a function of the excited states' lifetimes. This value can be inserted to correct for this effect.
- **BETATOFAVERAGE** f: The average β-value in front of the target. This value is necessary for an event-by-event Doppler correction with different incoming velocities.
- **BETADOPPLERAVERAGE** f: The average β-value used for the Doppler correction is defined here.
- **FIFIND** i: If i=1, the average first interaction point of a full energy peak γ-ray (with fold=1) is determined.
- **ADDBACK** i f: If i=1, add-back is employed. The second parameter specifies the maximum distance in cm between any two detectors for add-back reconstruction. The maximum addback distance of 15 cm is employed in our case.
- **TRIGGER** i: If i=1, it gives the trigger probability as function of γ-ray energy.

The input file for the DALI2 Reconstructor is shown in Listing B.4.

```
INPUTFILE .../78Zn/78Zn_Au_builder.root
OUTPUTFILE .../78Zn/78Zn_Au_Reconstructor_mult123.root
SPECTRABINANDRANGE 250 0. 6000.
DECAYPOSITIONZ 0.00
BETATOFAVERAGE 0.5482
BETADOPPLERAVERAGE 0.5305
STATISTICSREDUCTIONFACTOR 1
FIFIND 1
ADDBACK 1 15
TRIGGER 1
END
```

Listing B.4. Reconstructor.in ^{78}Zn

Bibliography

[1] Takaharu Otsuka et al. 'Evolution of shell structure in exotic nuclei'. In: *Rev. Mod. Phys.* 92 (1 Mar. 2020), p. 015002.

[2] E. Schrödinger. 'An Undulatory Theory of the Mechanics of Atoms and Molecules'. In: *Phys. Rev.* 28 (6 Dec. 1926), pp. 1049–1070.

[3] E. Rutherford. 'The scattering of alpha and beta particles by matter and the structure of the atom'. In: *Phil. Mag. Ser. 6* 21 (1911), pp. 669–688.

[4] N Bohr Dr. Phil. 'I. On the constitution of atoms and molecules'. In: *The London, Edinburgh, and Dublin Philosophical Magazine and Journal of Science* 26.151 (1913), pp. 1–25.

[5] Kris L G Heyde. 'The Nuclear Shell Model'. In: *The Nuclear Shell Model: Study Edition*. Berlin, Heidelberg: Springer Berlin Heidelberg, 1994, pp. 58–154.

[6] Roger D. Woods and David S. Saxon. 'Diffuse Surface Optical Model for Nucleon-Nuclei Scattering'. In: *Phys. Rev.* 95 (2 July 1954), pp. 577–578.

[7] Maria G Mayer. 'On Closed Shells in Nuclei'. In: *Physical review* 74.3 (1948), pp. 235–239.

[8] Otto Haxel, J Hans D Jensen and Hans E Suess. 'On the "Magic Numbers" in Nuclear Structure'. In: *Physical review* 75.11 (1949), p. 1766.

[9] David Halliday Krane Kenneth S. *Introductory nuclear physics*. Vol. 465. New York, NY: Wiley, 1988.

[10] Maria Goeppert Mayer. 'On Closed Shells in Nuclei. II'. In: *Phys. Rev.* 75 (12 June 1949), pp. 1969–1970.

[11] O Sorlin and M.-G. Porquet. 'Nuclear magic numbers: New features far from stability'. In: *Progress in Particle and Nuclear Physics* 61.2 (2008), pp. 602–673. ISSN: 0146-6410.

[12] C. Thibault et al. 'Direct measurement of the masses of ^{11}Li and $^{26-32}$Na with an on-line mass spectrometer'. In: *Phys. Rev. C* 12 (2 Aug. 1975), pp. 644–657.

[13] C. Détraz et al. 'Beta decay of $^{27-32}$Na and their descendants'. In: *Phys. Rev. C* 19 (1 Jan. 1979), pp. 164–176.

[14] J I Prisciandaro et al. 'New evidence for a subshell gap at N=32'. In: *Physics Letters B* 510.1 (2001), pp. 17–23. ISSN: 0370-2693.

[15] D. Steppenbeck et al. 'Evidence for a new nuclear 'magic number' from the level structure of ^{54}Ca'. In: *Nature* 502.7470 (2013), pp. 207–210. ISSN: 00280836.

[16] Takaharu Otsuka et al. 'Evolution of Nuclear Shells due to the Tensor Force'. In: *Phys. Rev. Lett.* 95 (23 Nov. 2005), p. 232502.

[17] E. Sahin et al. 'Shell Evolution towards ^{78}Ni: Low-Lying States in ^{77}Cu'. In: *Phys. Rev. Lett.* 118 (24 June 2017), p. 242502.

[18] J. Van de Walle et al. 'Coulomb Excitation of Neutron-Rich Zn Isotopes: First Observation of the 2_1^+ State in ^{80}Zn'. In: *Phys. Rev. Lett.* 99 (14 Oct. 2007), p. 142501.

[19] J. Van de Walle et al. 'Low-energy Coulomb excitation of neutron-rich zinc isotopes'. In: *Phys. Rev. C* 79 (1 Jan. 2009), p. 014309.

[20] A. Gottardo et al. 'Transition strengths in the neutron-rich ^{73,74,75}Ni isotopes'. In: *Phys. Rev. C* 102 (1 July 2020), p. 014323.

[21] C A Bertulani. 'Theory and Applications of Coulomb Excitation: CNS-EFES Summer School'. In: (2009).

[22] Kurt. Alder and Aage Winther. *Electromagnetic excitation : theory of Coulomb excitation with heavy ions*. North-Holland Pub. Co., 1975.

[23] Aage Winther and Kurt Alder. 'Relativistic coulomb excitation'. In: *Nuclear Physics A* 319.3 (1979), pp. 518–532. ISSN: 0375-9474.

[24] Carlos A Bertulani and Gerhard Baur. 'Electromagnetic processes in relativistic heavy ion collisions'. In: *Physics Reports* 163.5 (1988), pp. 299–408. ISSN: 0370-1573.

[25] T Glasmacher. 'Testing the Structure of Exotic Nuclei via Coulomb Excitation of Radioactive Ion Beams at Intermediate Energies'. In: *The Euroschool Lectures on Physics with Exotic Beams, Vol. III*. Ed. by J S Al-Khalili and E Roeckl. Berlin, Heidelberg: Springer Berlin Heidelberg, 2009, pp. 27–55.

[26] K. Alder et al. 'Study of Nuclear Structure by Electromagnetic Excitation with Accelerated Ions'. In: *Rev. Mod. Phys.* 28 (4 Oct. 1956), pp. 432–542.

[27] A N F Aleixo and C A Bertulani. 'Coulomb excitation in intermediate-energy collisions'. In: *Nuclear Physics A* 505.2 (1989), pp. 448–470. ISSN: 0375-9474.

[28] C. E. Aguiar, A. N. F. Aleixo and C. A. Bertulani. 'Elastic Coulomb scattering of heavy ions at intermediate energies'. In: *Phys. Rev. C* 42 (5 Nov. 1990), pp. 2180–2186.

[29] G Baur, K Hencken and D Trautmann. 'Electromagnetic dissociation as a tool for nuclear structure and astrophysics'. In: *Progress in Particle and Nuclear Physics* 51.2 (2003), pp. 487–564. ISSN: 0146-6410.

[30] David J Morrissey and Brad M Sherrill. 'In-Flight Separation of Projectile Fragments'. In: *The Euroschool Lectures on Physics with Exotic Beams, Vol. I*. Ed. by Jim Al-Khalili and Ernst Roeckl. Berlin, Heidelberg: Springer Berlin Heidelberg, 2004, pp. 113–135. ISBN: 978-3-540-44490-9.

[31] H Geissel et al. 'The GSI projectile fragment separator (FRS): a versatile magnetic system for relativistic heavy ions'. In: *Nuclear Instruments and Methods in Physics Research Section B: Beam Interactions with Materials and Atoms* 70.1 (1992), pp. 286–297. ISSN: 0168-583X.

[32] J. P. Dufour et al. 'Projectile fragments isotopic separation: Application to the lise spectrometer at GANIL'. In: *Nuclear Inst. and Methods in Physics Research, A* 248.2-3 (1986), pp. 267–281. ISSN: 01689002.

[33] M. SAM AUSTIN. *Up from Nothing: The Michigan State University Cyclotron Laboratory*. Michigan State University Press, 2015. ISBN: 9780996725200.

[34] Toshiyuki Kubo et al. 'BigRIPS separator and ZeroDegree spectrometer at RIKEN RI Beam Factory'. In: *Progress of Theoretical and Experimental Physics* 2012.1 (Dec. 2012). 03C003. ISSN: 2050-3911.

[35] N Fukuda et al. 'Identification and separation of radioactive isotope beams by the BigRIPS separator at the RIKEN RI Beam Factory'. In: *Nuclear Instruments and Methods in Physics Research Section B: Beam Interactions with Materials and Atoms* 317 (2013), pp. 323–332. ISSN: 0168-583X. DOI: https://doi.org/10.1016/j.nimb.2013.08.048. URL: http://www.sciencedirect.com/science/article/pii/S0168583X13009890.

[36] Toshiyuki Kubo. 'In-flight RI beam separator BigRIPS at RIKEN and elsewhere in Japan'. In: *Nuclear Instruments and Methods in Physics Research Section B: Beam Interactions with Materials and Atoms* 204 (2003), pp. 97–113. ISSN: 0168-583X.

[37] T. Kubo et al. 'Status and Overview of Superconducting Radioactive Isotope Beam Separator BigRIPS at RIKEN'. In: *IEEE Transactions on Applied Superconductivity* 17.2 (2007), pp. 1069–1077.

[38] O. Kamigaito et al. 'Present status and future plan of RIKEN RI beam factory'. In: *IPAC 2016 - Proceedings of the 7th International Particle Accelerator Conference* (2016), pp. 1281–1283.

[39] Kazunari Yamada et al. 'Construction of New Injector Linac for RI Beam Factory at RIKEN Nishina Center'. In: *Conf. Proc. C* 100523 (2010). Ed. by Akira Noda et al., MOPD046.

[40] *RIBF : Introduction to RI Beam Factory and Users' Information*. Accessed: 01.23.2021. URL: www.nishina.riken.jp/RIBF/accelerator/concept.html.

[41] Yasushige Yano. 'The RIKEN RI Beam Factory Project: A status report'. In: *Nuclear Instruments and Methods in Physics Research, Section B: Beam Interactions with Materials and Atoms* 261.1-2 SPEC. ISS. (2007), pp. 1009–1013. ISSN: 0168583X.

[42] S. Vaquero. 'In-beam gamma-ray spectroscopy of nuclei In-beam gamma-ray spectroscopy of nuclei'. In: *Ph.D. Thesis* (2018).

[43] K Kimura et al. 'High-rate particle identification of high-energy heavy ions using a tilted electrode gas ionization chamber'. In: *Nuclear Instruments and Methods in Physics Research Section A: Accelerators, Spectrometers, Detectors and Associated Equipment* 538.1 (2005), pp. 608–614. ISSN: 0168-9002.

[44] H Kumagai et al. 'Delay-line PPAC for high-energy light ions'. In: *Nuclear Instruments and Methods in Physics Research Section A: Accelerators, Spectrometers, Detectors and Associated Equipment* 470.3 (2001), pp. 562–570.

[45] S. Takeuchi et al. 'DALI2: A NaI(Tl) detector array for measurements of γ rays from fast nuclei'. In: *Nuclear Instruments and Methods in Physics Research A* 763 (Nov. 2014), pp. 596–603.

[46] Pieter Doornenbal. 'In-beam gamma-ray spectroscopy at the RIBF'. In: *Progress of Theoretical and Experimental Physics* 2012.1 (Dec. 2012). ISSN: 2050-3911.

[47] H Baba et al. 'New data acquisition system for the RIKEN Radioactive Isotope Beam Factory'. In: *Nuclear Instruments and Methods in Physics Research Section A: Accelerators, Spectrometers, Detectors and Associated Equipment* 616.1 (2010), pp. 65–68. ISSN: 0168-9002.

[48] Pieter Doornenbal. 'Manual of a GEANT4 Simulation Code for γ -Ray Detectors used in the RIKEN-RIBF Facility'. In: (2011).

[49] O B Tarasov and D Bazin. 'LISE++: Radioactive beam production with in-flight separators'. In: *Nuclear Instruments and Methods in Physics Research Section B: Beam Interactions with Materials and Atoms* 266.19 (2008), pp. 4657–4664. URL: http://lise.nscl.msu.edu/lise.html.

[50] C. Louchart et al. 'Collective nature of low-lying excitations in ^{70,72,74}Zn from lifetime measurements using the AGATA spectrometer demonstrator'. In: *Phys. Rev. C* 87 (5 May 2013), p. 054302.

[51] B Ekström et al. 'Decay Properties of 75-80Zn and Qβ-values of Neutron-Rich Zn and Ga Isotopes'. In: *Physica Scripta* 34.6A (Dec. 1986), pp. 614–623.

[52] S. V. Ilyushkin et al. 'β decay of the $\pi f_{5/2}$ ground state of ^{77}Cu studied with 225 MeV and 0.2 MeV purified radioactive beams'. In: *Phys. Rev. C* 80 (5 Nov. 2009).

[53] R. Orlandi et al. 'Single-neutron orbits near ^{78}Ni: Spectroscopy of the N=49 isotope ^{79}Zn'. In: *Physics Letters B* 740 (2014), pp. 298–302.

[54] *National Nuclear Data Center, NNDC*. URL: www.nndc.bnl.gov.

[55] J. Van Roosbroeck et al. 'Evolution of the nuclear structure approaching ^{78}Ni : β decay of $^{74-78}$Cu'. In: *Phys. Rev. C* 71 (5 May 2005), p. 054307.

[56] J M Daugas et al. 'The 8+ isomer in 78Zn and the doubly magic character of 78Ni'. In: *Physics Letters B* 476.3 (2000), pp. 213–218. ISSN: 0370-2693.

[57] A M Oros-Peusquens and P F Mantica. 'Particle-core coupling around 68Ni: a study of the subshell closure at N=40'. In: *Nuclear Physics A* 669.1 (2000), pp. 81–100. ISSN: 0375-9474.

[58] F. L. Bello Garrote et al. 'β decay of ^{75}Ni and the systematics of the low-lying level structure of neutron-rich odd-A Cu isotopes'. In: *Phys. Rev. C* 102 (3 Sept. 2020), p. 034314.

[59] E Sahin et al. 'Intermediate-energy Coulomb excitation of ^{77}Cu'. In: *RIKEN Accel. Prog. Rep.* RI49 (2016). URL: www.nishina.riken.jp/researcher/APR/APR049/pdf/36.pdf.

[60] N. Patronis et al. 'β-decay study of ^{77}Cu'. In: *Phys. Rev. C* 80 (3 Sept. 2009), p. 034307.

[61] S. Lalkovski. 'j-1 Anomaly through the Silver Isotopic Chain'. In: *Bulg. J. Phys.* 44.4 (2017), pp. 498–508.

[62] Ian J Thompson. 'Coupled reaction channels calculations in nuclear physics'. In: *Computer Physics Reports* 7.4 (1988), pp. 167–212. ISSN: 0167-7977.